University of Calgary

PRISM Repository **https://prism.ucalgary.ca**

The Vault Open Theses and Dissertations

2014-05-26

An Experimental Analysis of a Passive Pipeline Leak Detection Method

McKinnon, Sean

McKinnon, S. (2014). An Experimental Analysis of a Passive Pipeline Leak Detection Method (Master's thesis, University of Calgary, Calgary, Canada). Retrieved from https://prism.ucalgary.ca. doi:10.11575/PRISM/24882

http://hdl.handle.net/11023/1558

Downloaded from PRISM Repository, University of Calgary

UNIVERSITY OF CALGARY

An Experimental Analysis of a Passive Pipeline Leak Detection Method

by

Sean Paul McKinnon

A THESIS

SUBMITTED TO THE FACULTY OF GRADUATE STUDIES

IN PARTIAL FULFILMENT OF THE REQUIREMENTS FOR THE

DEGREE OF MASTER OF SCIENCE

DEPARTMENT OF MECHANICAL AND MANUFACTURING ENGINEERING

CALGARY, ALBERTA

MAY 2014

© SEAN PAUL MCKINNON 2014

Abstract

Recent advances in MEMS have facilitated measurement of very weak signals transmitted through soil from low frequency excitation of pipelines. The newest experimental MEMS seismometers with noise floors as low as 10 ng/$\sqrt{\text{Hz}}$ and frequency bandwidths from 0.1 to 100 Hz, promise a new method to compensate for the deficiencies in today's leak detection methods.

The in-situ setup is a passive leak detection method according to which a two-layer network of seismometers is used to monitor the pipeline. The first and second layers of sensors act respectively as inputs and outputs to the system. The propagation medium (soil) between the sensors, through which pipeline energy dissipates, is defined in this research as the "signal channel". An experimental setup comprised of mechanical hardware, instrumentation and software for signal acquisition and analysis, is used to investigate the feasibility of the approach. Minute changes of the transfer function, due to product contamination, are revealed in the dynamic mechanical properties of the signal channel.

Preface

The scope of this research encompasses the experimental setup and numerical analysis of a method of pipeline leak detection. This research explores the sensor placement (distance between sensors) with respect to the radial dimension of the pipeline. What this research does not explore is sensor placement with respect to the longitudinal axis of the buried pipeline.

Acknowledgements

Thank you Dr. Spiewak for the many hours, evenings and weekends you dedicated to helping me shape this thesis. Your patient input was invaluable. Over many coffees and in-depth conversations this research was refined to a place I am very proud of. Your support and guidance is appreciated.

Table of Contents

List of Tables

List of Figures and Illustrations

List of Symbols, Abbreviations and Nomenclature

Chapter 2	
Symbol	Definition
$C_1(\omega)\ and\ C_2(\omega)$	$Frequency\ dependant\ calibration\ factors\ of\ accelerometers$
C_{ls}	$Capacitance\ on\ left\ side$
C_{rs}	$Capacitance\ on\ right\ side$
D	$Electrical\ Polarization$
d	$Piezoelectric\ Coefficient\ Matrix$
∇^2	$Laplacian\ operator$
ε_0	$Permitivity\ of\ the\ vacuum$
E	$Youngs\ Modulus$
ECC	$Electromechanical\ coupling\ coefficient$
E_f	$Electric\ Field$
e	$Void\ ratio$
ε_p	$Electrical\ Permittivity\ Matrix$
F_z	$Amplitude\ of\ the\ Input\ Sinusoid$
$g(r,\omega)$	$Geometric\ spreading\ function$
$Y(x,t)$	$vector\ potential\ (ie.displacement)$
I	$Second\ moment\ of\ area$
L	$Effective\ length\ of\ suspension\ beam$
$M(r,\omega)$	$The\ ratio\ of\ output\ acceleration\ to\ input\ acceleration$
μ	$rigidity$
$\psi(r,\omega)$	$Complex\ valued\ phase\ angle$
ρ	$density$
S	$Compliance\ Matrix$
s_v	$Strain\ Vector$
T	$Applied\ Mechanical\ Stress$
$T_d(r,\omega)$	$Deterministic\ transfer\ function$
$T_e(r,\omega)$	$Experimental\ transfer\ function$

V_s	$Volume\ of\ Solids$
v_s	$S-wave\ velocity$
V_v	$Volume\ of\ voids$
z_1	$Amplitude\ of\ first\ measurement$
z_2	$Amplitude\ of\ second\ measurement$
ζ	$Damping\ ratio$

Chapter 3	
Symbol	Definition
∇^2	$Laplacian\ operator$
f	$frequency$
$G(s)$	$LT\ of\ the\ impulse\ response = Transfer\ function$
$g(t)$	$Impulse\ Response\ of\ the\ system$
K	$bulk\ modulus$
λ	$wavelength\ (maximum\ sensor\ distance\ from\ pipe)$
μ	$rigidity$
ω_n	$Natural\ Frequency\ identified\ in\ the\ Bode\ Plot$
P_0	$Propagation\ medium\ position$
$\emptyset(x,t)$	$scalar\ potential\ /\ field\ (ie. pressure, position)$
ρ	$density$
t	$time$
$U(s)$	$LT\ of\ the\ input\ signal$
v_p	$P-wave\ velocity$
$Y(s)$	$LT\ of\ the\ output\ signal$
$y(t)$	$Input\ signal\ (unit\ impulse\ function)$
$*$	$Convolution\ operator$

Chapter 4	
Symbol	Definition
A	$Total\ area\ inside\ the\ pipe\ between\ supports$
D_o	$Effective\ Diameter\ of\ the\ Obstruction$
d	$Distance\ between\ proof\ mass\ and\ diffraction\ grating$
E	$Modulus\ of\ elasticity$
E_v	$Expected\ value\ operator$
f	$frequency\ in\ Hertz$
f_0	$Pipe\ span\ natural\ frequency\ [Hz]$
f_p	$Pulsation\ Frequency$
f_v	$Vortex\ Shedding\ frequency$
g	$Gravitational\ constant$
I	$Moment\ of\ inertia$
I_{in}	$Incident\ laser\ intensity$
$I_{\pm 1}$	$First\ diffraction\ order\ intensity$
I_0	$Zeroth\ diffraction\ order\ intensity$
k	$Spring\ Constant$
$J_j(\omega)$	$Joint\ acceptance\ of\ the\ jth\ mode$
l	$Pipe\ span$
λ_f	$Frequency\ factor$
λ_o	$Optical\ Wavelength$
m	$Mass$
m_m	$Modal\ mass\ per\ unit\ length$
μ	$Weight\ per\ unit\ length\ of\ beam$
N	$Total\ number\ of\ sample\ points$
n	$Number\ of\ Impeller\ Vanes\ or\ Lobes$
N_r	$Rotational\ speed$
n_m	$1,2,3\ \ldots\ (number\ of\ modes)$

ω_j	$Natural\ frequency\ of\ the\ jth\ mode$
ω_n	$Natural\ Frequency$
ω_r	$Resonance\ Frequency$
$\omega[m]$	$an\ odd\ length\ (2L+1)-point\ lag\ window$
P	$Number\ of\ pump\ pistons$
$P_{xx}(f)$	$Power\ spectral\ density$
$P_{yy}(f)$	$Power\ Spectral\ Density\ of\ the\ Geophone\ (output)$
ψ_j	$Spanwise\ mode\ shape$
$r(x_1, x_2, \omega)$	$Correlation\ factor\ for\ homogeneous\ turbulence$
$r_{xx}[m]$	$Autocorrelation\ sequence\ (input)$
$r_{xy}[m]$	$Crosscorrelation\ sequence\ (input)$
S	$Strouhal\ Number$
$S_{F_{ij}}(\omega)$	$Power\ spectrum\ of\ the\ generalized\ force$
$S_{L_{ij}}(\omega)$	$Power\ spectrum\ of\ the\ pipeline$
T	$Total\ sampling\ interval$
T_{cg}	$Gain\ of\ the\ transfer\ function\ obtained\ from\ correlogram\ based\ PSD's$
T_{cp}	$Phase\ of\ the\ transfer\ function\ obtained\ from\ correlogram\ based\ PSD's$
T_i	$Sampling\ interval$
T_{pg}	$Gain\ of\ the\ transfer\ function\ obtained\ from\ periodogram\ based\ PSD's$
$U(z)$	$z\ transform\ of\ the\ input\ signal$
V	$Flow\ Velocity$
$X[s]$	$Discrete\ Fourier\ Transform$
$x[n]$	$Inverse\ Discrete\ Fourier\ Transform$
ζ	$Damping\ ratio$
Y_{ij}^2	$The\ mean\ square\ response\ of\ the\ jth\ mode$
$Y(z)$	$z\ transform\ of\ the\ output\ signal$
z	$Forward\ time\ shift\ operator$
$*$	$Complex\ conjugate$

CHAPTER 1: INTRODUCTION

Risk can be defined as the severity of an outcome multiplied by the probability of occurrence. Pipeline leaks have a relatively low probability of occurrence compared to other accidents that take place in the oil and gas industry, however the severity of the outcome is dangerously high. Therefore the risk associated with pipeline leaks is one that cannot be overlooked.

1.1 Impacts of Pipeline Leaks

Pipeline leaks are detrimental to both the environment and the economy. One interesting fact is that one liter of spilled oil can contaminate a million liters of groundwater [1]. The number of pipeline releases per year in Alberta from 1990 to 2012 are shown in Figure 1-1. The upper most parts of Figure 1-1 represent hydrocarbon liquid, which is easily the most detrimental leak in terms of damage to the environment. Hydrocarbon gas release is also an issue in terms of

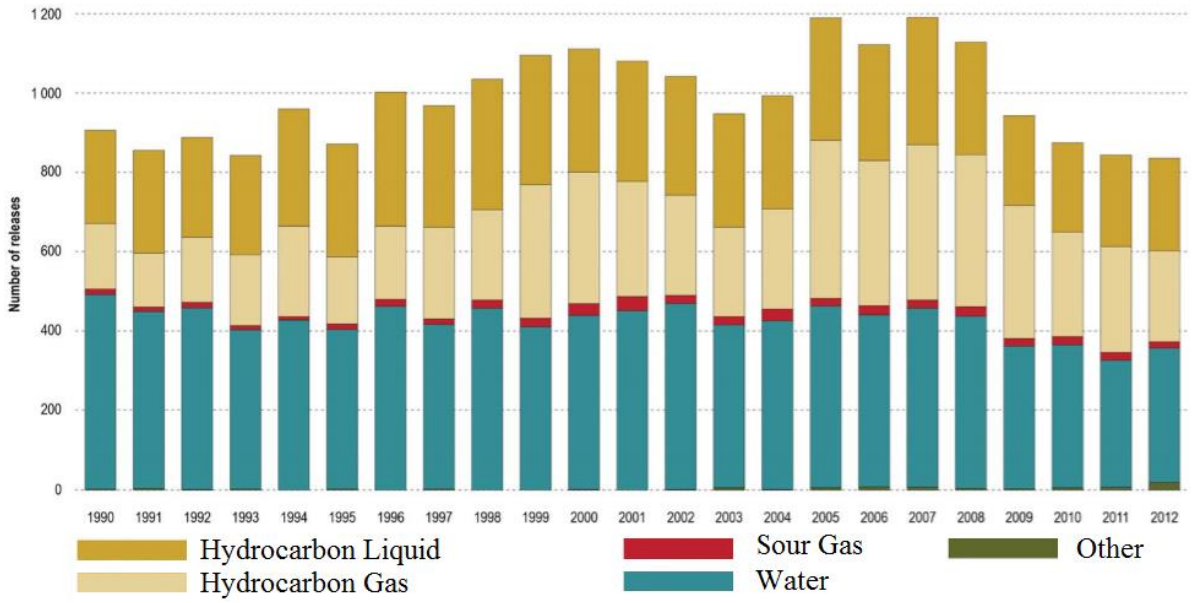

Figure 1-1: Number of Pipeline Releases per Year by Substance [37]

damage to the environment. This type of release does not get as much media attention as a hydrocarbon liquid release, however it has a significant impact on global warming [2].

Figure 1-2 shows pipeline failures by cause in Alberta from 1990 to 2012. Engineers can work to

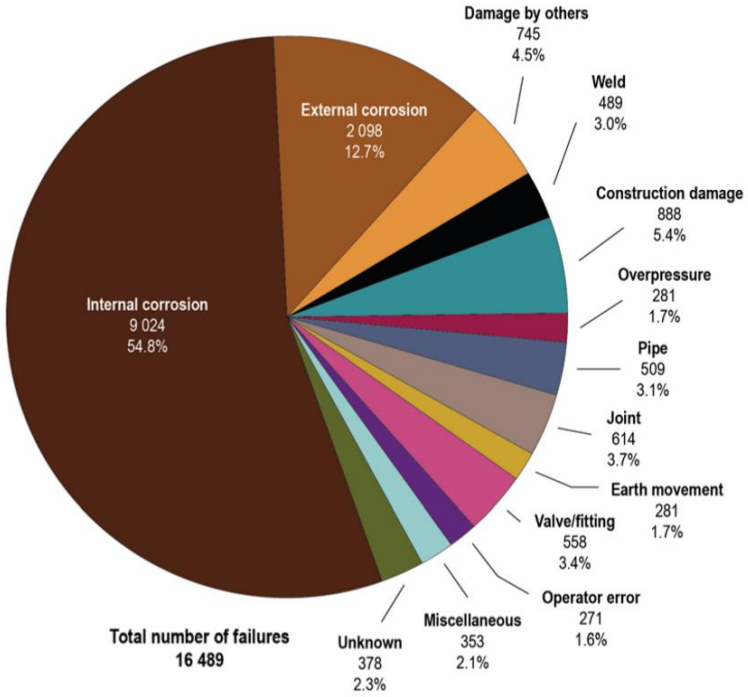

Figure 1-2: Pipeline Failures by Cause for All Years Combined [37]

overcome many of the causes, for example, improving pipeline coatings, and using cathodic protection to reduce the number of leaks due to external corrosion. However, many of the failures are unpredictable, for example, leaks due to earth movement or for unknown reasons. Due to the unpredictable variables that are beyond human control, there will always be a need for leak detection methods that can accurately determine the location of a leak in the shortest time possible. The effects of pipeline leaks are also felt by the economy. The Enbridge Kalamazoo spill dumped 3.8 million liters of diluted tar sands bitumen into the Kalamazoo River. In addition to large fines, cleanup costs for that leak are already $1 billion, and the river is still contaminated.

1.2 Current Leak Detection Methods

Table 1-1 gives an overview of the leak detection methods available today, with their advantages and disadvantages.

Table 1-1: Summary of current leak detection methods [3]

Method	Description	Advantages	Disadvantages
Walking the Line	Physically walking, driving or flying over the pipeline to detect leaks via vegetation changes, seeing a leak, or smelling additives	Low cost	Time consuming Additives must be removed
Arial Thermogram	Infrared thermographic pipeline image that identifies a "plume" around a leak	Accurately identifies and locates leaks	Affected by sunlight, rain and wind conditions
Line Flow Balance	Calculating the volumetric flow rate at two points along the pipeline	Easily identifies a gross loss of product	Cannot pinpoint source of leak Line flow rates must not vary with time
Acoustic Detector	Leaks may produce a low frequency emission that propagates down the pipeline	Crews can identify the location of a leak	Complications occur when there are multiple leaks or a splice in the pipe
"Pig" Based Monitoring Systems	A device called a pig is inserted into the pipeline which travels due to compressed flow, the pig is recovered at a receiving station	Can identify the location of a leak to within a pipe length Utilizes a wide array of technology including acoustics	Pigs can become stuck due to debris build up inside the pipe
Real-Time Transient Model	RTTM makes it possible to calculate mass flow, pressure, density, and temperature at every point pipeline	Can obtain data from a wide range of instruments Can identify the location of a leak	High initial capital investment

Many leak detection schemes are available today, however, none of which are suitable for all situations. Because of this, there will always be a need for new leak detection methods.

1.3 The Proposed Leak Detection Method

Figure 1-3 shows the proposed setup. The in-situ setup is a passive detection method, meaning the energy used to detect a leak is inherently present in the system due to pipeline vibration. A two-layer network of sensors (e.g. seismometers) is used to monitor dynamic properties of the medium surrounding the pipeline (signal channel). The propagation medium between the sensors, through which pipeline energy dissipates is defined in this research as the "signal channel". As a pipeline radiates energy through the surrounding medium; the first sensor (Seismometer A) measures the input to the real world signal channel. The second sensor

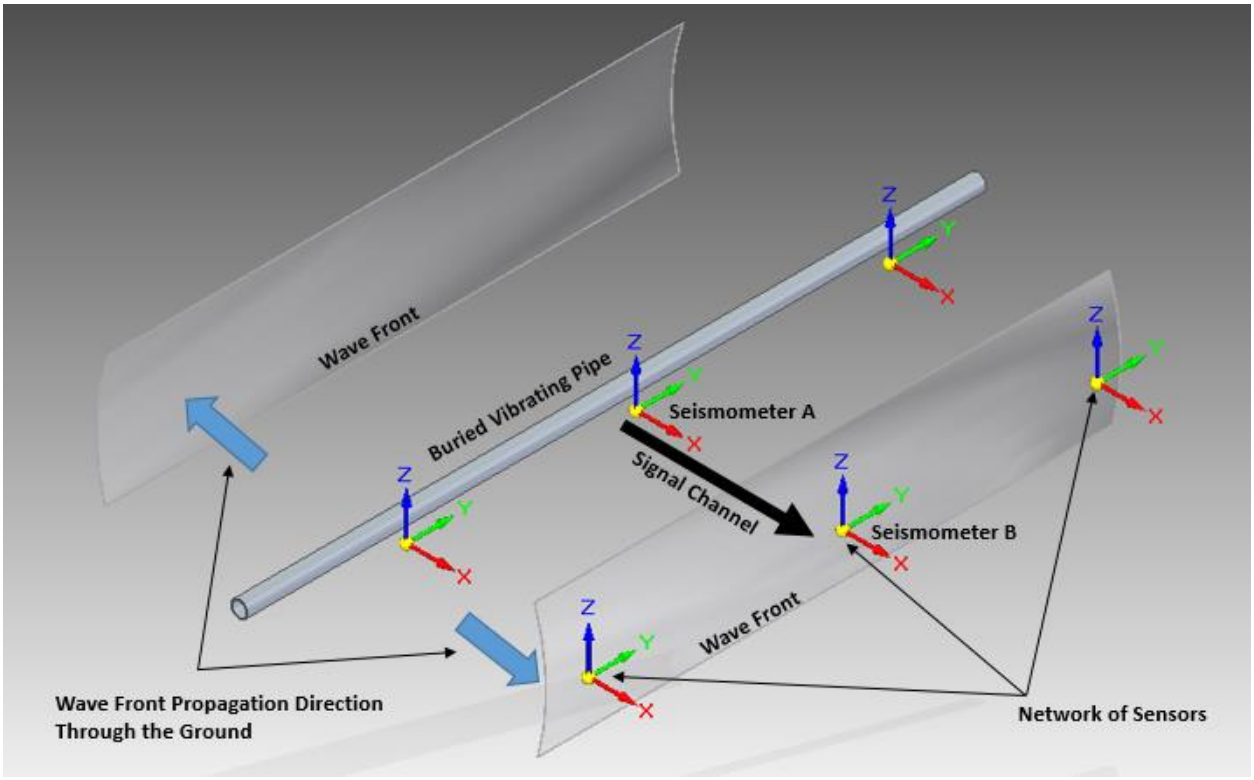

Figure 1-3: In-Situ Proposed Leak Detection Method

(Seismometer B) measures the output from the real world signal channel. Both sensors provide input to the model of the signal channel. Figure 1-4 shows the block diagram of this system, it is expected that the appropriate model will produce quantities indicating the presence of pipeline product from pipeline vibration as input.

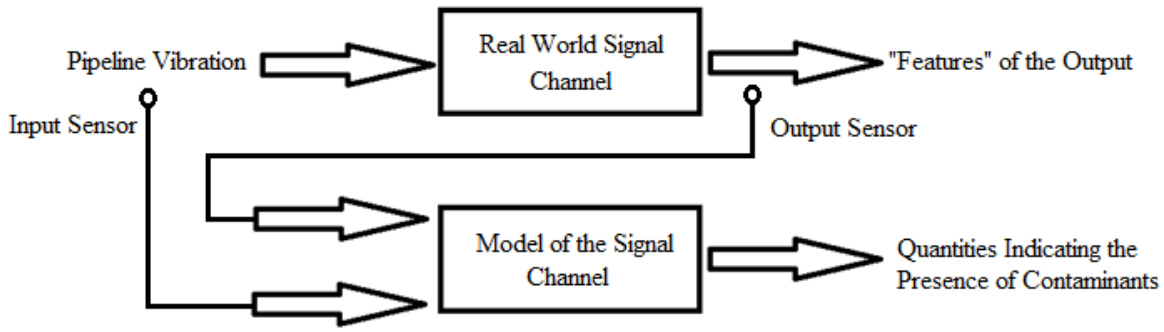

Figure 1-4: Leak Detection Block Diagram

By using advanced signal and system analysis techniques, changes in the medium properties can be determined, and used to detect pipeline leaks. The research presented in this thesis describes an experimental setup and numerical evaluation techniques which identify features of the signal channel for pipeline leak detection. A rigorous experimental setup is an essential research and development step towards developing the leak detection method, and a requirement to validate the hypothesis that changes in features of the signal channel are indicative of hydrocarbon contamination. The features of interest considered in this research are the gain and phase of the transfer function, the delay of the system, the natural frequencies and damping ratios of the signal channel.

CHAPTER 2: LITERATURE REVIEW

2.1 Traditional MEMS Sensing Methods

2.1.1 Electrostatic Sensing

MEMS devices are potentially suitable for pipeline leak detection. They have traditionally used a few types of sensing schemes, the most abundantly used types are electrostatic and capacitive. These two types of sensing will be reviewed in detail here, and more advanced optical methods will be reviewed in Chapter 4.

A capacitor can be defined as two conductors that are capable of holding opposite charges [4]. If the distance between the two conductors change, the capacitance value will change; this is the fundamental aspect which allows electrostatic sensing to be a reality. There are two configurations of electrostatic sensing devices that are most common; parallel plate capacitors, and interdigitated fingers. In the 1990's the field of MEMS encountered rapid growth, one of the most prominent devices to be produced in this time was the ADXL accelerometer manufactured by Analog Devices, shown in Figure 2-1. This accelerometer was specifically designed to be

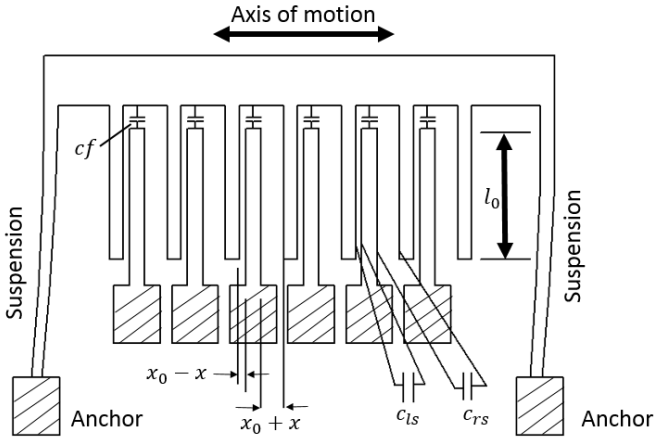

Figure 2-1: ADXL Transverse Comb Drive Accelerometer [4]

used in the automotive industry as an actuator for air bag deployment, and stands as a hallmark for all electrostatic sensing MEMS devices. The ADXL accelerometer used an interdigitated finger setup. There are two capacitance values associated with a single finger, one to the left hand side of the finger and one to the right, at rest they are [4]:

$$C_{ls} = C_{rs} = \frac{\varepsilon_0 l_0 t}{x_0} \quad \textbf{(2-1)}$$

where:

C_{ls} $Capacitance\ on\ left\ side$ [F]

C_{rs} $Capacitance\ on\ right\ side$ [F]

ε_0 $Permitivity\ of\ the\ vacuum = 8.85 * 10^{-14}\ [\frac{F}{cm}]$

As an acceleration is applied to the chip, the proof mass (with mass *m*) will move due to inertial force *(F = ma)*. This changes the gap on either side of the fingers and the capacitance values become:

$$C_{ls} = \frac{\varepsilon_0 l_0 t}{x_0 - x} \quad \textbf{(2-2)}$$

$$C_{rs} = \frac{\varepsilon_0 l_0 t}{x_0 + x} \quad \textbf{(2-3)}$$

This very small capacitance change is read using on-chip signal processing devices. If the fringe field capacitance is ignored (often the case), the total capacitance is:

$$C_{tot} = C_{ls} + C_{rs} \quad \textbf{(2-4)}$$

During motion, the rate of capacitance change can be measured with respect to displacement, termed the displacement sensitivity:

$$S_x = \frac{\partial C_{tot}}{\partial x} \quad \textbf{(2-5)}$$

During motion, the rate of capacitance change can be measured with respect to acceleration, termed the acceleration sensitivity. The force constant of the proof mass is twice that of a single fixed-guided cantilever:

$$k = 2 * \frac{12EI}{L^3} \quad \textbf{(2-6)}$$

where:

L $Effective\ length\ of\ suspension\ beam$ [m]

E $Youngs\ Modulus$ [GPa]

I $Second\ moment\ of\ area$ [m^4]

Because there are 6 fingers contributing to the capacitance, the overall capacitance is:

$$C(x) = 6\frac{\varepsilon_0 l_0 t}{x_0 - x} + 6\frac{\varepsilon_0 l_0 t}{x_0 + x} \quad \textbf{(2-7)}$$

By making a substitution for *x* using:

$$F = ma = xk; \quad x = \frac{ma}{k}; \quad x = \frac{maL^3}{24\ EI} \quad \textbf{(2-8)}$$

The expression for acceleration sensitivity is:

$$\frac{\partial C(x)}{\partial a} = \frac{\partial}{\partial a}\left[6\varepsilon_0 l_0 t\left(\frac{1}{x_0 - \frac{maL^3}{24\ EI}} + \frac{1}{x_0 + \frac{maL^3}{24\ EI}}\right)\right] \quad \textbf{(2-9)}$$

There are several advantages and disadvantages to using electrostatic sensing, and are summarized in Table 4-2.

2.1.2 Piezoelectric Sensing

The direct effect of piezoelectricity is observed when a piezoelectric crystal is placed under stress (tensile or compressive) [4]. The stress creates an electric field via altering the spacing between the centers of positive and negative charge sites in each domain cell. Compressive and tensile stresses will create electric fields and subsequently voltages of opposite polarity. The inverse piezoelectric effect is observed when an electric field exerts a force between positive and negative charge sites, which causes elastic strain in the crystal. The change in dimension of the crystal depends on the polarity of the applied electric field. The equation which relates the electrical polarization and applied mechanical stress is [4]:

$$D = dT + \varepsilon E_f \qquad \textbf{(2-10)}$$

where:

$D \quad Electrical\ Polarization\ [\frac{C}{m^2}]$

$T \quad Applied\ Mechanical\ Stress[\frac{N}{m^2}]$

$E_f \quad Electric\ Field\ [\frac{V}{m}]$

$\varepsilon_p \quad Electrical\ Permittivity\ Matrix[\frac{F}{m}]$

$d \quad Piezoelectric\ Coefficient\ Matrix\ [\frac{C}{N}]$

When the device is used as a sensor, there is often no electric field present, and the second term is ignored. The inverse piezoelectric effect can be described by a similar matrix-form equation, and is included here for reference purposes as it relates to piezoelectric actuation. Several piezoelectric actuators are discussed later in this thesis in the Experimental Setup section.

$$s_v = ST + dE \quad \textbf{(2-11)}$$

where:

s_v $Strain\ Vector$

S $Compliance\ Matrix\ [\frac{m^2}{N}]$

When the device is used as an actuator, there is often no mechanical stress present, and the first term is ignored. The electromechanical coupling coefficient (ECC) is a measure of how much energy is transferred between the two energy domains during the process of actuation or sensing [4]. The loss of energy is transferred to the environment as heat.

$$ECC = \frac{Energy\ Converted}{Input\ Energy} \quad \textbf{(2-12)}$$

The advantages and disadvantages of using piezoelectric sensing techniques can be found in Table 4-2.

2.2 Resonant-Column Tests of Soils

By setting cylindrical samples of soils and sands into torsional and longitudinal oscillations, wave propagation within the samples can be studied. The device used to set the samples into vibration is shown in Figure 2-2. The resonance frequency and length of the sample are all that is needed to find the wave velocity. The resonant column test has become the accepted industry standard for testing dynamic properties of soils since the 1960's [5]. It is reported that for ideal spheres, the samples will respond to the loading in a nonlinear, inelastic manner, and that the confining pressure placed on the sample will have a dominant effect. Obtaining an accurate estimate of the shear modulus of the soil is of most importance in such tests. In this research, the

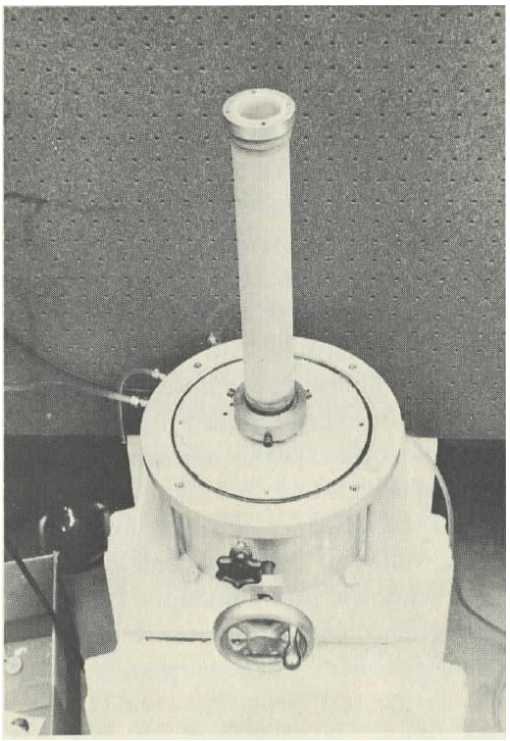

Figure 2-2: Resonant Column Test Apparatus [5]

major variable of concern is the damping ratio, as shear waves are not measured in both the in-situ and experimental setups. Tests conducted on Ottawa Illinois sand by Hall and Richart (1967) [5], revealed that both the longitudinal and shear wave velocities decreased as the amplitude of vibration increased. These tests also indicated that the wave velocities decreased as much as 10 to 15 percent as the void ratio was changed from the minimum value to the maximum. Where the void ratio is defined as the ratio of the volume of voids to the volume of solids (Figure 2-3):

$$e = \frac{V_v}{V_s} \qquad \textbf{(2-13)}$$

Where:

e $Void\ ratio$

V_v $Volume\ of\ voids$

V_s $Volume\ of\ Solids$

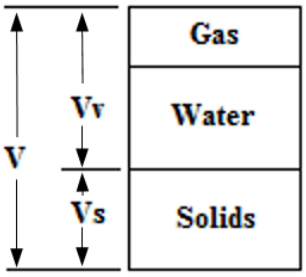

Figure 2-3: Phase Diagram to Illustrate Calculation of Void Ratio

When the sample is set into free vibration, it will eventually come to a stop. A reduction of the amplitude of vibration is due to the internal damping of the sample; the reduction is similar to that of a viscously damped system. The theory for a single-degree-of-freedom viscously damped system may act as a suitable model for damping which occurs in soils [5]. The decay of a free vibration of a single-degree-of-freedom system is described by the logarithmic decrement, which is defined as the ratio of two successive amplitudes of motion [5].

$$\delta = ln\frac{z_1}{z_2} = \frac{2\pi\zeta}{\sqrt{1-\zeta^2}} \quad \textbf{(2-14)}$$

$$\zeta = \frac{\delta}{\sqrt{4\pi^2+\delta^2}} \quad \textbf{(2-15)}$$

where:

z_1 $Amplitude\ of\ first\ measurement$

z_2 $Amplitude\ of\ second\ measurement$

ζ $Damping\ ratio$

The logarithmic decrement can be obtained from experimental data (decay curve) by plotting each amplitude against the cycle number in a semi-log graph as shown in Figure 2-4.

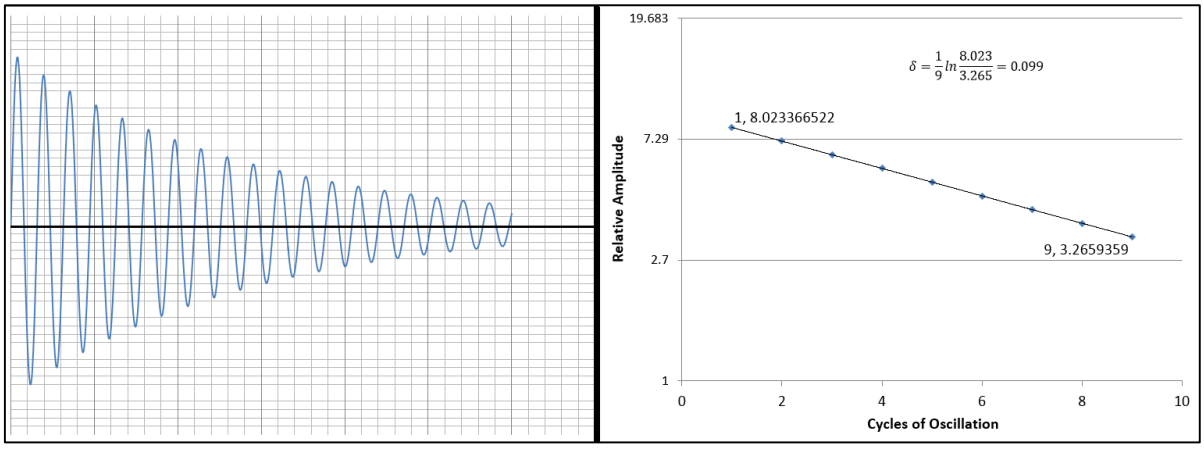

Figure 2-4: Amplitude-Time Decay Plot (left), Amplitude vs. Cycle Number Plot (right)

The theory of a viscously damped free vibrating system applies to the system if a straight line results. This theory may also be applied to the impulse response of a system, as the two methods of exciting the system into free vibration are essentially identical. To measure the log decrement from two non-successive peaks the following formula can be used [6].

$$\delta = \frac{1}{n} ln \frac{z_1}{z_n} \quad \textbf{(2-16)}$$

The damping found between peaks 1 and 2 of the impulse response will be the same as the damping found between peaks 2 and 3 if the system is linear. If the results are appreciably different then the system is non-linear.

2.3 Transfer Functions of Soils

In a linear system the transfer function is defined as the output signal divided by the input signal in the frequency domain [7]. For many systems found in the literature, vertical input and output soil vibration signals are obtained; the deterministic input and output signals are respectively [8]:

$$Y_z = F_z e^{i\omega t} \quad \textbf{(2-17)}$$

$$U_z(r, \omega, t) = F_z g(r, \omega) e^{i(\omega t - \psi(r,\omega))} \quad \textbf{(2-18)}$$

where:

F_z $Amplitude\ of\ the\ Input\ Sinusoid$

r $Distance\ from\ source\ to\ reciever$

ω $Angular\ frequency$

$g(r,\omega)$ $Geometric\ spreading\ function$

$\psi(r,\omega)$ $Complex\ valued\ phase\ angle$

The deterministic transfer function is [9]:

$$T_d(r,\omega) = \frac{U_z(r,\omega,t)}{Y_z} = g(r,\omega)e^{-i\psi(r,\omega)} \quad \textbf{(2-19)}$$

The experimental transfer function is:

$$T_e(r,\omega) = \frac{-M(r,\omega)C_2(\omega)}{\omega^2 C_1(\omega)} \quad \textbf{(2-20)}$$

where:

$M(r,\omega)$ $The\ ratio\ of\ output\ acceleration\ to\ input\ acceleration$

$C_1(\omega)\ and\ C_2(\omega)$ $Frequency\ dependant\ calibration\ factors\ of\ accelerometers$

The following research was conducted on acceleration data gathered from earthquakes in the Wellington Metropolitan Area, New Zealand [10]. The following three dimensional ground motion transfer functions shown in Figure 2-7 convey the coupling between a soil site and a nearby rock site. The 3x3 complex matrix (transfer function) represents the amplitude and phase relations between the soil site and rock site. Each earthquake is considered to be an independent instance of polarized motion at both sites. Figure 2-5 shows the sensor setup, where the hypocenter is the center of the earthquake.

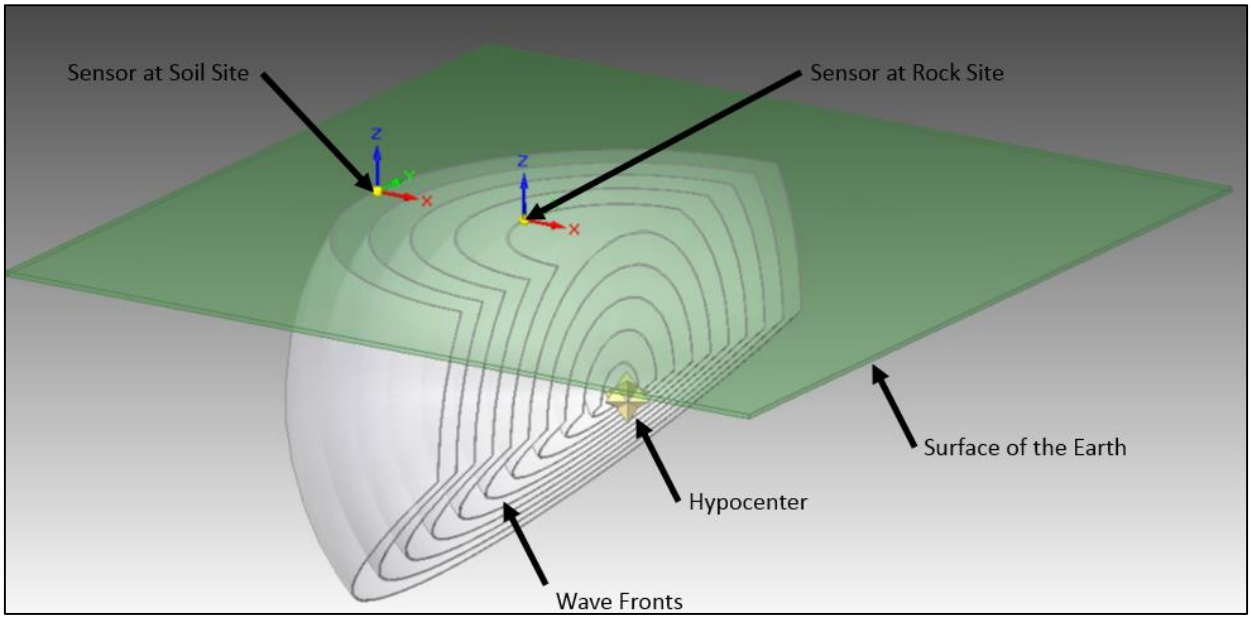

Figure 2-5: Sensor Positions Relative to the Earthquake Hypocenter [10]

Figure 2-6 is a topographical map showing the strong motion sites in the Wellington area, where the two sites of interest in this review are shown circled. The epicentre (point on the earth's surface directly above the hypocenter) distribution area surrounds the area shown in Figure 2-6.

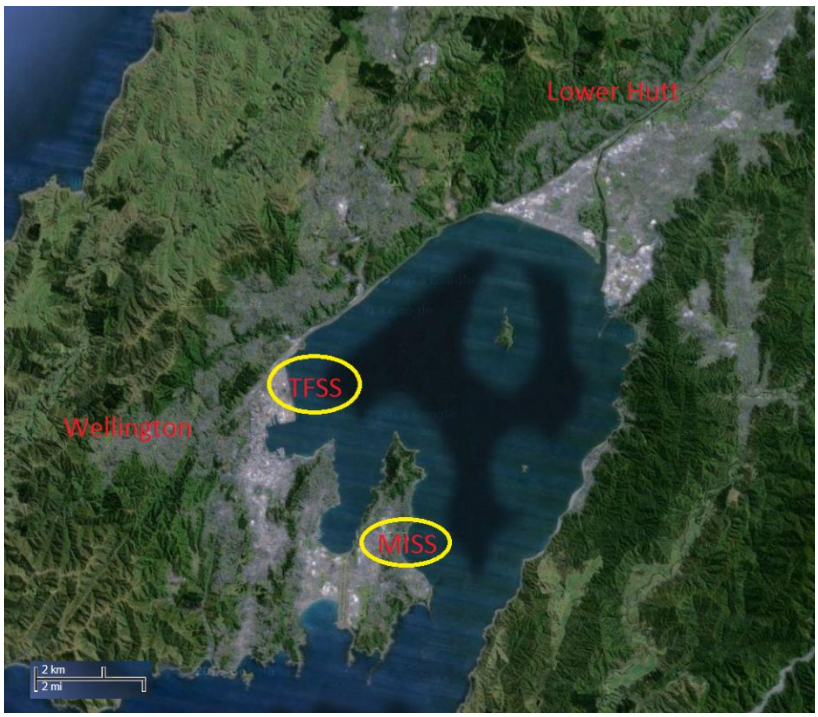

Figure 2-6: Strong Motion Sites in the Wellington Area [10]

The soil descriptions for each of the sites considered here are shown in Table 2-1, the differences are considerable. The numbers shown in Table 2-1 represent the soil thickness in meters.

Table 2-1: Description of Soils underneath the Strong-Motion Network Sites [10]

Soil Type and Thickness (m)							Depth to Bedrock
Station	A	B	C	D	E		F
TFSS	5	145					150
MISS	12	9	40				61
A, Gravelly sand with shells			C, Gravel			E, Basal gravel	
B, Blue silty clay			D, Wilford marine			F, Greywacke bedrock	

The method used in the literature defines $s(f)$ as the frequency domain ground-motion vectors at a soil site, and $r(f)$ a nearby rock site, at frequency f. The motion at the rock site is considered the input and the soil site the output. The transfer function is $G(i,j)$, $(i,j = 1\ (north),\ 2\ (east), 3\ (vertical))$ between the wave motion in the direction *j* at the rock site and the wave motion in the direction *i* at the soil site. The most general linear relationship among the three components of the two vectors is shown in Figure 2-7. Because the seismograms recorded at each station are generally different lengths, the time series data was modified by either adding zeros or truncating them to the same duration. The data was also band-pass filtered between 0.1 and 20 Hz. The transfer functions for the two sites are much different due to the differences in soil characteristics.

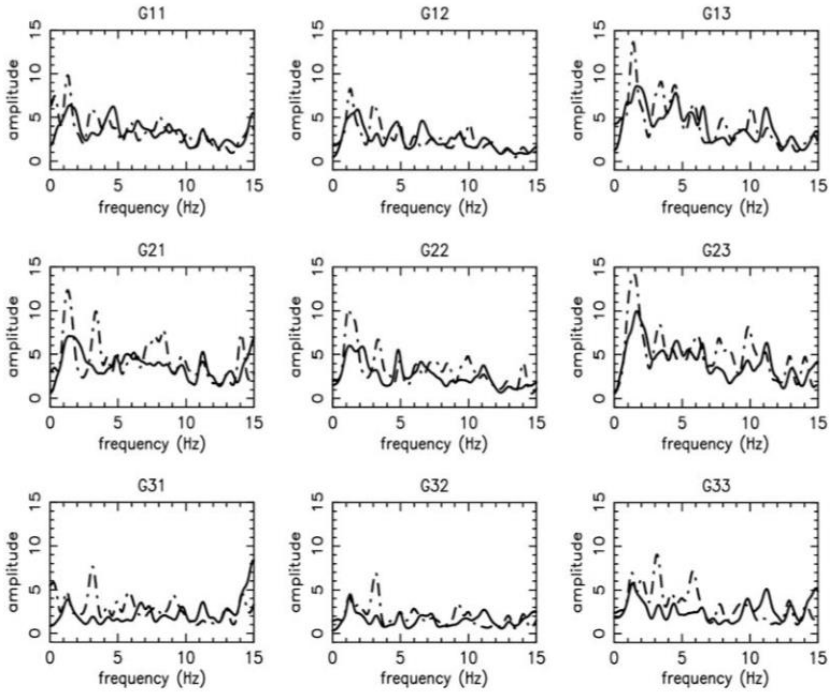

Figure 2-7: Comparison of the Transfer Functions for TFSS (Solid Line) and MISS (Dashed-Dotted Line) [10]

2.4 Pipeline Leak Detection Using Frequency Content Analysis

A similar method of leak detection to that proposed in this research is the acoustic detection method. The acoustic detection method utilizes geophones, hydrophones and accelerometers that are attached directly to the pipe or their appurtenances (e.g. control valves) [11]. The similarity between this method and the proposed method is the use of the Fast Fourier Transform (FFT). Consequently, the inherent difficulties in executing the methods are similar, namely; the inherent noise in the system, and signal attenuation in the medium. In one research study that examined the usefulness of the acoustic detection method, the type of estimate used for the power spectral density was the periodogram [11]. This report stated that the most efficient method of computing the power spectral density was to use a Hanning window, and power spectrum averaging (periodogram) with 50% overlap. The same method of computing the periodogram is

investigated in this research, with the addition of zero padding. The research on the acoustic detection method identified the impact in the choice of sensor in regards to measuring ambient noise. It was found that the accelerometer used in the experiment had a lower sensitivity, and the ambient noise power was very close to the "leak signal" power; essentially burying the "leak signal". The geophone had a much higher sensitivity and the "leak signal" power was well above the ambient noise. Because of this, the data collected from the geophone was used to compute the transfer function between two points on the test pipe. The conclusion drawn was that the periodogram method performed best when the signal power was well above the ambient noise.

2.5 Ground Waves

2.5.1 Introduction to Ground Waves

The way a sensor is placed in the ground will have a dominant effect on what type of ground wave it measures. Therefore the dynamic properties of the ground obtained from the data will depend on the sensor orientation. There are four types of ground waves; two of which are classified as body waves, and two are surface waves.

2.5.2 Body Waves

The primary wave is named such because it is the first wave to reach a seismic station in an earthquake. It is also called a P-wave or a pressure wave. The primary wave is classified as a body wave, and travels the fastest through the earth, it is comprised of compression and dilation of the ground [12]. The area ahead of the wave is momentarily compressed, as the area behind the wave is dilated, as can be seen on the left in Figure 2-8. If a sensor is buried in the ground with the sensing axis parallel with the surface of the earth it will measure the P-wave. A

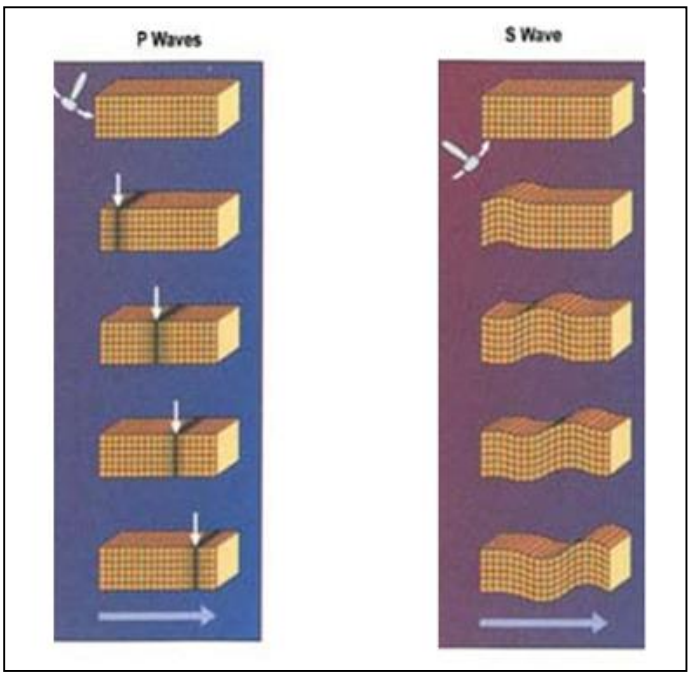

Figure 2-8: Body Waves [40]

fundamental mathematical description of the P-wave is given in Section 3.2. The secondary wave is named such, because it is the second wave to reach the seismic station in an earthquake. It is also called an S-wave or shear wave. Secondary waves are also classified as body waves, and are made of alternating transverse motion (right side of Figure 2-8). If a sensor is buried in the ground with the sensing axis vertical it will be measuring the secondary wave. Digitally sampling / analyzing P-waves and S-waves will respectively result with normal and sheer dynamic soil / ground properties. The partial differential equation describing the shear wave motion is the same for both types of surface waves presented next.

2.5.3 Surface Waves

Love waves are classified as a surface wave, and are also called L-waves or long waves. Love waves are comprised of alternating transverse motion parallel to the earth's surface (top of Figure 2-9). A Love wave is a horizontally polarized sheer wave [12]. It is strongest at the

surface and decreases in amplitude as depth increases. Love waves are dispersive, meaning the wave velocity is dependent on frequency, with the low frequency waves generally propagating the fastest. The depth of penetration of the Love wave increases as the frequency decreases. If a sensor is placed horizontally on the surface of the earth, the Love wave will be measured.

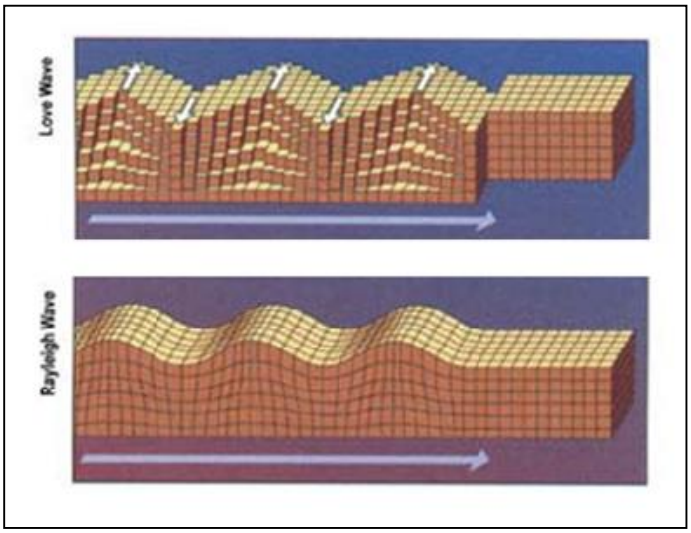

Figure 2-9: Surface Waves [40]

Rayleigh waves are the second type of surface wave, and are commonly referred to as "ground-roll". The motion of this wave is in the direction of propagation and vertical / perpendicular with respect to the surface of the earth (shown on the bottom of Figure 2-9). A sensor placed on the surface of the earth with the sensing axis placed vertically will measure the Rayleigh wave. Rayleigh waves are also dispersive and the amplitude decreases with depth. The appearance of the Rayleigh wave is similar to water waves. Digitally sampling / analyzing Love waves and Rayleigh waves will result with shear dynamic soil / ground properties. The partial differential equation describing the displacement of shear, Love and Rayleigh waves is the vector wave equation, which is valid for homogenous, isotropic materials (2-21) [12].

$$\nabla^2 \Upsilon(x,t) = \frac{1}{{v_s}^2} \frac{\partial^2 \Upsilon(x,t)}{\partial t^2} \qquad \textbf{(2-21)}$$

where:

$\Upsilon(x,t)$ $vector\ potential\ (ie. displacement)$

v_s $S-wave\ velocity$

∇^2 $Laplacian\ operator = \frac{\partial^2}{\partial x^2}+\frac{\partial^2}{\partial y^2}+\frac{\partial^2}{\partial z^2}$

The S-wave velocity is given below.

$$v_s = \sqrt{\frac{\mu}{\rho}} \tag{2-22}$$

where:

μ $rigidity$

ρ $density$

The rigidity of the material has a simple interpretation. If the value of the rigidity is large then the material experiences a small strain for a given stress. Shear waves cannot propagate through fluids, as a fluid has a rigidity value of zero, and cannot support any shear stress.

CHAPTER 3: PASSIVE LEAK DETECTION METHOD

3.1 Motivation and Hypothesis

The hypothesis underlying this research is that changes in the propagation medium surrounding a pipeline may be detected due to contamination from pipeline product. This is facilitated by monitoring low frequency pipeline vibrations, with high sensitivity seismometers. The motivation behind investigating the feasibility of this new leak detection method are the recent advances in MEMS seismometers. As it will be shown, the increased sensitivity, and wide bandwidths of emerging MEMS devices promise a new method to monitor pipelines. The focus of this research is the manner in which this hypothesis will be tested; an experimental setup and numerical evaluation techniques for detecting medium contamination.

3.2 Contamination Detection and Quantification

The propagation medium between the sensors, through which pipeline energy dissipates is defined in this research as the "signal channel", as shown Figure 3-1.

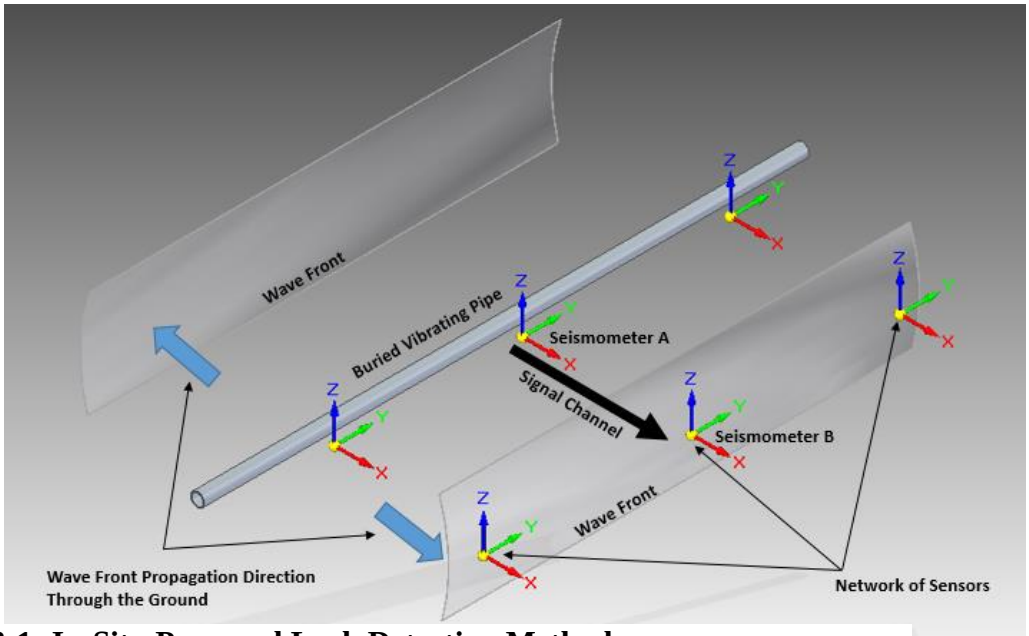

Figure 3-1: In-Situ Proposed Leak Detection Method

Moving product through pipelines involves a large quantity of energy, this energy is gradually dissipated along the pipeline. One form of energy dissipation is mechanical vibration into the medium surrounding the pipeline, which creates ground waves. The first step in identifying signal channel contamination is to model the way the ground waves move through the signal channel. It is expected that the ideal model will produce quantities indicating the presence of pipeline product from pipeline vibration as input (Figure 3-2).

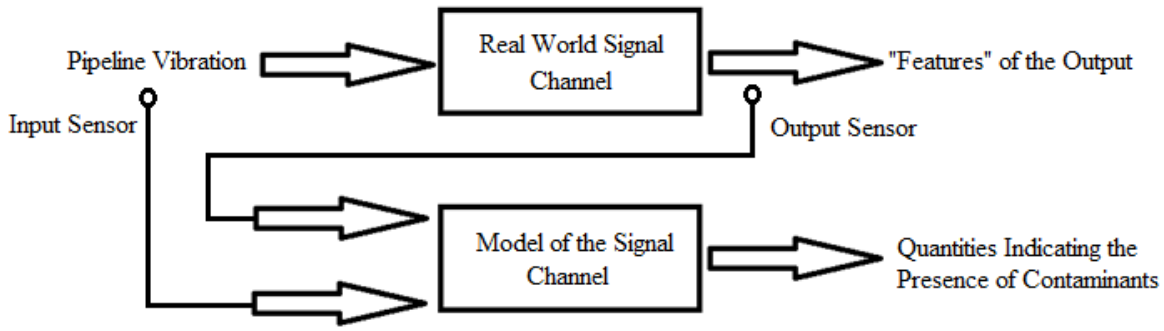

Figure 3-2: Leak Detection Block Diagram

The dynamic properties of the medium are of interest, the function of the model is to identify the changes in these properties. It is assumed that the signal channel can be characterized by analysing the signals from sensors A and B, and that its characteristics will change due to pipeline leaks.

3.2.1 Distributed-Parameter Properties of Soil

Energy from the pipeline dissipates through several types of ground waves. The way a sensor is placed in the ground will determine which type of ground wave is being measured. The P-wave most accurately represents the strongest wave in the in-situ leak detection scheme and in the experimental leak detection setup considered in this research. Therefore the present discussion will focus on the primary wave, shown in Figure 3-3. Firstly, this is because sensor A is buried

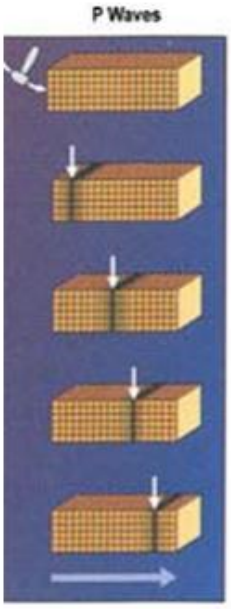

Figure 3-3: P-wave [40]

close to the pipe, and cannot measure surface waves. Second, it is possible to orient the sensors such that the shear wave is measured, however the energy present in the shear wave is much less than that of the P-wave, and is not considered in the experimental setup for this reason.

The partial differential equation which describes the P-wave propagation is the scalar wave equation in three dimensions, valid for a homogeneous, isotropic material [12], [13].

$$\nabla^2 \emptyset(x,t) = \frac{1}{{v_p}^2} \frac{\partial^2 \emptyset(x,t)}{\partial t^2} \quad \textbf{(3-1)}$$

where:

$\emptyset(x,t)$ $scalar\ potential\ /\ field\ (ie. pressure, position)$

t $time$

∇^2 $Laplacian\ operator = \frac{\partial^2}{\partial x^2} + \frac{\partial^2}{\partial y^2} + \frac{\partial^2}{\partial z^2}$

v_p $P - wave\ velocity$

$$v_p = \sqrt{\frac{K + \frac{4\mu}{3}}{\rho}} \quad \textbf{(3-2)}$$

where:

μ $rigidity$

ρ $density$

K $bulk\ modulus$

The impact hydrocarbon contamination has on the wave equation is found in the expression for the P-wave velocity (3-2). The density, rigidity and bulk modulus are affected by the addition of hydrocarbons to the signal channel. The bulk modulus is "the ratio of pressure applied to the fractional volume change that results" [12]. Both the S-wave and P-wave velocities depend on the rigidity, however, because the shear wave does not create a volume change in the material, it does not depend on the bulk modulus.

Given the constitutive empirical equation of the P-wave propagation (3-1), it is possible to compute a "response" of the propagation medium at any chosen location $P_0 = \{x_0, y_0, z_0\}$. The response will be found as a solution to Equation 3-1 for the specific initial and boundary values defined by the pipeline vibration and physical geometry of the propagation medium. However, the reading from the sensor placed within the field represented by the underlying wave equation will not only depend upon Equation 3-1. Other factors will include the properties of the medium, the excitation, and the geometry of the propagation medium. In the case of the laboratory experiments, the size and shape of the soil containment, as well as the reflection coefficients from the container will have an impact on the measured signal. Because the sensors are stationary, an assumption is made that the system is a lumped parameter system. It is therefore not the intention of this research to model the distributed parameter system. The intention is to model the system using the transfer function, however, before this can be done it must be proved that the signal channel is a linear system. This is accomplished through the use of the impulse response; if the impulse response shows linearity then the transfer function can be used to model the signal channel.

3.2.2 Impulse Response of Soil

A hypothetical case that the signal channel is a linear system is considered. Therefore the output signal can be expressed in terms of the pipeline vibration *u(t)*. The convolution integral of an arbitrary input signal with the impulse response of the signal channel is [14]:

$$y(t) = g(t) * u(t) = \int_0^t g(t-\tau)u(\tau)d\tau \qquad \textbf{(3-3)}$$

where:

$y(t)$ $Output\ signal$

$u(t)$ $Arbitrary\ input\ signal\ (pipeline\ vibration)$

$g(t)$ $Impulse\ Response\ of\ the\ system\ (signal\ channel)$

$*$ $Convolution\ operator$

The impulse response of the system is its output in response to the unit impulse function as input. The impulse function simulates a rapid release of energy from the pipeline. The impulse response can be obtained from solving the P-wave PDE for the specific geometry of the propagation medium, however, it can also be obtained experimentally. Several impulse responses obtained from the enhanced experimental setup are shown in Figure 3-4, the details of the setup used to obtain them are presented in Section 5.2.2. Figure 3-4 (A) identifies the time delay of the system, as it can be seen there is a clear delay for the impulse to reach the geophone (1.1 ms). Two features of the signal channel provided via the impulse response are the damping ratio of the system and the time delay. Obtaining the damping ratio from the impulse response is discussed in Section 2.2. The time delay feature can be used to calculate the velocity of the wave [15], a feature of the signal channel that will change due to hydrocarbon contamination. The

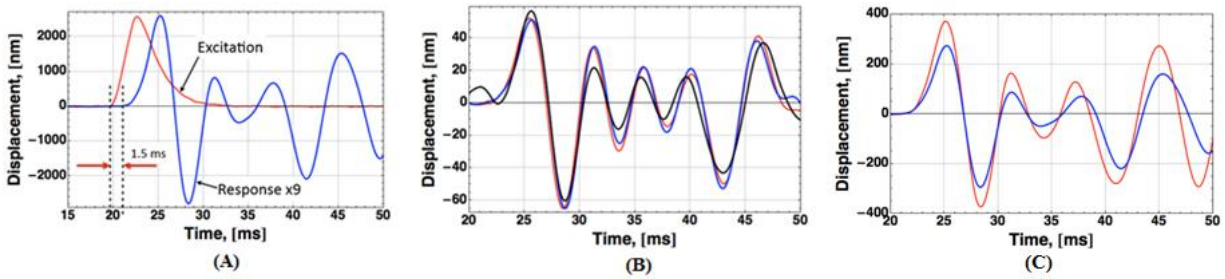

Figure 3-4: Impulse Response of Enhanced Experimental Setup

(A) Representative Impulse Response Showing Time Delay

(B) A Comparison of Normalized Responses Obtained at Different Small Amplitudes Red – 0.4 µm, Blue – 0.16 µm (multiplied by 2.5), Black – 0.08 µm (multiplied by 5)

(C) A Comparison of Normalized Responses Obtained at Different Large Amplitudes Dark Blue – 2.6µm, Light Red – 0.4µm (multiplied by 6.5)

velocity will almost always increase with effective pressure. This pressure dependence is the result of closing cracks, grain boundaries and filling voids within the soil, which stiffens the elastic frame. "Because velocity depends on the ratio of elastic modulus to density, the modulus and density effects "fight" each other; sometimes the velocity goes up; sometimes down" [15]. The three impulse responses in Figure 3-4 (B) are normalized to assist in comparison. The gain shown for the three impulse responses obtained with three different low excitation amplitudes of 0.4 µm, 0.16 µm and 0.08 µm are very similar. The three different impulse responses are shown using different colors for each amplitude of excitation. The average percent difference between the three maximum amplitudes is only 9.2%. This similarity proves that superposition applies and validates the linearity of the system for small excitation amplitudes. It was found that linearity applied up to 1.5 µm of displacement from the actuator. Beyond 1.5 µm amplitude of excitation the system exhibits nonlinearity, as shown in Figure 3-4 (C). A decrease in the gain for the high excitation of 2.6µm is clearly shown, with a percent difference between maximum amplitudes of 36.4%.

The major shortfall of using only the impulse response of the system to detect signal channel contamination is that rarely a pipeline would produce such an impulse. The impulse response is therefore limited to the laboratory, and does not offer as much information as the transfer function.

3.2.3 Transfer Function Model of Soil

Applying the properties of the Laplace Transformation (LT) to Equation 3-3 facilitates obtaining the transfer function of the signal channel. Specifically, according to the convolution theorem the convolution of two functions is equivalent in the Laplace domain to multiplying their Laplace Transforms (LT) [14]. The ratio of the output LT over the input LT is the transfer function.

$$L\{y(t) = g(t) * u(t)\} \rightarrow Y(s) = G(s)\,U(s) \qquad \textbf{(3-4)}$$

where:

$Y(s)$ $LT\ of\ the\ output\ signal$

$G(s)$ $LT\ of\ the\ impulse\ response = Transfer\ function\ of\ the\ system$

$U(s)$ $LT\ of\ the\ input\ signal$

A model inherently has two components: its structure and coefficients / parameters. For linear dynamic and time invariant systems the most commonly used model of dynamics is the transfer function. The transfer function is advantageous because “the frequency response of a system examines the characteristics of the outputs for the entire range of possible sinusoidal inputs” [16]. A common representation of the transfer function uses a scalar polynomial representation in the numerator and the denominator and is known as the “Transfer Function form”, shown in Equation 3-5 [16]. The poles and zeros are another feature of the signal channel which can be

monitored to identify signal channel contamination. Of the several transfer function forms to be presented, the rational polynomial form is of the least value when used to determine changes in properties of the signal channel because the poles and zeros are not obvious.

$$G(s) = \frac{b_m s^m + b_{m-1} s^{m-1} + \cdots + b_0}{a_n s^n + a_{n-1} s^{n-1} + \cdots + a_0} \quad \textbf{(3-5)}$$

An alternative, more useful representation is known as the pole-zero form, shown in Equation 3-6 [16]. The Pole-Zero form has an advantage that all of the roots in both the numerator and denominator are shown explicitly. The pole-zero form may be suitable to detect changes in the signal channel due to pipeline leaks.

$$G(s) = \frac{K \prod_{i=1}^{m} (s + z_i)}{\prod_{i=1}^{n} (s + p_i)} = \frac{K(s + z_1)(s + z_2) \ldots (s + z_m)}{(s + p_1)(s + p_2) \ldots (s + p_n)} \quad \textbf{(3-6)}$$

The order of the transfer function is the order of the polynomial in the denominator, which determines how accurately it represents the "real world" scenario. For causal systems the order of the numerator is less than that of the denominator [16]. Determining the order of the transfer function is an obstacle that must be overcome in order to capture the dynamics of the modeled system; a challenge that this research will explore. The two previous transfer functions are shown in the continuous time domain. By moving to the discrete time domain and plotting the poles and zeros on the complex plane, a useful pictorial view of the transfer function is obtained, and can be used to detect changes in the properties of the signal channel, as shown in Figure 3-5. This figure is from a test using the enhanced experimental setup. The test and setup are described respectively in Sections 5.3.6 and 5.2.2. One

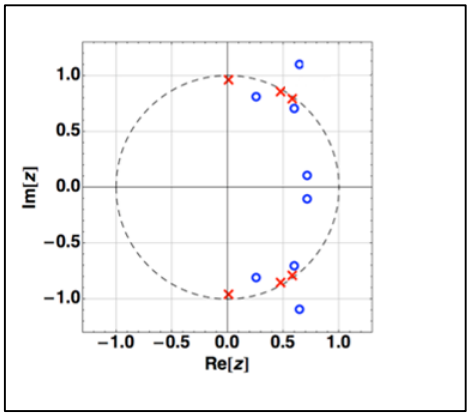

Figure 3-5: Pole-zero Plot

method of determining signal channel contamination includes monitoring the pole-zero plot of the transfer function to detect changes in their positions. When the pipeline is first installed and no leaks are present, a picture of the "normal" pole-zero plot is obtained. By monitoring the "normal" picture, it is possible to detect changes in the signal channel. External variables may change the pole-zero plot, such as water content or temperature changes, as well as rain. It may be possible to use the pole-zero technique in conjunction with other means to remove the possibility of erroneous alarms. Combinations of leak detection techniques are standard in industry, e.g. including satellite imagery or radar to confirm rainfall.

The most useful form of the transfer function for use in this research is the partial fraction expanded form. Presented in this form it is possible to simulate properties of the signal channel by a set of mechanical oscillators (mass - spring - dashpot) connected in parallel. Specifically, a high order transfer function can then be decomposed into a sum of several second order transfer functions and several first order transfer functions, as shown in Equation 3-7 [16]. The natural frequencies as well as the damping ratios can be readily obtained, and can be compared for clean and contaminated soil.

$$G(s) = \frac{b_1 s + c_1}{s + a_1} + \frac{b_2 s + c_2}{s + a_2} + \frac{d_1 s + e_1}{s^2 + 2\zeta_1 \omega_{n1} s + \omega_{n1}^2} + \frac{d_2 s + e_2}{s^2 + 2\zeta_2 \omega_{n2} s + \omega_{n2}^2} \qquad \textbf{(3-7)}$$

The Bode plot is a useful method for visualizing the second order transfer functions obtained from the partial fraction expansion method. The Bode magnitude plot shows the magnitude of the frequency response gain versus the frequency. The Bode phase plot shows the frequency response phase shift versus the frequency. The addition of hydrocarbons to the signal channel will change the stiffness, damping and mass of the system. The following examples illustrate the

effects on a system modelled by a second order transfer function. Figure 3-6 shows the effect that changing stiffness has on such a system. The resonance frequency is increased as the system stiffness is increased.

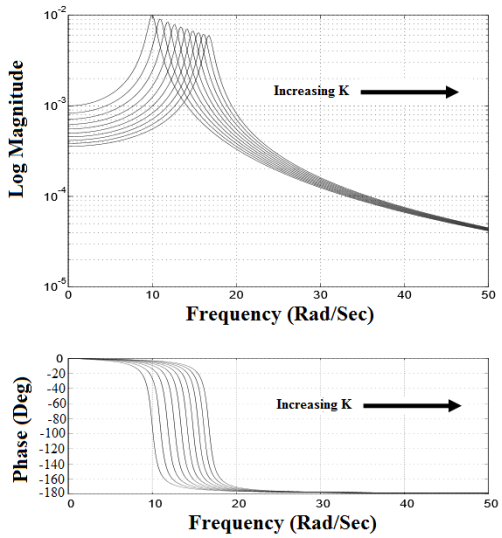

Figure 3-6: Effect of Changing Stiffness SDOF System [38]

Figure 3-7 shows how the system response changes with the addition of mass. The resonance frequency decreases as the mass is increased. The sharpness of the resonance peak (damping) decreases as the mass increases.

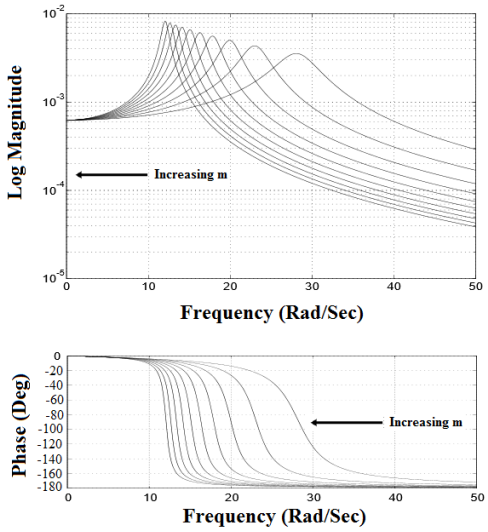

Figure 3-7: Effect of Changing Mass SDOF System [38]

Figure 3-8 shows the effect that changing the damping has on the system response. The resonance frequency shows little change. What does change is the magnitude of the resonance peak.

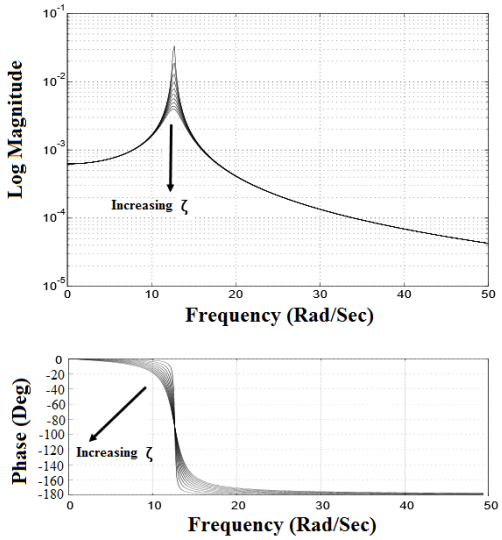

Figure 3-8: Effect of Changing Damping SDOF System [38]

One method of evaluating this change experimentally is to use the so called "full width at half maximum (FWHM)" [6]. In this approach the numerical value of the damping ratio is determined from the resonance peak in the Bode magnitude plot, as shown in Figure 3-9.

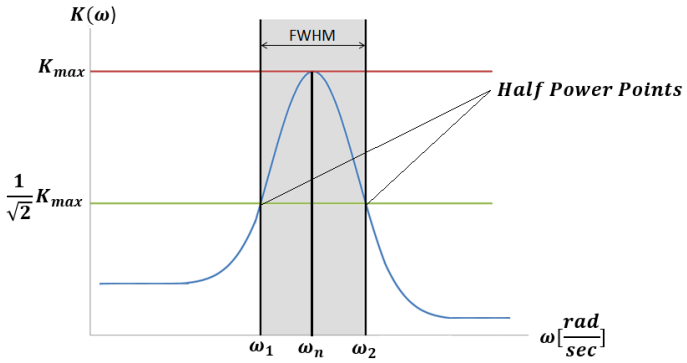

Figure 3-9: Full Width at Half Maximum Applied to a Sample Bode Plot

The half power value corresponds to $\frac{1}{\sqrt{2}}K_{max}$, and the FWHM is $\omega_2 - \omega_1$. The damping ratio is calculated as follows from the FWHM method [6].

$$\zeta = \frac{\omega_2 - \omega_1}{2\omega_n} \quad \textbf{(3-8)}$$

where:

ω_n $Natural\ Frequency\ identified\ in\ the\ Bode\ Plot$

This method of evaluation is coarse, a more sophisticated method of data evaluation is explored in this research via the parametric method of estimating the transfer function.

3.3 Experimental Identification

Following the principle of triple modular reliability, an investigation into three methods of estimating the transfer function are presented in this research. The transfer function of the signal channel can be estimated using the power spectral densities (PSD's) of the inputs and outputs of the system. Two of the three methods employ this estimation process. These methods are referred to in the literature as the periodogram and correlogram. The third method of estimating the transfer function is known as parametric estimation. In statistics it is often referred to as auto regressive moving average (ARMA).

Of the three methods, the periodogram is the most intuitive and the fastest, but it can provide only the gain-frequency relationship of the system. This method makes no assumptions about the dynamics of the system, and only considers the signals which are captured by the seismometers. For this reason the approach is termed "signal based" analysis. In addition, the periodogram does not make any attempt to fit a model to the transfer function using coefficients or parameters, it makes no assumption that the structure of the model is fixed. For this reason the approach is

categorized as “non-parametric” estimation. Table 3-1 summarizes the categories to which the three experimental identification methods belong.

Table 3-1: Summary of Experimental Identification Methods

	Signal Based	System Based
Non-parametric Estimate	Periodogram	Correlogram
Parametric Estimate		Parametric Identification

The correlogram provides a higher quality estimate for the gain and phase information than the periodogram, and is explored for this reason. The major difference between the periodogram and correlogram is that the correlogram first estimates the autocorrelation sequence before applying the FFT, and the periodogram acts directly on the data set to estimate the PSD. As it will be shown in Chapter 4, the correlogram assumes an explicit relationship between the input and output signals and is consequently categorized as “system based” identification. The correlogram is also a non-parametric estimate of the transfer function, as it does not attempt to fit a model to using coefficients (parameters) to the transfer function.

The most advanced method of estimating the transfer function presented is parametric estimation. Unlike the periodogram and the correlogram it does not use the FFT in any way, rather it acts only on the time domain signals. The structure of the model used to fit the transfer function is assumed to be known, and coefficients (parameters) are used to fit the data. For this

reason the name “parametric identification” is used. This method is also a system based identification method. As it will be shown in Chapter 4, it is a more robust, accurate and elegant method than the former two methods.

3.4 Features of Interest

The features of the signal channel which can be monitored for product contamination are found from the transfer function. The features of the signal channel that this research investigates are presented in Table 3-2.

Table 3-2: Investigated Features of the Signal Channel Obtained via the Transfer Function

	Feature of the Signal Channel
1)	Gain of the system
2)	Phase shift of the system
3)	Delay of the system
4)	Damping ratio of the soil (sand)
5)	Natural frequencies (local peaks of the magnitude plot)

Because the periodogram and correlogram are nonparametric methods the numerical values obtained for the above features are not as conclusive or as accurate as those obtained from parametric estimation. A representative Bode plot is shown below in Figure 3-10, obtained using the parametric estimate of the transfer function. The full details of the numerical analysis used to obtain the plots are presented in Section 4.2.1.4, and the details of the experimental setup are presented in Chapter 5, along with representative experimental results. In the Bode magnitude plot several features are distinguished. The low frequency gain and phase shift are shown from 20 to 80 Hz, a rapid phase shift drop is shown at approximately 90 Hz. A resonance frequency is

shown at 89.5 Hz, and using the FWHM method the damping ratio was calculated to be 0.033. Using the partial fraction expansion method using second order transfer functions, the resonance frequency was found to be 89.54 Hz, and the damping ratio is 0.0329.

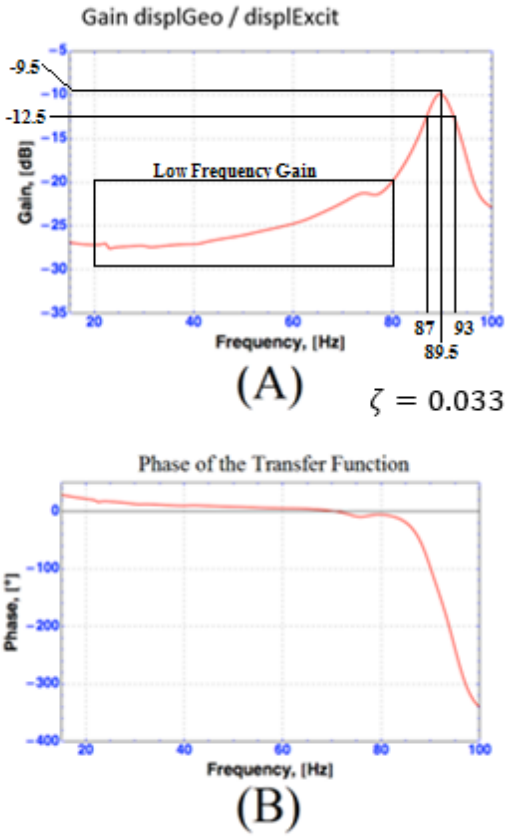

Figure 3-10: Bode Plot obtained from the Parametric Estimate of the Transfer Function from the Enhanced Experimental Setup, Excitation Amplitude = 1.5 µm

(A) Gain Shown From 0 – 100 Hz

(B) Phase Shown From 0 – 100 Hz

3.5 Impact of Signal Attenuation

Two inherent difficulties in the proposed leak detection method are the inherent noise in the pipeline vicinity, and signal attenuation in the medium. A distance from the pipe that a sensor may be placed will be strongly influenced by the signal attenuation in the signal channel. Because the geometric attenuation of bulk waves is proportional to one over the square of the

distance, the bulk wave is attenuated in one to two wavelengths from the source. After one to two wavelengths the Rayleigh wave becomes dominant [9]. For example, if the pipeline was producing a strong excitation at 80Hz, and an average velocity for bulk ground waves is 5.5 km/s [12], the maximum distance from the pipe a sensor can be placed is calculated as follows (two wavelengths).

$$2\lambda = \frac{v_p}{f} = \frac{5500\ [\frac{m}{s}]}{80\ [Hz]} = 137.50\ m \qquad \textbf{(3-9)}$$

where:

$\lambda \quad wavelength\ (maximum\ sensor\ distance\ from\ pipe)$

$f \quad frequency$

Assuming the attenuation limit is two wavelengths, the seismometer at the end of the signal channel can be place up to 137.5m from the pipeline (for a strong excitation at 80 Hz).

3.6 Impact of Ambient Noise

The above considerations implied that all involved signals were deterministic. However in reality either random or stochastic signals are encountered. Deterministic methods will fail when stochastic and random signals are encountered, and therefore other methods of signal channel modelling must be considered. The ambient noise is either stochastic or random in nature. In the city, ambient noise may also be known as noise pollution, however it is still present in the most remote places on earth. Examples of ambient noise could be wind blowing or a river rushing. Ambient noise has been studied in great detail. Two industry accepted models which provide the ambient noise level for extreme situations are known as the NLNM (New Low Noise Model) and NHNM (New High Noise Model) [17]. These models are power spectral density (PSD) plots that

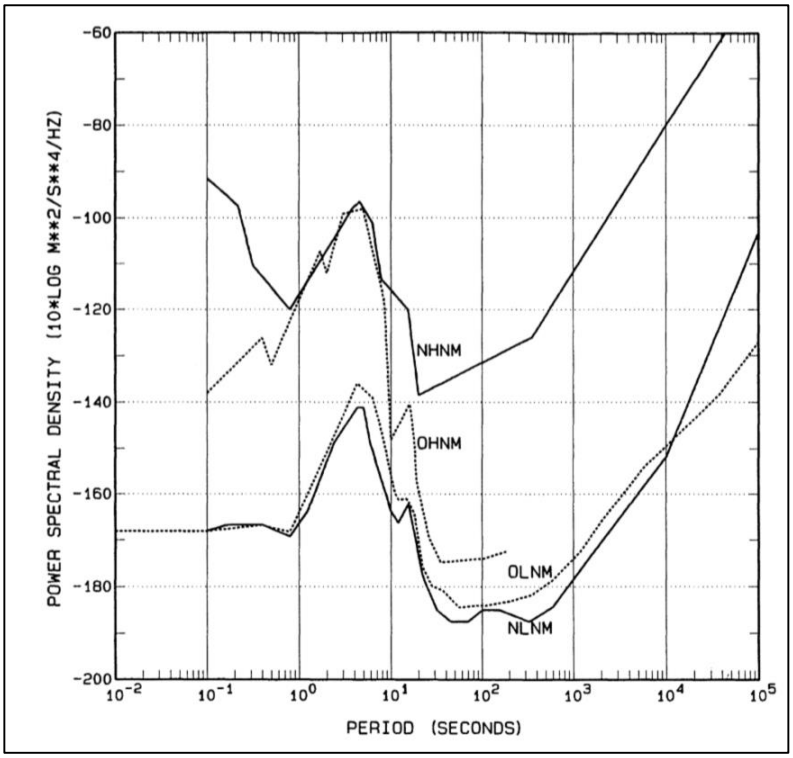

Figure 3-11: Original and New Noise Models [17]

identify the power present across a range of frequencies computed from many geological sites on earth (Figure 3-11). The NLNM represents a theoretical minimum that would not be representative of any one geological site on earth, as it is computed from taking the minimum values over all geological sites used in the study. The NHNM is an average computed from high background noise. One would be able to find sites that exhibit higher and lower ambient noise than that shown by the NHNM [17]. The challenge is that pipeline vibration may be below the ambient noise in certain areas. Therefore certain methods of estimating the transfer function may fail in this scenario. Because one of the unknowns in this research is the strength of vibration of a pipeline, an assumption was made based on these noise models. The experimental setup was accurately scaled to produce an output signal at the geophone such that when the vibration isolation platform used in the experimental setup is enabled the ambient noise is between the

NLNM and the NHNM and is assumed to be representative of a pipeline in a remote location. When the vibration isolation platform is disabled the floor vibration (ambient noise) is above the NHNM, and is assumed to be representative of a pipeline close to cities or locations of high background noise.

CHAPTER 4: SIGNAL PRODUCTION AND SIGNAL PROCESSING

4.1 Signal Production

4.1.1 Pipeline Vibration

4.1.1.1 Introduction to Pipeline Vibration

Pipeline vibration is typically classified as either low-frequency or high-frequency excitation. High-frequency excitation is by convention considered to be greater than 500 Hz [18]. Once the energy is created, amplification of the signal may occur from resonance in either the acoustic or structural domains. Several different mechanisms for both generation and amplification of both high and low-frequency excitations exist. The focus here is on the excitation and amplification mechanisms of both high and low frequencies.

4.1.1.2 High Frequency Pipeline Excitation

Two main sources of high-frequency (>500 Hz) pulsations exist in pipelines; vortex shedding and blade pass excitation [18].

Vortex shedding is an oscillating flow characteristic that occurs when a fluid flows past an object. In the flow, a regular pattern of vortices at the trailing edge of the body are generated. They detach periodically from either side of the body. The alternating vortex shedding creates an alternating pressure field which interacts with the object [19]. A simplified analysis can be performed using the Strouhal number, and the frequency of the vortex shedding can be found from the following equation (4- 1) [18]:

$$f_v = \frac{S\,V}{D_o} \qquad \textbf{(4- 1)}$$

where:

f_v $Vortex\ Shedding\ frequency\ [Hz]$

V $Flow\ Velocity\ \left[\frac{m}{S}\right]$

S $Strouhal\ Number$

D_o $Effective\ Diameter\ of\ the\ Obstruction\ [m]$

The second source of high-frequency excitation is blade pass excitation, also called pocket pass excitation. The term "blade pass excitation" evolved from the action of centrifugal compressors, whereby the compressor blades pass by certain internal components and generate pressure pulses. The term "pocket pass excitation" evolved from the action of screw type compressors; the intermeshing of the male and female lobes generates progressive cavities and modulates the pressure field of the fluid. The frequency of the blade pass excitation can be derived from the number of blades on the impeller wheel of the centrifugal compressor, and the revolutions per minute. For a screw type compressor the excitation frequency can be derived from the number of lobes on the male rotor and the compressor running speed [20]. The following equation describes the frequency of pulsation (4- 2):

$$f_p = n\, N_r \qquad \textbf{(4- 2)}$$

where:

f_p $Pulsation\ Frequency\ [Hz]$

n $Number\ of\ Impeller\ Vanes\ or\ Lobes$

N_r $Rotational\ speed\ [rps]$

The amplitude of pulsation created from vortex shedding and blade pass excitation are generally very small (0.5 psi / 3.5 kPa) [18]. This small amplitude is not enough to cause dangerous vibration levels, or create a significant noise. However, when suitable mechanisms are in place that are able to amplify the small pulsation, larger vibration or noise levels may be reached.

For high frequency excitation the amplification mechanism is the cross wall natural frequency. When the diameter of the pipe is large, the wavelength (distance between pulsations) can become relatively small. If the wavelength becomes smaller than the diameter of the pipe it is possible for the direction of pulsation propagation to become oblique with respect to the longitudinal axis of the pipe. Through wave interference, there is an opportunity for a pressure gradient to form across a section of the pipe. The wave interference pattern is defined as a cross wall mode [18]. The three dimensional wave equation can be simplified to the Bessel function, which can be solved for the propagation of the cross wall modes. The ordered pairs represent respectively the number of radial lines (m = diametrical) and annular circles (n = circumferential). Figure 4-1 shows what the cross section pressure gradients look like for several different modes.

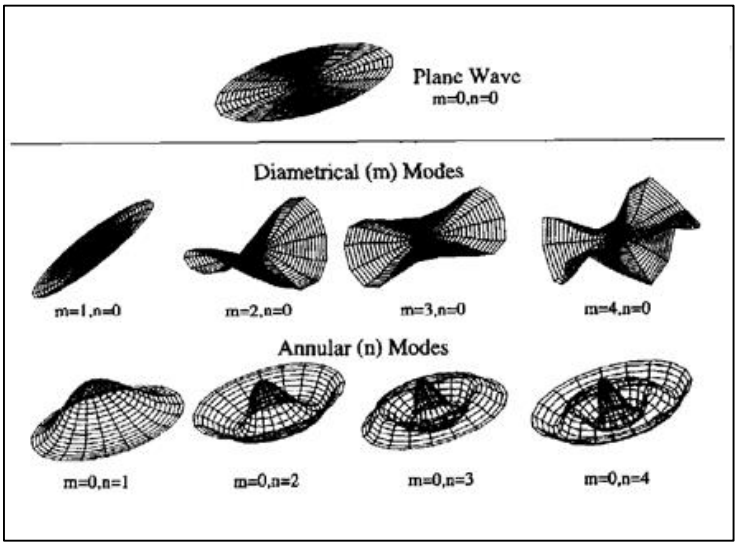

Figure 4-1: Pipe Shell Wall Vibration Mode Shapes [18]

Once the low-amplitude, high-frequency excitation is amplified, it may excite the pipe wall. For high-frequency excitation the pipe wall is excited circumferentially [18]. Stated another way, the circumferential excitation is radial vibration across the pipes cross-section, the pipe may be thought of as "breathing". As the excitation frequency increases, the pipe may begin to vibrate out of phase and produce a sine-wave around the circumference. Figure 4-2 shows what these mode shapes look like through a cross section, as well as a 3 dimensional view of the pipe for i=3 [18].

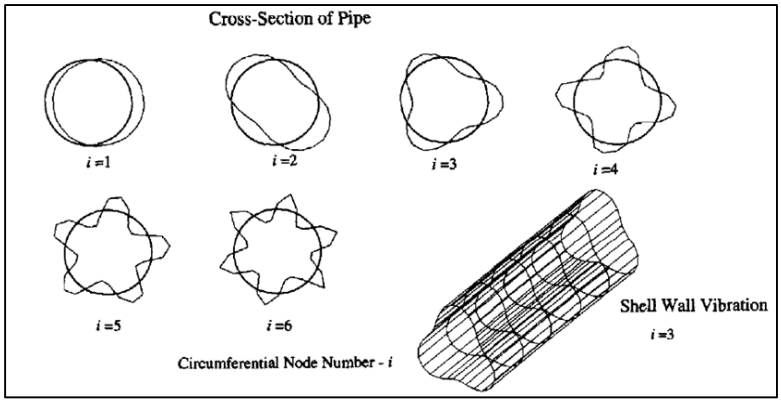

Figure 4-2: Cross Wall Acoustical Mode Shapes [18]

4.1.1.3 Low Frequency Pipeline Excitation

There are a considerable amount of low frequency excitation sources found along pipelines. A short list which is shown below includes vibrations which are [21]:

1) Mechanically induced vibrations due to:

- unbalanced machinery forces related to the speed of the machine and multiples of the running speed due to the use of transmissions

$$f_1 = 1\ N_r \quad \textbf{(4- 3)}$$

$$f_2 = 2\ N_r \quad \textbf{(4- 4)}$$

2) Pulsation induced

- reciprocating pumps

$$f_n = n_m \, N_r \, P \qquad \textbf{(4- 5)}$$

- reciprocating compressors

$$f_n = n_m \, N_r \qquad \textbf{(4- 6)}$$

where:

n_m 1,2,3 ... $(number\ of\ modes)$

P $number\ of\ pump\ pistons$

3) Liquid (or mixed phase) flow excited

- flow disturbance due to quasi-steady flow

$$0\ Hz < f < \ 30\ Hz \qquad \textbf{(4- 7)}$$

Low frequency excitation is considered to be less than 500 Hz. It is possible to have positive displacement pumps and compressors operating below 300 RPM [20], which produce excitation frequencies as low as 5Hz. This confirms that very low frequency vibrations can be present in pipelines, and confirms one of the major driving factors for this research. As in high frequency excitation, there must be a mechanism in place to change the pulsation into a vibration. Cross wall modes are no longer a factor here, because the wavelength is much larger than the diameter of the pipe. The mechanisms in place which translate low frequency pulsation into vibration are called coupling mechanisms [21]. Pressure pulsations may produce vibrations at piping bends, closed pipe sections, valves, orifices, reducers and changes in pipe diameters.

Once the pulsation has produced a vibration it may be amplified in the following way. At low frequencies the pipe is excited laterally along its axis, like a beam. Figure 4-3 shows the modal configuration of the axial excitation.

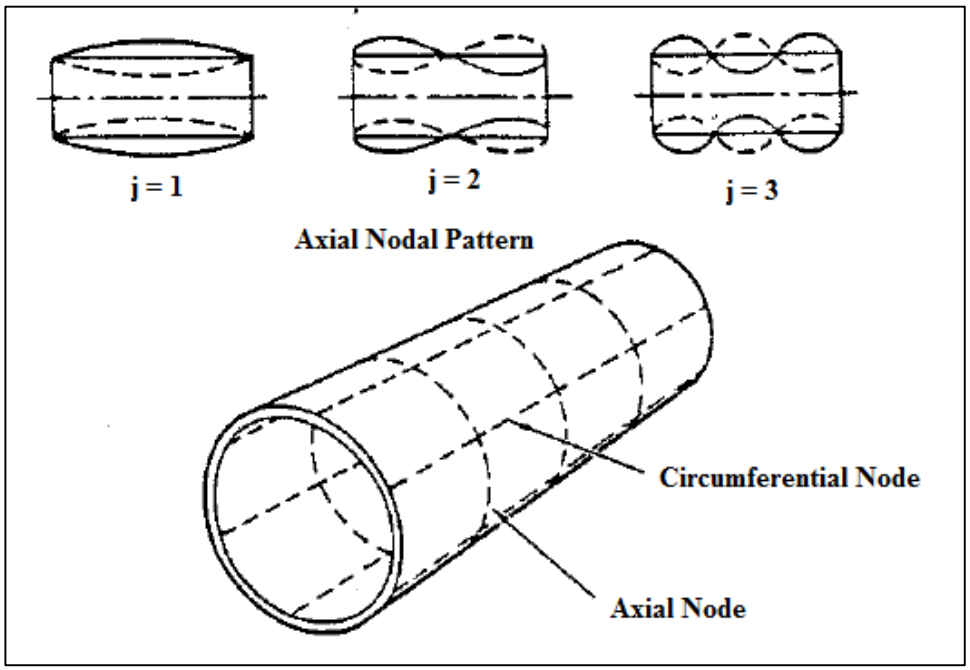

Figure 4-3: Axial Modes for a Simply Supported Cylinder [18], [21]

The natural frequency of the pipe may be found from ideal beam theory. For a straight section of pipe this is:

$$f_o = \frac{\lambda_f}{2\pi}\sqrt{\frac{gEI}{\mu l^4}} \qquad \textbf{(4- 8)}$$

where:

f_0 $Pipe\ span\ natural\ frequency\ [Hz]$

g $Gravitational\ constant\ [9.81\ \frac{m}{sec^2}]$

E $Modulus\ of\ elasticity\ [GPa]$

I $Moment\ of\ inertia\ [m^4]$

l $Pipe\ span\ [m]$

λ_f $Frequency\ factor$

μ $Weight\ per\ unit\ length\ of\ beam\ [\frac{Kg}{m}]$

As a sample calculation, consider a 30 inch (0.762 m) diameter pipeline (the Keystone pipeline as an example) with a 104 ft (31.69 m) straight section. The first fundamental frequency would be found at 5Hz.

4.1.1.4 Turbulence Induced Pipeline Vibration

The proposed method of pipeline leak detection assumes vibrations are present at every point along the pipeline. The locations of pipeline vibration sources are not limited to the vicinity of pipeline pump and compressor stations. A source of pipeline vibration exists in the most remote locations along the pipeline. Because the flow through a pipeline is not steady, a randomly varying pressure field is developed on the inside surface of the pipe. This creates turbulent flow, which causes pipeline vibration. Using of the theory of random vibrations the average of the mean square amplitude of the pipeline response can be calculated.

The square of the amplitude of the response, averaged over a long time segment is defined as the mean square response. If the power spectrum of the surface pressure within the pipe is measured, the pipe natural frequency measured, pipe damping and mode shape measured, the mean square response of the *jth* pipe mode (modes are shown in Figure 4-3) can be found by integrating over the entire frequency range of the response spectrum [19]:

$$Y_{ij}^2 = \psi_j^2(z) \int_{-\infty}^{\infty} S_{L_{ij}}(\omega)\ d\omega \qquad \textbf{(4- 9)}$$

where:

Y_{ij}^2 $Mean\ square\ response\ of\ the\ jth\ pipe\ mode\ in\ the\ ith\ direction$

$S_{L_{ij}}(\omega)$ $Power\ spectrum\ of\ the\ pipeline\ response\ in\ the\ jth\ mode\ in\ the\ ith\ direction$

$\psi_j(z)$ $Spanwise\ mode\ shape$

The power spectrum of the pipeline response is found from the following:

$$S_{L_{ij}}(\omega) = \frac{S_{F_{ij}}(C)}{Z(\omega)^2} \qquad \textbf{(4- 10)}$$

where:

$Z(\omega)^2$ $Impedance\ of\ the\ jth\ \ mode\ of\ the\ pipe$

ω_j $Natural\ frequency\ of\ the\ jth\ mode$

m_m $Modal\ mass\ per\ unit\ length$

ζ $Damping\ of\ the\ jth\ mode\ due\ to\ pipe\ structure, material\ and\ fluid$

$S_{F_{ij}}(\omega)$ $The\ power\ spectrum\ of\ the\ generalized\ force\ in\ the\ the\ jth\ mode\ and\ the\ ith\ direction$

The dynamic response of the pipeline to turbulence is characterized by the general force on each mode in which the pipe responds. The power spectrum of the generalized force in the *ith* direction and the *jth* mode is [19]:

$$S_{F_{ij}}(\omega) = \frac{S_{pi}(\omega) A^2 J_i^2(\omega)}{\left[\int_0^L \psi_j^2\ (x)\ dx\right]^2} \qquad \textbf{(4- 11)}$$

where:

$$J_i^2(\omega) = \frac{\iint_0^A \psi_j(x_1)\ \psi_j(x_2)\ r(x_1, x_2, \omega)\, dA_1\, dA_2}{A^2} \quad Jont\ acceptance\ of\ the\ jth\ mode$$

A $\quad Total\ area\ inside\ the\ pipe\ between\ supports$

$r(x_1, x_2, \omega)$ $\quad Correlation\ factor\ for\ homogeneous\ turbulence$

$S_{pi}(x_1, x_2, \omega)$ $\quad Cross\ spectral\ density\ of\ the\ measured\ turbulance\ at\ two\ points$

The cross spectral density can predict the level of turbulence between two points on the inside surface of the pipe [19].

$$S_{pi}(x_1, x_2, \omega) = \frac{1}{2\pi}\int_{-\infty}^{\infty} \lim_{t_0 \to \infty} \frac{1}{2t_0}\int_{-t_0}^{t_0} p_i(x_1, t) p_i(x_2, t+\tau) e^{-i\omega\tau}\, dt\, d\tau \qquad \textbf{(4- 12)}$$

where:

$p_i(x_1, t)$ $\quad Surface\ pressure\ in\ the\ ith\ direction\ at\ each\ point\ x\ on\ the\ inside\ of\ the\ pipe$

4.1.2 Experimental Excitation

4.1.2.1 Introduction to Experimental Excitation

Two types of experimental excitation were investigated; sinusoidal and broadband excitation. The sinusoidal excitation was investigated first to confirm that the excitation was retrievable and not buried in the ambient noise. A very small excitation was used, and the setup is described in Section 5.2.1, the results are shown in Section 5.4. The broadband signal was used to generate excitation through a range of frequencies, as this is a necessary requirement to produce a meaningful transfer function. The experimental setup is described in Section 5.2.2, and the results are shown in Section 5.4. Several considerations are given to the generated signal using LabVIEW.

4.1.2.2 Excitation Filtering

For broadband excitation a filter is applied to assist in the parametric identification method of PSD estimation. It was found that an elliptic filter applied to the input assisted in achieving an optimal result via the parametric method of estimating the transfer function. Figure 4-4 shows the control panel of the software package used to create the input excitation. For generating white noise the amplitude was controlled by the sliders labelled "Amplitude" and "Noise Level". The purpose of filtering the excitation was to concentrate the energy of the excitation into the band of interest. This was 20-300 Hz for most tests reported in this research.

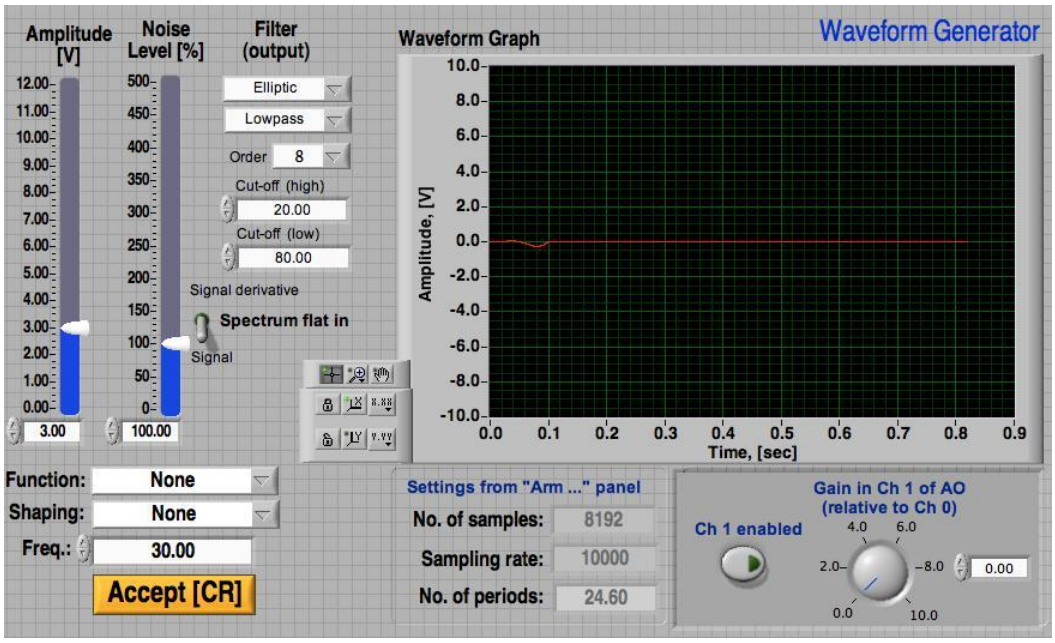

Figure 4-4: LabVIEW Input Terminal for Experimental Excitation

4.2 Signal processing

4.2.1 Signal Processing Software

4.2.1.1 Introduction

Power spectral density (PSD) plots identify the frequencies which contain power within a signal. The methods used to produce a PSD plot belong to a class of mathematics known as Digital Spectral Analysis. More generally, "spectral analysis is any signal processing method that characterizes the frequency content of a measured signal" [14].

Two classical methods of estimating the PSD are the periodogram and the correlogram. With the advent of the Fast Fourier Transform (FFT) and signal processing integrated circuits, the periodogram has become the most widely used method. The FFT is not a type of Fourier Transform; rather an algorithm to compute the Discrete Time Fourier Transform (DTFT). Both the periodogram and correlogram method of PSD estimation will be explored here, and what information is available from each method. The major difference between the two methods of estimation is that the correlogram first estimates the autocorrelation sequence before applying the FFT, and the periodogram acts directly on the data set to estimate the PSD. The PSD's are then used to obtain a transfer function of the system.

Another distinctive signal processing scheme known as parametric estimation will also be employed in this research. This latter scheme will be used to compute the transfer function directly. In statistics this method is known as auto regressive moving average (ARMA) analysis, and does not use the FFT in any way, rather it acts only on the time domain signals.

A flowchart which gives the high level description of the experimental procedure used in this research is provided in appendix A (Process Flowchart for Experimental Leak Detection). This flowchart references the detailed procedure via flowcharts for the individual methods themselves: periodogram, correlogram and parametric methods (Appendix B,C and D respectively).

4.2.1.1.1 Nyquist critical frequency

All of the methods for investigating the frequency content of a signal used in this research require the use of data acquisition hardware. The use of modern data acquisition hardware involves the digitization (amplitude) and sampling (time) of a continuous signal. A very important rule which cannot be violated during this process is known as the Nyquist critical frequency. The Nyquist criterion states that the sampling frequency must be at least twice that of the maximum frequency to be observed in the signal. If this requirement is violated aliasing will occur. Figure 4-5 shows what an under sampled signal will look like. The signal is represented at a much lower frequency, and erroneous results are presented. Aliasing cannot be detected once the signal is sampled and the transfer function obtained will be of no value.

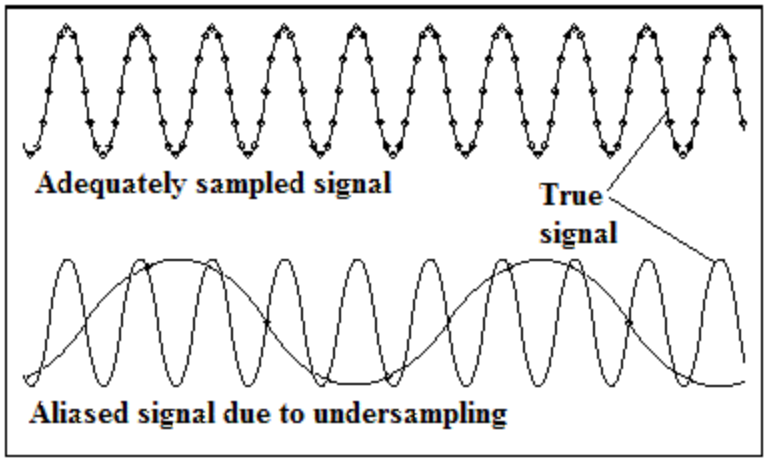

Figure 4-5: Adequate and inadequate sampling rates [22]

4.2.1.1.2 Discrete Fourier Transform (DFT) pairs

The Fourier Transform converts a time domain signal into its equivalent frequency domain representation. There are several ways of expressing the DFT, often seen in different scientific and technical fields. The following is typically used in signal processing [14].

$$X[s] = \mathrm{T}\sum_{n=1}^{N} x[n]e^{-2\pi isn/N} \quad \textbf{(4- 13)}$$

$$x[n] = \frac{1}{N\,T}\sum_{s=1}^{N} X[s]e^{2\pi isn/N} \quad \textbf{(4- 14)}$$

where:

$X[s]$ $Discrete\ Fourier\ Transform\ of\ x[n]$

$x[n]$ $Inverse\ Discrete\ Fourier\ Transform\ of\ X[s]$

N $Total\ number\ of\ sample\ points$

T $Total\ sampling\ interval$

4.2.1.1.3 Parseval's Theorem

The total power contained within a signal is the same regardless of computation in the time or frequency domain. Comparing this power obtained in the time domain and in the frequency domain gives an estimate of the PSD quality. If, for example, the power in the frequency domain is significantly different from that in the time domain, the PSD reliability would be considered low. This method of estimating the accuracy and reliability of the PSD will subsequently be used, and is known as Parcival's Theorem [14]:

$$Total\ Power \propto \sum_{n=0}^{N-1} |x[n]|^2 = \frac{1}{N} \sum_{s=0}^{N-1} |X[s]|^2 \quad \textbf{(4- 15)}$$

4.2.1.2 Periodogram Method of PSD Estimation

The Power Spectral Density is defined as the Discrete Fourier Transform (DFT) of the Autocorrelation sequence [14]:

$$P_{xx}(f) = T \sum_{n=-\infty}^{\infty} \left(r_{xx}[m] e^{-2\pi i f m T}\right) \quad \textbf{(4- 16)}$$

where:

$P_{xx}(f)$ $Power\ spectral\ density\ of\ the\ input$

$r_{xx}[m]$ $Autocorrelation\ sequence\ (input)$

f $frequency\ in\ Hertz$

The inverse DTFT of the above Power Spectral Density recovers the Autocorrelation sequence:

$$r_{xx}[m] = \int_{-\frac{1}{2}T}^{\frac{1}{2}T} P_{xx}(f) \mathrm{e}^{(2\pi i f m T)}\, df \quad \textbf{(4- 17)}$$

The above pair of transforms is known as the Wiener-Khintchine theorem [14]. The above definitions of the PSD are based on ensemble averages. However in reality one does not have an ensemble of waveforms which can be used to estimate an average. It becomes apparent that time averaging, in place of ensemble averaging is required. This property is known as ergodocity: "A random process is said to be ergodic if, with probability 1, all its statistics can be predicted from a single waveform of the process via time averaging; that is, the time averages of almost all possible single waveforms are equal to the same constant (the ensemble average)" [14].

Based on the Wiener-Khintchine theorem, for an ergodic process/signal the periodogram PSD estimator is [14]:

$$P_{xx}(f) = \lim_{n\to\infty} E_v \left\{ \frac{1}{(2N+1)T} \left| T \sum_{n=-N}^{N} \left(x[n] \mathrm{e}^{(-2\pi i f n T)} \right) \right|^2 \right\} \qquad \textbf{(4- 18)}$$

where:

E_v *Expected value operator*

If the expected value operator is ignored, and a finite data set of N is substituted (x[0],….,x[N-1]), the PSD is [14]:

$$P_{xx}(f) = \frac{T}{N} \left| \sum_{n=0}^{N-1} \left(x[n] \mathrm{e}^{(-2\pi i f n T)} \right) \right|^2 \qquad \textbf{(4- 19)}$$

When the expected value operator is ignored, the periodogram PSD estimate yields inconsistent results. It is therefore necessary to use "pseudo ensemble averaging" to smooth the results. The three types of averaging schemes most commonly used are summarized in Table 4-1.

Table 4-1: Periodogram Averaging Schemes

Daniell	Will smooth the periodogram by calculating an average over several adjacent frequency bins.
Bartlett	Calculates an average from multiple periodograms from segments of the data sequence.
Welch	Extended Bartlett method; overlaps the segments and uses windowing.

There are other methods available to smooth the data, however they are usually restricted to specific types of signals. The three methods shown above are considered to be the most robust

methods for smoothing the periodogram. After a method is chosen the final step is to use the Fast Fourier Transform (FFT) to compute the periodogram.

As it will be subsequently shown, to obtain a properly scaled PSD estimate, the following expression using the noise power bandwidth of the window has to be employed.

$$Scaled\ P_{xx}(f) = \frac{P_{xx}(f)}{Noise\ Power\ bandwidth\ of\ weighting\ window} \qquad \textbf{(4- 20)}$$

4.2.1.2.1 Using Weighting Windows

The Welch method employs "time domain weighting windows", which is the common practice when using the FFT. These windows (e.g. Hanning, Bartlett etc.) reduce spectral leakage (side lobes) in the periodogram PSD estimate. To reduce the PSD estimator variance in the correlogram method similar windows are used, termed "lag windows" [14]. Spectral leakage distorts the data such that energy from one frequency component is spread to an adjacent frequency. Spectral leakage is a result of passing the FFT a non-integer number of cycles. Consequently, the FFT assumes that the time record is repeated throughout all time [22]. However, in most cases the signal being acquired is continuous, it is present before, during and after the sampling, and an integer number of cycles is are not acquired. It is therefore necessary to force periodicity by windowing the data.

Figures 4-6 and 4-7 show the effects on the FFT output from three common windows applied to a sample data set [22]. In Figure 4-6 the FFT is passed an integer number of cycles; the uniform window has the narrowest lobe and the Hann and flat top windows introduce some spreading. In

this instance it would be best to use no window (uniform), as it gives the best resolution. The spectral resolution is limited to the width of the main lobe.

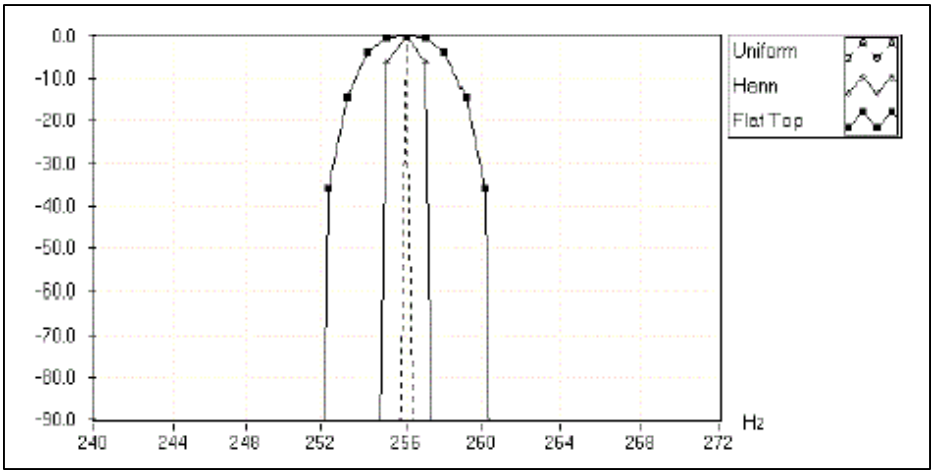

Figure 4-6: Three windows with an integer number of cycles [22]

In the case where the FFT is passed a non-integer number of cycles, the advantage of windowing becomes apparent, as shown in Figure 4-7. Here, the uniform window is outperformed in terms of spectral leakage by the Hann and Flat top windows. The ability to detect two closely spaced frequency components is increased as the width of the main lobe decreases and spectral resolution increases.

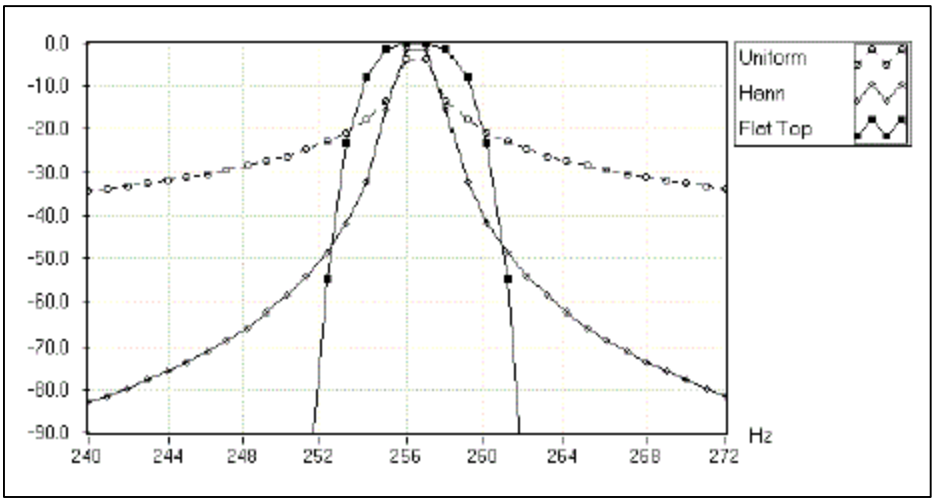

Figure 4-7: Three windows with a non-integer number of cycles [22]

4.2.1.2.2 Zero Padding and Segment Averaging

Zero padding is the process of adding zeros to both sides of the time series data, which artificially increases the resolution of the PSD. This is because the resolution of the PSD is related to the total length of the record.

Segment averaging is used in the Welch method of PSD estimation by computing several PSD's from the data using a 50% overlap between segments. The process is shown in the periodogram flowchart in Appendix B, where several PSD's are averaged to compute a single result with a lower variance than any segment could produce on its own. This flowchart outlines the method used in this research to experimentally obtain the data, and numerically obtain the periodogram PSD estimate and transfer function.

4.2.1.2.3 Transfer Function Magnitude Obtained from Periodogram PSD Estimate

Considered is a dynamic system whose inputs x(t) and output y(t) are known. The gain of the transfer function of this system can be found as:

$$T_{pg}(f) = \sqrt{\frac{Abs(P_{yy}(f))}{Abs(P_{xx}(f))}} \quad \textbf{(4- 21)}$$

where:

$T_{pg}(f)$ $Gain\ of\ the\ transfer\ function\ obtained\ from\ periodogram\ based\ PSD's$

$P_{yy}(f)$ $Power\ Spectral\ Density\ of\ the\ output\ signal$

$P_{xx}(f)$ $Power\ Spectral\ Density\ of\ the\ input\ signal$

4.2.1.3 Correlogram Method of PSD Estimation

The correlogram first estimates the autocorrelation sequence, or the cross-correlation sequence before applying the FFT to estimate the PSD and cross PSD respectively. The Autocorrelation sequence of a discrete random variable at two different time indices is defined as [14]:

$$r_{xx}[n_1, n_2] = E_v\{(x[n_1]x^*[n_2])\} \quad \textbf{(4- 22)}$$

where:

$x[n]$ $discrete\ random\ variable\ x\ at\ time\ index\ n$

$*$ $complex\ conjugate$

A random process is defined as wide sense stationary if its mean is constant, and the autocorrelation is a function of only the difference in time indices: $m = n_2 - n_1$.

The cross-correlation sequence of two discrete random variables at two different time indices is defined as [14]:

$$r_{xy}[n_1, n_2] = E_v\{(x[n_1]y^*[n_2])\} \quad \textbf{(4- 23)}$$

where:

$y[n]$ $discrete\ random\ variable\ y\ at\ time\ index\ n$

Under the assumption of an ergodic signal the autocorrelation sequence becomes:

$$r_{xx}[m] = E_v\{(x[n+m]x^*[n])\} = \lim_{m\to\infty} \frac{1}{2M+1} \sum_{n=-M}^{M} (x[n+m]x^*[n]) \quad \textbf{(4- 24)}$$

$$= \frac{1}{(N-m)} \sum_{n=0}^{N-m-1} (x[n+m]x^*[n]) = r_{xx}[m]$$

where:

N *Number of samples*

The unbiased estimators used for the autocorrelation and cross-correlation are summarized as follows [14]:

$$r_{xx}[m] = \begin{cases} \dfrac{1}{(N-m)} \displaystyle\sum_{n=0}^{N-m-1} (x[n+m]x^*[n]), & 0 \le m \le N-1 \\ \dfrac{1}{(N-|m|)} \displaystyle\sum_{n=0}^{N-|m|-1} (x[n+|m|]x^*[n]), & -(N-1) \le m \le 0 \end{cases} \quad \textbf{(4- 25)}$$

$$r_{xy}[m] = \begin{cases} \dfrac{1}{(N-m)} \displaystyle\sum_{n=0}^{N-m-1} (x[n+m]y^*[n]), & 0 \le m \le N-1 \\ \dfrac{1}{(N-|m|)} \displaystyle\sum_{n=0}^{N-|m|-1} (x[n]y^*[n+|m|]), & -(N-1) \le m \le 0 \end{cases} \quad \textbf{(4- 26)}$$

The most general form of the correlogram method of PSD estimation as well as cross PSD estimation are shown below; these equations are computed via the FFT. The equations shown include a windowing term which reduces the effects of essentially convolving the true PSD with the transform of the discrete time rectangular window.

$$P_{xx}[f] = T \sum_{m=-L}^{L} \omega[m] r_{xx}[m] \mathrm{e}^{(-2\pi i f m T)} \quad \textbf{(4- 27)}$$

$$P_{xy}[f] = T \sum_{m=-L}^{L} \omega[m] r_{xy}[m] e^{(-2\pi i f m T)} \quad \textbf{(4- 28)}$$

where:

$P_{xx}[f]$ *Power Spectral Density of the input signal*

$P_{xy}[f]$ $Cross-power\ spectral\ density\ estimate$

$\omega[m]$ $an\ odd\ length\ (2L+1)\ lag\ window$

The process flowchart for the correlogram method of PSD estimation is included in Appendix C. This flowchart outlines the method used in this research to experimentally obtain the data, and numerically obtain the Correlogram PSD estimate and transfer function.

4.2.1.3.1 Transfer Function Obtained from Correlogram PSD Estimate

The correlogram transfer function gain is computed from the following ratio [23]:

$$T_{cg}(i) = \frac{P_{xy}(i)}{P_{xx}(i)} \quad \textbf{(4- 29)}$$

where:

T_{cg} $Gain\ of\ the\ transfer\ function\ obtained\ from\ correlogram\ based\ PSD's$

The phase of the transfer function is found from the following [23]:

$$T_{cp}(i) = Arg(\frac{P_{xy}(f)}{P_{xx}(f)}) \quad \textbf{(4- 30)}$$

where:

T_{cp} $Phase\ of\ the\ transfer\ function\ obtained\ from\ correlogram\ based\ PSD's$

4.2.1.4 Parametric Estimation

4.2.1.4.1 Introduction

Spectral analysis methods described in the preceding sections have significant weaknesses when applied to stochastic signals associated with the dissipation of energy generated from pipelines. Therefore, the application of these methods in the leak detection and quantification may yield

unsatisfactory results. A diametrically different approach described in this section and referenced henceforth as parametric identification is inherently designed to cope with stochastic and complex signals.

The fundamental assumption is the existence of a cause-and-effect relationship between the input and the output of the investigated system. Stated in Section 3, the system under investigation is defined in this research as the "signal channel". This hypothetical relationship is defined either by the impulse response g(t) or the transfer function of the channel G(s). Of particular interest is the model given by Equation 3-5; a scalable transfer function whose order and coefficients must be estimated. Consequently, the estimation procedure to be employed is classified as both "model based" and "parametric".

4.2.1.4.2 Parametric Estimate of the Transfer Function

The assumed cause-and-effect relationship described by Equation 4-3 of a continuous-time dynamic system is used to obtain an equivalent discrete-time system described by transfer function G(z) [24].

$$s \rightarrow \frac{2}{T_i}\,\frac{1-z^{-1}}{1+z^{-1}} \tag{4- 31}$$

$$G(s) \rightarrow G(z) = \frac{Y(z)}{U(z)} = \frac{b_1 z^{-1} + \cdots + b_m z^{-m}}{1 + a_1 z^{-1} + \cdots + a_m z^{-m}} \tag{4- 32}$$

where:

$Y(z)$ $z\ transform\ of\ the\ output\ signal$

$U(z)$ $z\ transform\ of\ the\ input\ signal$

T_i $Sampling\ interval$

z $Forward\ time\ shift\ operator$

$a_i\ , b_j$ $Parameters\ in\ the\ discrete\ time\ transfer\ function$

Applying the inverse z transformation to Equation 4-32 yields the difference equation [24]:

$$y(k) + \hat{a}_1 y(k-1) + \cdots + \hat{a}_m y(k-m) - \hat{b}_0 u(k-1) - \cdots - \hat{b}_m u(k-m) = e(k) \quad \textbf{(4- 33)}$$

where:

$e(k)$ $Error\ due\ to\ shifted\ parameter\ estimate$

From this equation, the estimate of y(k) from time k-1 can be made. This estimate $\hat{y}(k|k-1)$, can be considered a one step ahead prediction.

$$\hat{y}(k|k-1) = -\hat{a}_1 y(k-1) - \cdots - \hat{a}_m y(k-m) + \hat{b}_1 u(k-1) + \cdots + \hat{b}_m u(k-m) = \psi^T(k)\hat{\theta} \quad \textbf{(4- 34)}$$

where:

$\psi^T(k)$ $Data\ Vector = [-y(k-1) \ldots - y(k-m)\ , u(k), u(k-1) \ldots u(k-m)]$

$\hat{\theta}^T$ $Parameter\ Vector = \left[\hat{a}_1 \ldots \hat{a}_m\ , \hat{b}_0 \ldots \hat{b}_m\right]$

The equation error becomes the difference between the new measurement and the one step ahead measurement from the model, as shown below.

$$e(k) = y(k) - \hat{y}(k|k-1) \quad \textbf{(4- 35)}$$

The inputs and outputs are measured for k = m, m+1,…,m+N. From this there are N+1 equations with the following form:

$$\hat{y}(k) = \psi^T(k)\hat{\theta} + e(k) \quad \textbf{(4- 36)}$$

The least squares method minimizes the loss function:

$$V(\hat{\theta}) = e^t(k)e(k) = \sum_{k=m}^{k=m+N} e^2(k) \quad \textbf{(4- 37)}$$

by finding a set $\hat{\theta}$ for which:

$$\left.\frac{dV}{d\hat{\theta}}\right|_{\theta=\hat{\theta}} = 0 \quad \textbf{(4- 38)}$$

This is a classic problem in statistics whose solution for the parameter vector involves the pseudo inverse of the data matrix [24]:

$$P(k) = [\psi^T(k)\psi(k)]^{-1} \quad \textbf{(4- 39)}$$

The solution then becomes:

$$\hat{\theta} = P(k)\psi^T(k)y(k) \quad \textbf{(4- 40)}$$

The process flowchart for the parametric method of estimating the transfer function is included in Appendix D. This flowchart outlines the method used in this research to experimentally obtain the data, and numerically obtain the parametric estimate of the transfer function, where both the gain and phase are available.

4.2.2 Signal Processing Hardware

4.2.2.1 Introduction to MEMS Ultra-Sensitive Sensors

Micro-Electro-Mechanical Systems (MEMS) are devices whose features range from 1 to 100 µm [25]. MEMS devices are applicable to several engineering disciplines, such as mechanical, electrical, and materials engineering, to name a few. MEMS can be divided into two categories; sensors and actuators. "Sensing can be broadly defined as energy transduction processes that result in perception, whereas actuation can be defined as energy transduction processes that produce actions" [4].

In this research it is important to realize the differences between accelerometers, geophones, and seismometers, which are collectively referred to as inertial sensors. The defining characteristic of a seismometer is its very high sensitivity compared to other devices. However, the function of the device often dictates the designation. For example, devices used to measure ground movement are classified as seismometers and geophones, a geophone used under water is called a hydrophone. Geophones and seismometers typically measure velocity, however, advanced versions can provide the acceleration signals as well. Similarly, while the primary quantity measured by accelerometers is the acceleration of motion, they can also provide the velocity signal on the output.

Recent advancements in MEMS fabrication techniques have enabled the fabrication of sensors with sensitivities improved as much as 100 times when compared to versions available on the market today [25]. Figure 4-8 is a power spectral density plot showing the improved sensitivity of emerging sensors. The emerging sensors are shown with acceleration readings of -180

$g/\sqrt{Hz}$ dB, which is 1 $ng/\sqrt{Hz}$ on a linear scale. Sensitivity is defined as the ratio between the magnitude of the output signal and the magnitude of the input stimulus [4]. The requirements of emerging MEMS devices are nano-g sensitivity, which is very demanding for traditional sensing schemes. Such a large improvement of a sensors sensitivity allows much smaller signals to be measured, along with much greater accuracy and precision. Since MEMS devices are operated in

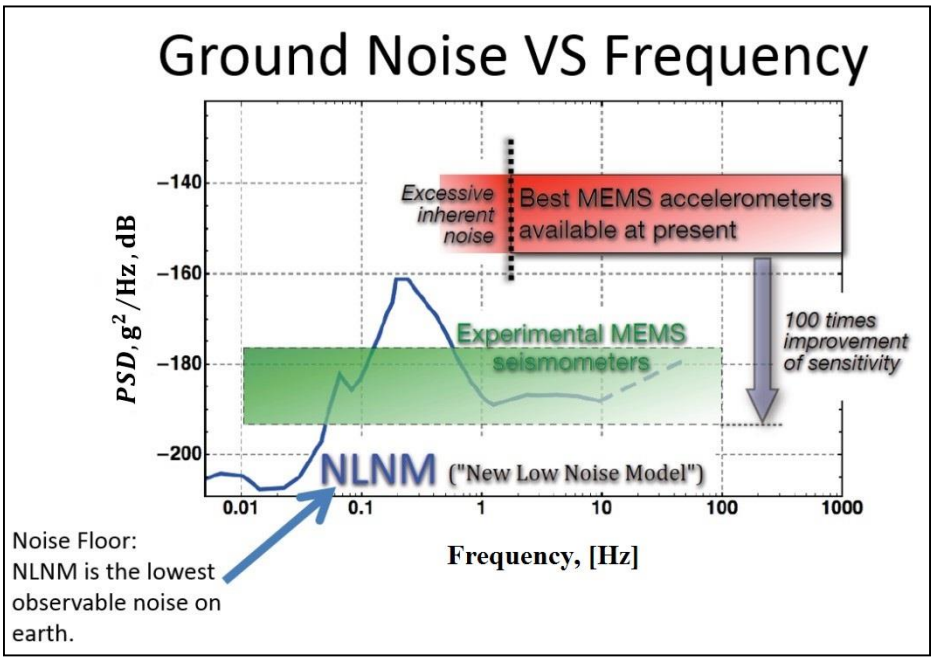

Figure 4-8: Experimental MEMS Seismometers

gases at normal pressures, the small moving parts are vulnerable to molecular agitation. If the sensor is designed for low level signals, this thermal-mechanical noise can be the limiting noise component [26]. In other words, the noise floor determines the sensitivity of the device. Brownian motion is usually the main source of thermal-mechanical noise. "Here, the agitation of an observable object is caused by molecular collisions from a surrounding gas or liquid and the agitation is directly related to the fluid's viscosity" [26]. Because the sensitivity of emerging MEMS devices are close to their thermal-mechanical noise floors (nano-g sensitivity, $1\ nG = 9.81 * 10^{-9}\ \mathrm{m}/s^2$), new challenges are created in the design of the device. The fundamental

challenges are designing very high sensitivity devices with low thermal-mechanical noise floors, low "1/f noise" [27], and a low resonance frequency. The 1/f noise is a result of conductance variation when current passes through a resistor, and is commonly referred to as flicker noise or pink noise [4]. Because the emerging MEMS seismometers have a low frequency requirements (< 100 Hz), there is an additional demand to be met. It is desirable to design the device with its resonance frequency close to the frequency of the signal being detected. For sensors with low damping the resonance frequency is:

$$\omega_r \simeq \omega_n = \sqrt{\frac{k}{m}} \qquad \textbf{(4- 41)}$$

where

ω_r $Resonance\ frequency$

ω_n $Natural\ Frequency$

k $Spring\ Constant$

m $mass$

Therefore a large proof mass is required and the spring stiffness minimized, which makes for a very delicate device. It is reported that one advancement in MEMS manufacturing has accommodated this demand: "Here we had to push our fabrication limits using a combination of surface micro machining and Deep Reactive Ion Etching (DRIE)" [27].

Traditional sensing schemes such as electrostatic, and piezoelectric are inadequate for nano-g sensitivity; optical sensing techniques are advantageous because optical performance approaches the Brownian noise limits of the mechanical device [27].

4.2.2.2 Optical MEMS Sensing Methods

The relative advantages and disadvantages of optical sensing devices are summarized in Table 4-2. Traditional sensing methods are discussed in Section 2.1.

Table 4-2: Comparison of Traditional and Optical Sensing Methods

Sensing Method	**Advantages**	**Disadvantages**
Electrostatic Sensing	- Simple materials - Requires low current and low voltage - Fast Response	- For sufficient capacitance a larger footprint is required - Elaborate readout electronics - Susceptible to error from humidity and particles
Piezoelectric Sensing	- Passive electronics – no power required	- Suitable for low temp applications - Complex growth of crystals
Optical Sensing	- Very high sensitivity - High accuracy - Low noise	- Difficult to achieve smooth finish on micro machined parts - Difficult to create certain lenses

4.2.2.2.1 Accelerometer with Optical Diffraction Grating

Figure 4-9 is one example of an emerging 3-axis MEMS ultra-sensitive accelerometer. Using an optical diffraction grating and a large proof mass (2 grams [27]), a very low thermo-mechanical noise floor was achieved; 0.5 $ng/\sqrt{Hz}$ [28].

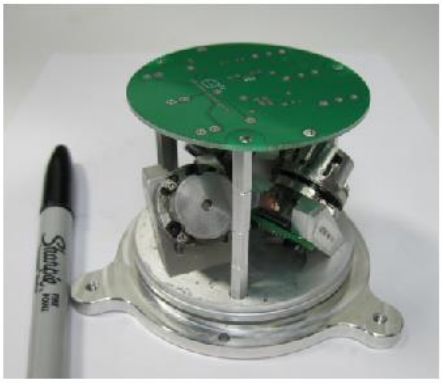

Figure 4-9: Silicon Audio's GeoLight Prototype [28]

Figure 4-10 shows a vertical cavity surface emitting laser (VCSEL) which illuminates the silicon diffraction grating. A percentage of the light reflects directly off of the grating fingers and the rest of the light passes through the grating and reflects off of the moving proof mass, to accrue additional phase; the beams are received by the photo detectors. A diffracted field results, as

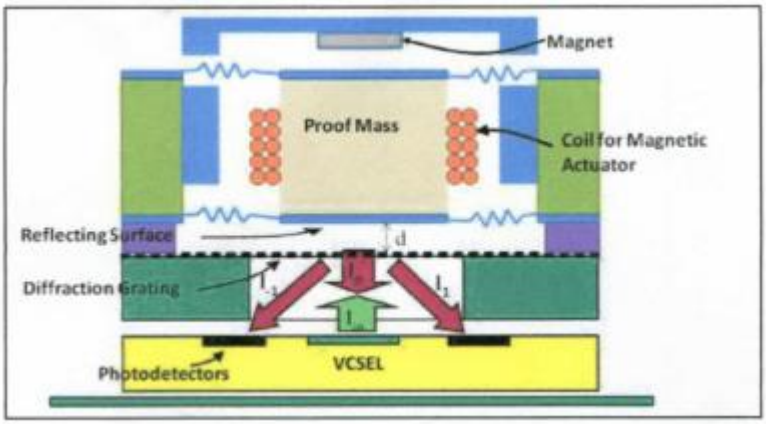

Figure 4-10: Schematic of MEMS Optical Diffraction Grating Sensing Scheme [28]

shown in Figure 4-11. The field is modulated with respect to the separation between the moving proof mass and the stationary diffraction grating. When a coherent light source is incident on the grating and proof mass, the reflected light is diffracted into zeroth order and odd orders [29].

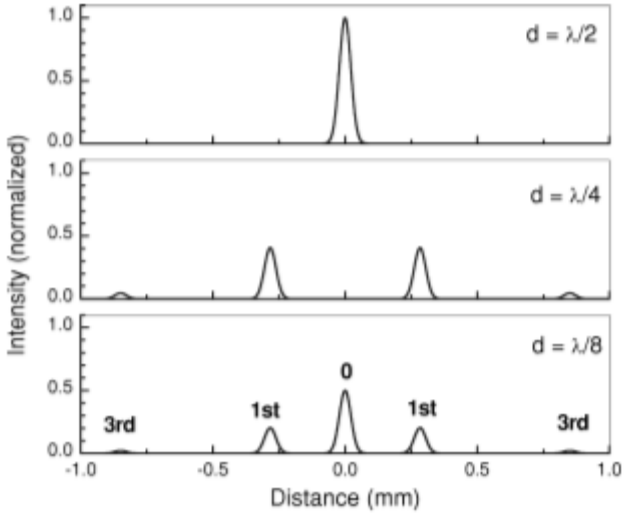

Figure 4-11: Intensity Distribution on Photo Detector Plane for Different Separations [34]

Any of the diffraction gratings can be used to measure the displacement of the proof mass with inferometric resolution. From Figure 4-11, the central beam spot disappears when the separation is equal to $\lambda/4$. The energy is divided between the first and other odd order components. The diffraction grating shown in Figure 4-10 uses a 50% fill factor which is formed directly on the surface of the silicon. The diffraction order intensities can be estimated as follows [29]:

$$I_0 = I_{in}\, cos^2\left(\frac{2\pi d}{\lambda_o}\right) \qquad \textbf{(4- 42)}$$

$$I_{\pm 1} = \frac{4I_{in}}{\pi^2} sin^2\left(\frac{2\pi d}{\lambda_o}\right) \qquad \textbf{(4- 43)}$$

where:

I_0 $Zeroth\ diffraction\ order\ intensity$

$I_{\pm 1}$ $First\ diffraction\ order\ intensity$

I_{in} $Incident\ laser\ intensity$

λ_o $Optical\ Wavelength$

d $Distance\ between\ proof\ mass\ and\ diffraction\ grating$

4.2.2.2.2 Accelerometer with a Fabry Pérot Resonant Optical Cavity

Figure 4-12 shows another example of an emerging MEMS ultra-sensitive accelerometer. Using a resonant optical cavity as an acceleration sensing device, with a 1 gram proof mass, the demonstrated noise performance was 10 $ng/\sqrt{Hz}$ [25]. The theoretical noise performance is 0.5 $ng/\sqrt{Hz}$. Table 4-3 summarizes the discrepancies between the demonstrated and theoretical performance.

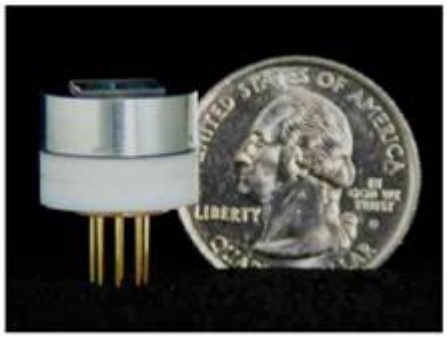

Figure 4-12: Symphony Acoustic's Optical Resonant Cavity Accelerometer [25]

Table 4-3: Sources of noise between demonstrated and theoretical performance

Shot noise of the photo detector	Produced from the quantum fluctuation of current due to the discrete passage of charges [4]
The resistor Johnson noise	Due to random thermal fluctuations of internal electrons and particles, Johnson noise follows a Gaussian distribution [4]
The Laser phase noise	"quantum noise; spontaneous emission of gain medium into the resonator modes" [30]
The Laser 1/f noise	Conductance fluctuation as current flows through a resistor [4]

There exists a difference between a Fabry Pérot Inferometer (Fabry Pérot Resonant Optical Cavity) and something known as a optically-resonant etelon, sometimes called a Fabry Pérot etelon. The difference being the cavity length is adjustable in the Fabry Pérot Resonant Optical Cavity, and it is not in an etelon [31]. Figure 4-13 shows the method for detecting acceleration.

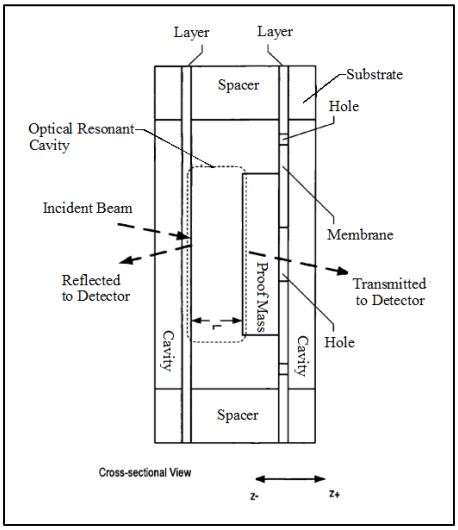

Figure 4-13: Symphony Acoustic's Accelerometer Optical Resonant Cavity [31]

The optical resonant cavity is shown separated by a distance L; one half of the cavity is the surface of the proof mass and the other is the opposing surface labelled "Layer". Both surfaces are partially reflective. The Fabry Pérot Resonant Optical Cavity splits the incident beam into two beams; reflected and transmitted. The characteristics of the transmitted and reflected beams depend on the cavity length L. The beams are sent to optical detectors, as shown in Figure 4-14,

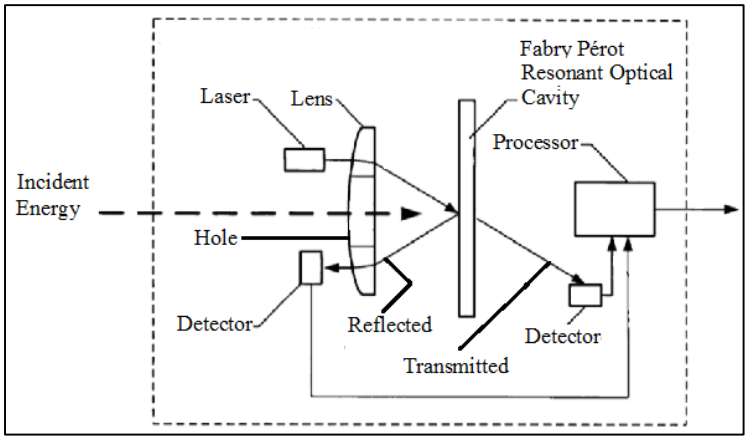

Figure 4-14: Symphony Acoustic's Accelerometer Block Diagram [31]

where both beams create an electrical signal based on the light intensity, which is used by the processor to determine acceleration. This is a major advancement in the field of optical MEMS,

until recently only a single beam was used. This advancement ensures that no optical energy is wasted, and as a result the signal to noise ratio is improved [31]. From Figure 4-13, notice that only one side of the optical cavity has a proof mass (made of glass and the outside surface coated with dielectrics or semiconductors so that it is partially reflective), this mass is mechanically coupled to the membrane of the supporting layer, and the opposing layer is also a membrane. To allow the incident energy to pass through unimpeded there are holes and cavities in the substrate. As the sensor is affected by an acceleration, a force acts on the proof mass, one half of the optical cavity is deflected, changing the cavity length L. The opposing side without a mass is deflected a negligible amount because it's mass is not great enough. The z direction shown in Figure 4-13 is the sensitive axis to acceleration.

The change in cavity length changes the intensity of the reflected and transmitted beams. From Figure 4-15, the incident beam is shown reflecting and transmitting down the length of the optical cavity. The transmitted field can be found by adding the individual contributions from each transmitted wave. To accomplish this, the relative phases and amplitudes are required [32].

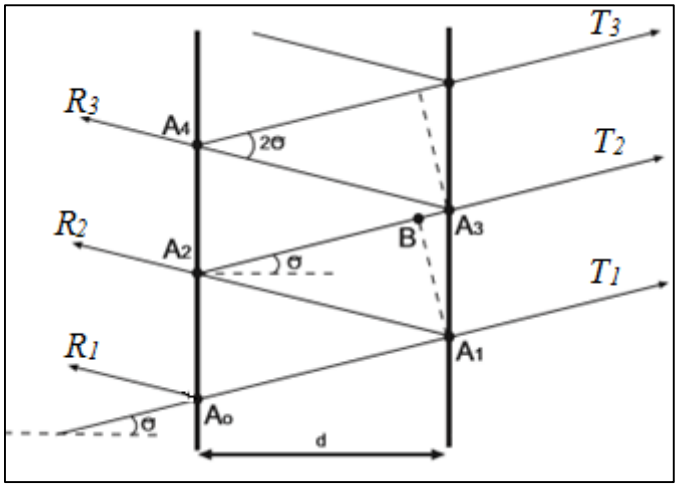

Figure 4-15: Multiple-Beam Interference in a Fabry Pérot Optical Cavity [33]

The phase difference between each transmitted wave is related to the difference in their paths. The path difference *p* between beams T1 and T2 can be seen in Figure 4-15.

$$p = A_1A_2 + A_2B \quad \textbf{(4- 44)}$$

where:

$$A_2B = A_1A_2\,cos(2\theta) \quad \textbf{(4- 45)}$$

Substituting Equation 4-46 into Equation 4-45 yields:

$$p = A_1A_2\,(1 + cos(2\theta)) \quad \textbf{(4- 46)}$$

$$p = A_1A_2\,(2cos^2(\theta)) \quad \textbf{(4- 47)}$$

substituting:

$$d = A_1A_2\,cos(\theta) \quad \textbf{(4- 48)}$$

into Equation 4-47 yields:

$$p = 2d\,cos(\theta) \quad \textbf{(4- 49)}$$

Each reflective surface has its own transmission and reflection amplitude coefficient. Consider a wave travelling from the medium toward the cavity, the reflection and transmission amplitude coefficients are r_1 and t_1. For a wave traveling from the cavity toward the medium, the reflection and transmission amplitude coefficients are r_2 and t_2. "The transmission coefficient is the fraction of the incident electric field that is transmitted and the reflection coefficient is the fraction that is reflected" [33]. The electric field amplitudes for the individual transmitted and reflected waves are shown in the following tables:

Table 4-4: Electric Field Amplitudes for Individual Transmitted Waves [33]

Emerging Transmitted Beam	Amplitude of Emerging Transmitted Beam
T_1	$E_0\, t_1\, t_2\, e^{i\omega t}$
T_2	$E_0\, t_1\, t_2\, r_2^2 e^{i(\omega t - \delta)}$
T_3	$E_0\, t_1\, t_2\, r_2^4 e^{i(\omega t - 2\delta)}$

Table 4-5: Electric Field Amplitudes for Individual Reflected Waves [33]

Emerging Reflected Beam	Amplitude of Emerging Reflected Beam
R_1	$E_0\, \mathrm{r}_1\, e^{i\omega t}$
R_2	$E_0\, t_1\, t_2\, r_2 e^{i(\omega t - \delta)}$
R_3	$E_0\, t_1^2 r_2^3 e^{i(\omega t - 2\delta)}$

In both of the above tables, E_0 is the amplitude of the incident electric field. From the exponential, it is shown that the electric field is time dependant, and δ is the phase difference between successively transmitted and reflected beams.

By making the following substitutions the analysis is simplified:

$$t_1 t_2 = \tau \qquad \textbf{(4- 50)}$$

$$R = r_1^2 = r_2^2 \qquad \textbf{(4- 51)}$$

$$\theta = \delta + 2x \qquad \textbf{(4- 52)}$$

Where x represents the phase changes upon reflection of each surface [34]. Summing the individual amplitudes of the transmitted waves; the total amplitude for the transmitted electromagnetic field is (acronym EAT: Electromagnetic field Amplitude Transmitted) [34]:

$$EAT_{Total} = \left[\left(1 - e^{i(\omega t - \delta)}(R + \tau)\right) R^{1/2}\right]\left(1 - Re^{i(\omega t - \delta)}\right)^{-1} \quad \textbf{(4- 53)}$$

Summing the individual amplitudes of the reflected waves; the total amplitude for the transmitted electromagnetic field is (acronym EAR: Electromagnetic field Amplitude Reflected) [34]:

$$EAR_{Total} = \tau\left(1 - Re^{i(\omega t - \delta)}\right)^{-1} \quad \textbf{(4- 54)}$$

The intensity of the transmitted and reflected electric fields are given by the product of the total electric field amplitudes and their complex conjugates [34]:

$$I_{Transmitted} = EAT_{Total}\, EAT^{*}_{Total} \quad \textbf{(4- 55)}$$

$$I_{Transmitted} = [1 - 2(R + \tau)\ cos\,\theta + (R + \tau)^2](1 + R^2 - 2R\cos\theta)^{-1} \quad \textbf{(4- 56)}$$

and:

$$I_{Reflected} = EAR_{Total}\, EAR^{*}_{Total} \quad \textbf{(4- 57)}$$

$$I_{Reflected} = \tau^2(1 + R^2 - 2R\ \cos\theta)^{-1} \quad \textbf{(4- 58)}$$

As the beams are parallel to each other, it is possible to use a lens to combine them and observe the interference pattern. Because of the circular symmetry of the device, the transmitted and reflected beams intensity distribution appear as concentric rings. In the case of the transmitted beam, bright rings appear on a dark background. In the case of the reflected beam, dark fringes occur on a bright background, as shown in Figure 4-16.

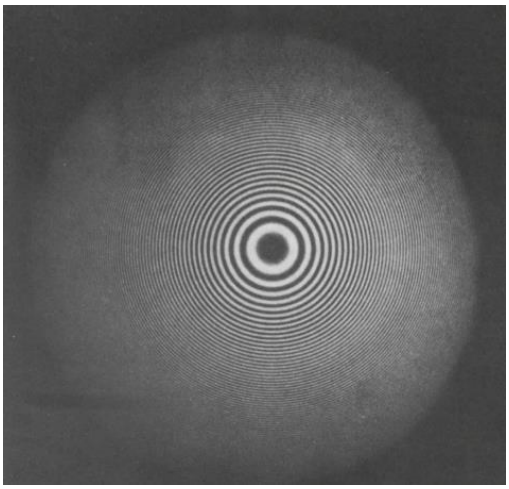

Figure 4-16: Transmitted Radiation from a Fabry Pérot Cavity [34]

The following states there are no energy losses in an ideal interferometer [33]:

$$t_1 t_2 + r_1 r_2 = 1 \qquad \textbf{(4- 59)}$$

The conservation of energy is observed in the reflectance and transmittance, which are defined as the ratio of reflected and transmitted light intensity to the incident light intensity.

CHAPTER 5: EXPERIMENTAL SETUP AND RESULTS

5.1 Introduction

The experimental setup was assembled at the University of Calgary's Mechanical and Manufacturing Engineering Department. Two exploratory experimental setups were created for preliminary evaluation of the proposed leak detection method prior to designing a larger more rigorous setup. A fundamental difference between the in-situ leak detection scheme and the experimental leak detection setup exists. The difference being that the experimental setup is an active approach and the in-situ setup is a passive method. The active approach implies that the energy used to excite the medium is created via a piezoelectric actuator. The passive method implies that the energy is already present in the system due to pipeline vibration.

5.2 Exploratory Experimental Setups

5.2.1 Initial Experimental Setup

Fine grain sand was first baked at 200℃ for several hours to ensure a sample with zero percent water moisture. The sand was placed in a 1.4 L polyethylene container atop an anti-vibration

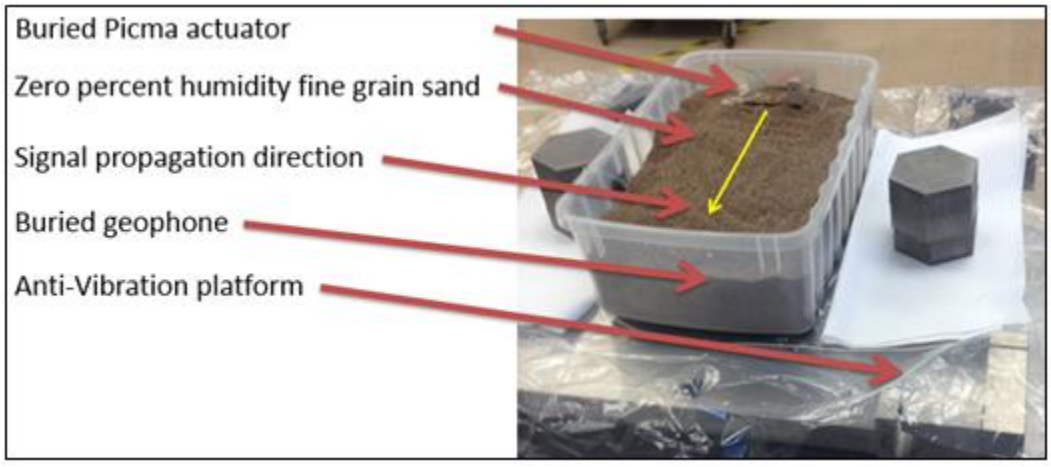

Figure 5-1: Initial Experimental Setup with Picma Actuator

platform (small container assures homogeneity of the sand). Figure 5-1 shows the setup utilizing a miniature multilayer piezo actuator, manufactured by Physik Instrumente (PI) under the trade name "Picma® chip actuator" [35]. The actuator is capable of 2.2µm displacement at 100 Volts, and measures 3x3x2 mm (sensitivity can be found in Table 5-3). The Picma chip was attached to a large mass and fitted with a pressure plate (2.5 mm x 30 mm) via high tack wax on both sides,

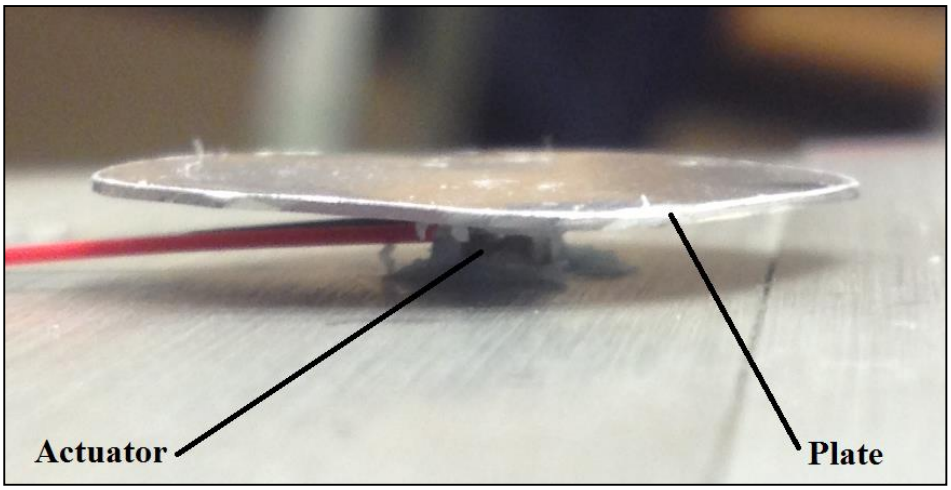

Figure 5-2: Side View of Picma Actuator with the Pressure Plate

as shown in Figure 5-2 above. The Geophone used in the experiment is shown in Figure 5-3, and is manufactured by Geospace Technology, model number GS-32CT. This geophones output is a measure of velocity with a resonance frequency of 10 Hz [36], the sensitivity is shown in Table 5-3.

Figure 5-3: GS-32 CT Geophone

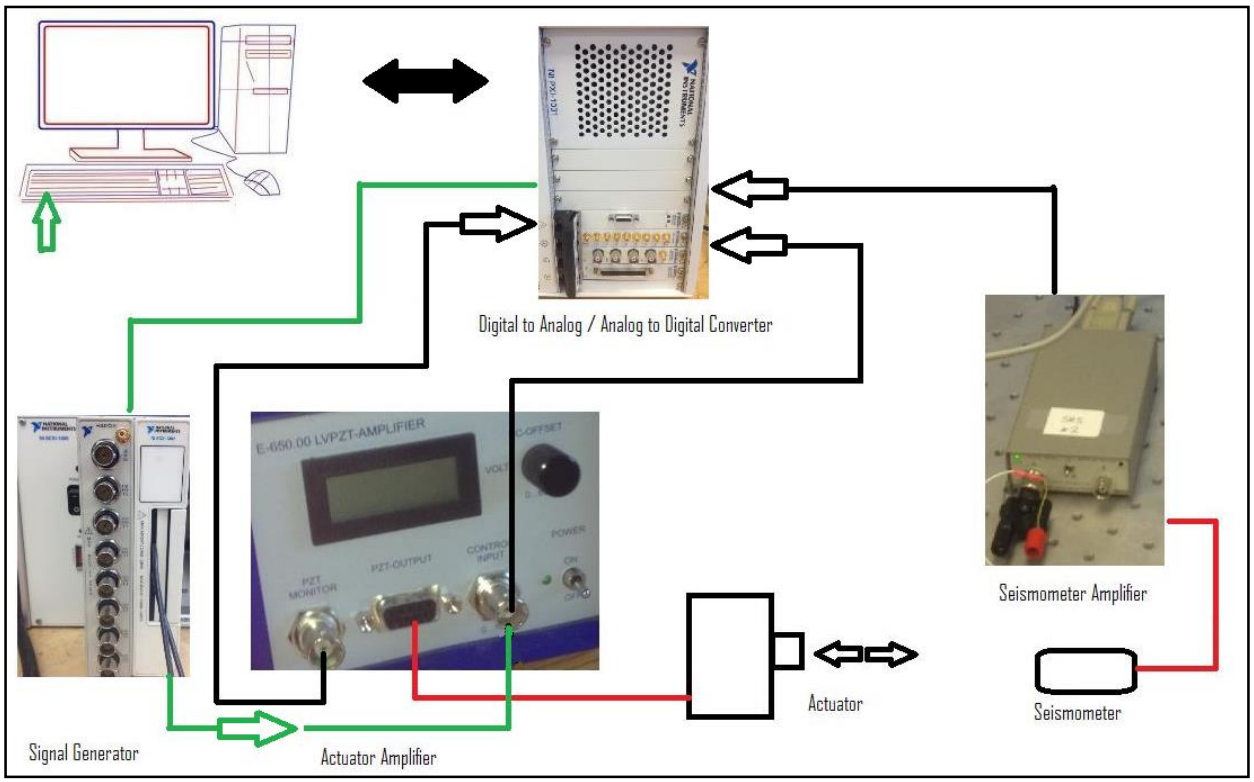

Figure 5-4: Block Diagram for Initial Experimental Setup

The block diagram for the initial experimental setup can be seen in Figure 5-4. A voltage profile was first generated using LabVIEW, either sinusoidal or white noise. This signal was sent to the digital to analog converter, which is essentially an extension of the motherboard of the computer. The signal is then sent to the signal generator, followed by the amplifier used to power the Picma actuator (manufactured by PI, model number E-650.00 LVPZT-AMPLIFIER). The actuator amplifier DC offset can be set by adjusting the potentiometer on the front face. Throughout the initial experimental setup the DC offset was set to 30 Volts. The gain of the amplifier is 6, which means that if 10 Volts are applied to the input, 60 Volts will appear on the output. The signal sent to the actuator varied between ±5 V, which means the actuator was driven from 0 to 60 Volts. This results in a sinusoidal excitation of the Picma actuator with 1.3 µm displacement. The signal is received by the geophone and amplified via the geophone amplifier, which has a

gain of 100 V. Three signals are acquired by the data acquisition device (DAQ). The first channel is physical channel 0, the signal generator. Physical channel 0 is split at the actuator amplifier so that the same signal operating the amplifier is sent directly to the analog to digital converter and recorded. The second signal is physical channel 1, which is the LVPZT-AMPLIFIER monitor, which is one tenth of the driving voltage (output to the actuator) by convention. The third signal is the physical channel 2, which is the GS-32CT Geophone. The physical channels and the digital channels are offset by one, and can be seen in Table 5-1.

Table 5-1: Signal Acquisition Channel Designations for Initial Experimental Setup

Physical Channel	Digital Channel	Component
0	1	Signal Generator
1	2	LVPZT-AMP monitor
2	3	GS-32CT Geophone

5.2.2 Enhanced Experimental Setup (ESS)

The enhanced experimental setup utilized the same geophone, sand and container. The actuator was upgraded to an actuator capable of larger displacement and integrated feedback control (sensitivity can be found in Table 5-3). The larger actuator was also manufactured by Physik Instrumente (PI), model number P845.10, which is a pre-loaded piezo actuator. The advantage to the upgraded actuator is the ability to use feedback to monitor the actual displacement of the actuator, rather than just monitoring the voltage used to drive the actuator (Figure 5-5 shows the assembled actuator). Several sized pressure plates and a large mass were manufactured at the University of Calgary, and assembled to the actuator. Having no prior knowledge of an

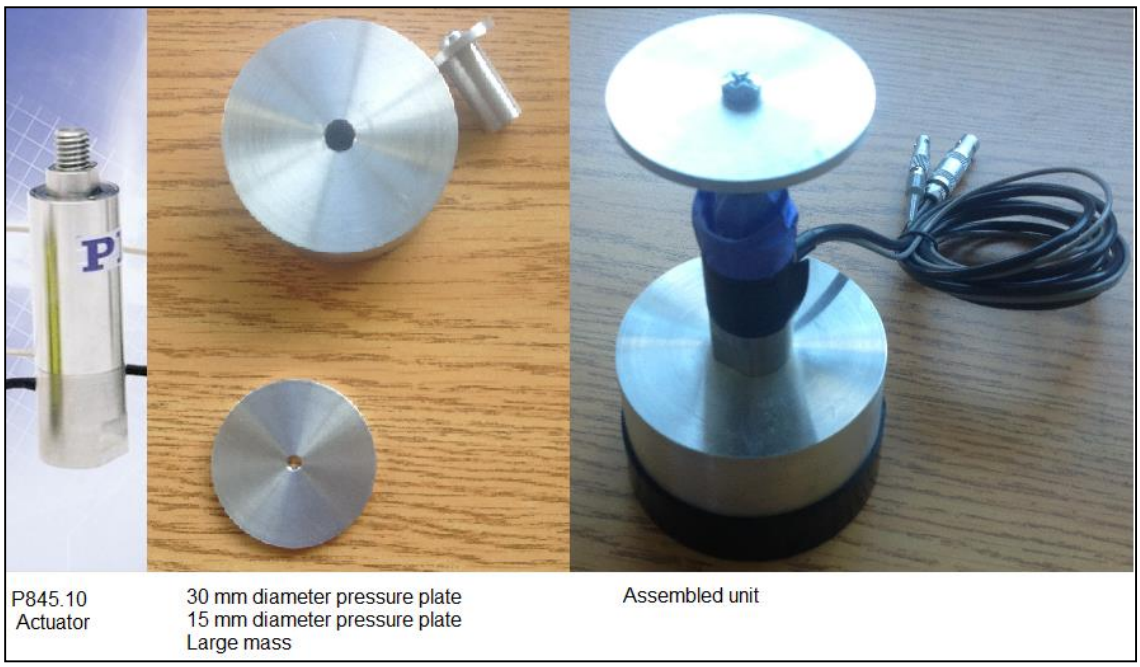

Figure 5-5: P845.10 Actuator Assembly

appropriate pressure plate diameter, the same size pressure plate as that used in the initial experimental setup was used (30 mm). A second pressure plate with an area four times smaller was also chosen (15 mm diameter). The large mass was to act as a stationary object with respect to the inertial frame and would act as a seismic anchor (Figure 5-6 shows the buried actuator and geophone). The block diagram for the enhanced experimental setup can be seen in Figure 5-7. The upgraded actuator required a different amplifier (E-505.00 LVPZT-AMPLIFIER) than the initial experimental setup; capable of sending the feedback signal to the analog to digital converter. A potentiometer is located on the front face to control the DC offset, a ten turn potentiometer in the range of 0 to 100V. "The output voltage is controlled by an analog signal applied to the BNC input ranging from -2 to +12 Volts. Multiplying by the gain factor of 10 (see Table 5-4 Gain of Amplifiers), an output voltage range of -20 to +120 Volts results" [35]. The signal recorded from the actuator monitor is by convention one tenth of the actual output voltage. The physical and digital channel designations can be found in Table 5-2.

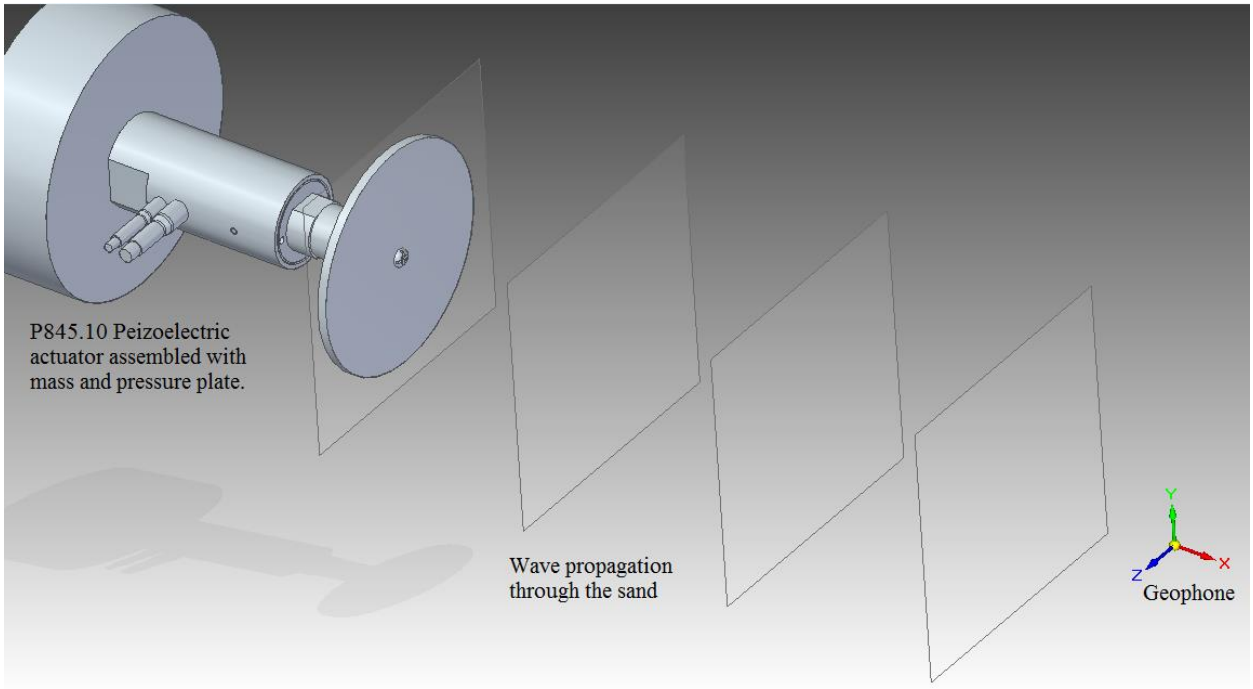

Figure 5-6: Buried P845.10 Actuator and Geophone

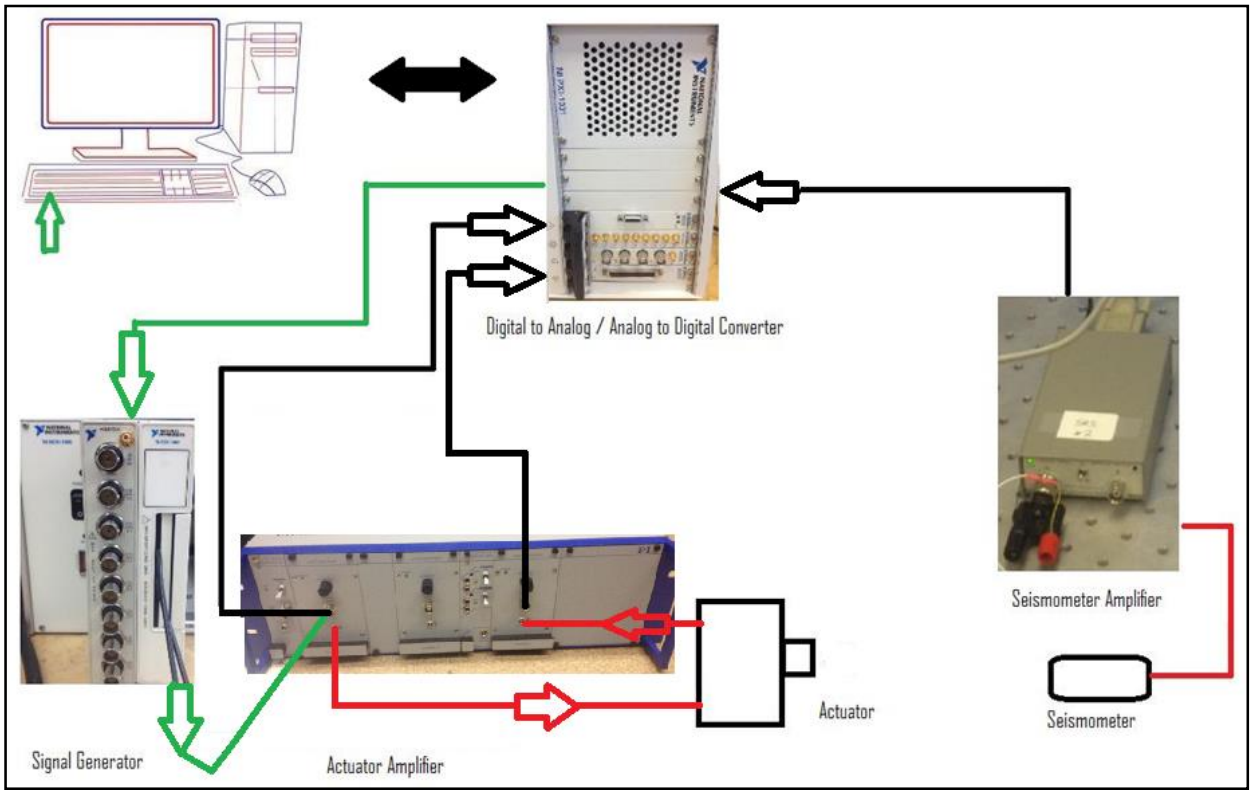

Figure 5-7: Block Diagram for Enhanced Experimental Setup

Table 5-2: Signal Acquisition Channel Designations for Enhanced Experimental Setup

Physical Channel	Digital Channel	Component
0	1	Signal Generator
1	2	GS-32CT Geophone
2	3	P845.10 Actuator monitor

Table 5-3: Sensitivities of Actuators and Geophone

Component	Sensitivity
Picma Chip Actuator	2.2 μm / 100V
P845.10 Pre-Loaded Piezo Actuator	15 μm / 100V
GS-32CT Geophone	27.5 V/m/s

Table 5-4: Gain of Amplifiers

Component	Gain
E-650.00 LVPZT-AMPLIFIER	+6 ±1V
Geophone Amplifier	+100 ±1 V
E-505.00 LVPZT-AMPLIFIER	+10 ±0.1

5.3 Results

5.3.1 Characterizing the Ambient Noise

The objectives of the experimental setups are to provide valid transfer functions capable of producing quantifiable features of the signal channel. The results presented here identify the conditions in which the objectives can be achieved, as well as the values for the natural frequency, damping ratio, gain, and phase shift of the system.

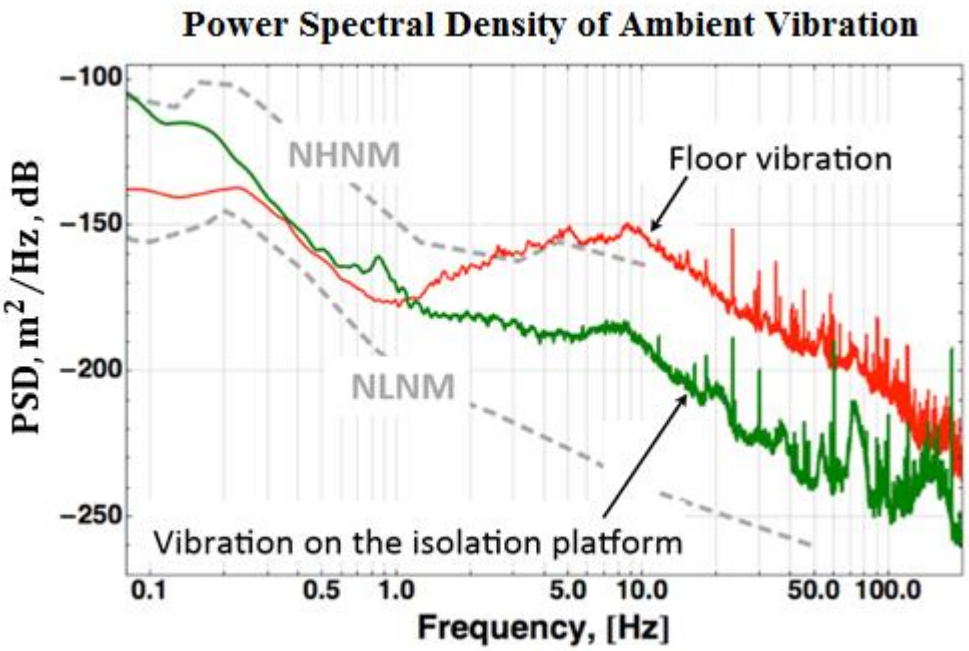

Figure 5-8: Ambient Noise in the University of Calgary Micro Dynamics laboratory

The ambient noise was first measured in the University of Calgary Micro Dynamics laboratory, and was assumed to be constant. This was accomplished by recording the geophone signal with no excitation to the system. The results are shown in Figure 5-8. This figure, shows for reference, the New High Noise Model (NHNM) as well as the New Low Noise Model (NLNM), together with the floor vibration both with and without the isolation platform enabled. When the vibration isolation platform is disabled the floor vibration (ambient noise) is above the NHNM, and is

assumed to be representative of a pipeline close to cities or locations of high background noise. When the vibration isolation platform is enabled the ambient noise is between the NLNM and the NHNM and is assumed to be representative of a pipeline in a remote location.

5.3.2 System Identification with Signals Buried in Noise

To evaluate the usefulness of the three methods used to obtain the transfer function it was necessary to perform the experiment with weak excitation and strong excitation. One of the fundamental questions this research attempts to answer is whether or not a valid transfer function can be obtained if the signal source is "buried in noise". It is possible to compare results for the two scenarios as follows; set the excitation strength to a level that is above the ambient noise and then again below the ambient noise. If the transfer functions are significantly different it may not be possible to produce a valid transfer function from the "buried" signal. Figure 5-9 shows the

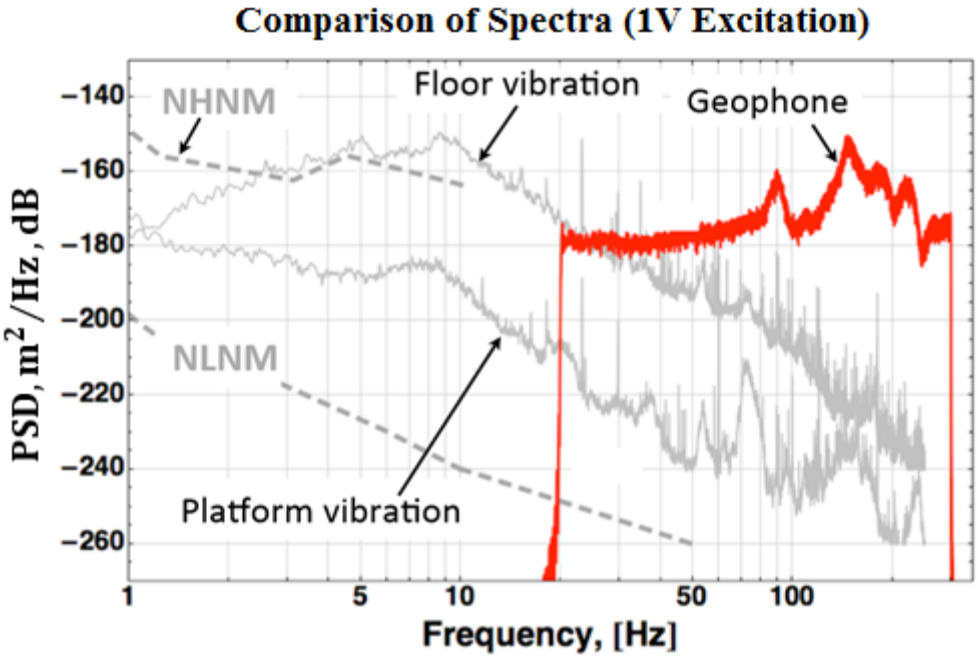

Figure 5-9: Comparison of Spectra for Excitation Amplitude Set to 1.5 µm

geophone signal (converted to displacement) when the excitation amplitude is set to 1.5 µm, and is above both the floor vibration (no vibration isolation) and above the NHNM (exception being at the left side). Figure 5-10 shows the geophone signal (converted to displacement) when the excitation amplitude is set to 0.15 µm, and is effectively "buried" in the ambient noise, and is below the NHNM. The 1.5 µm excitation and 0.15 µm excitation represent the two scenarios used to test if a valid transfer function can be obtained from the proposed experimental setup. In addition, by activating the vibration isolation and setting the excitation amplitude to 0.15 µm, an effective separation between the measured signal and the background noise results. This allows verification of the results obtained from the test with no vibration isolation (set to 0.15 µm), this result is shown for the parametric estimation in Section 5.4.6.

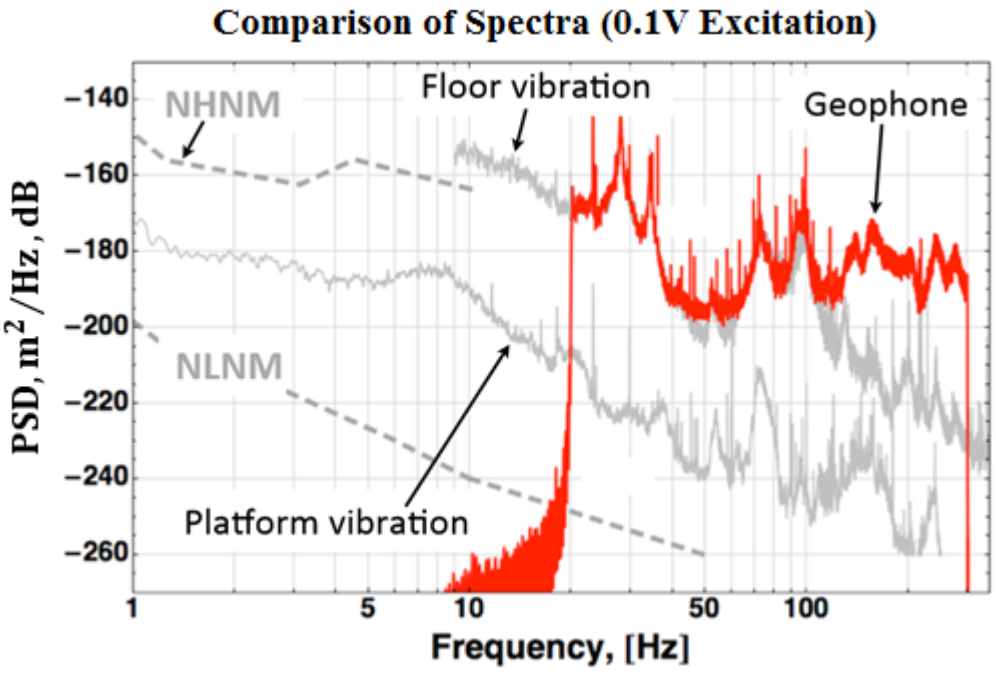

Figure 5-10: Comparison of Spectra for Excitation Amplitude = 0.15 µm

5.3.3 Time Domain Response

One of the first objectives was to determine if the signal from the exciter was retrieved by the geophone. A snapshot of the time domain response to a sinusoidal excitation set to 46 Hz and 1 µm displacement in the initial experimental setup is shown in Figure 5-11 (A), it shows that the geophone signal is recovered in the time domain. A filter was applied to the time domain

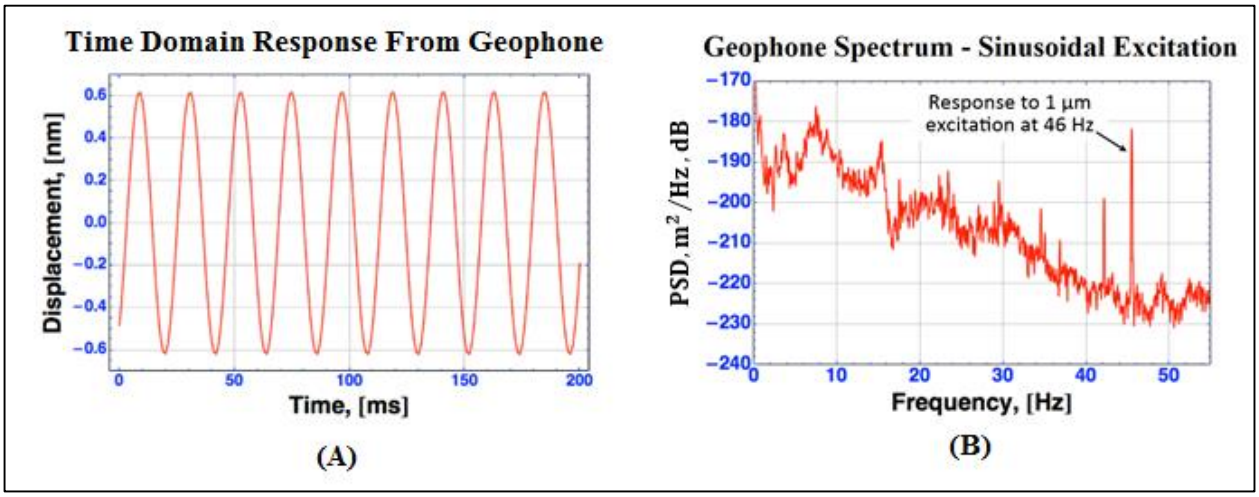

Figure 5-11: Sinusoidal Excitation of the Initial Experimental Setup

(A) Filtered Time Domain Response from Geophone

(B) Geophone Frequency Domain Spectrum

response and a displacement measuring 0.6 nm was recorded. Figure 5-11 (B) shows the frequency domain response of the geophone. Figure 5-12 shows the unfiltered and filtered time domain response from the geophone with the 46 Hz sinusoidal excitation. Clearly the signal is buried in ambient noise. Figure 5-13 shows the time domain signal from the enhanced experimental setup with the excitation amplitude set to 1.5 µm. This test represents the "high level" excitation. Figure 5-14 shows the time domain signal from the enhanced experimental setup with the excitation amplitude set to 0.15 µm. This test represents the "low level" excitation, where the time domain signals show that white noise with a Gaussian distribution was applied to the actuator.

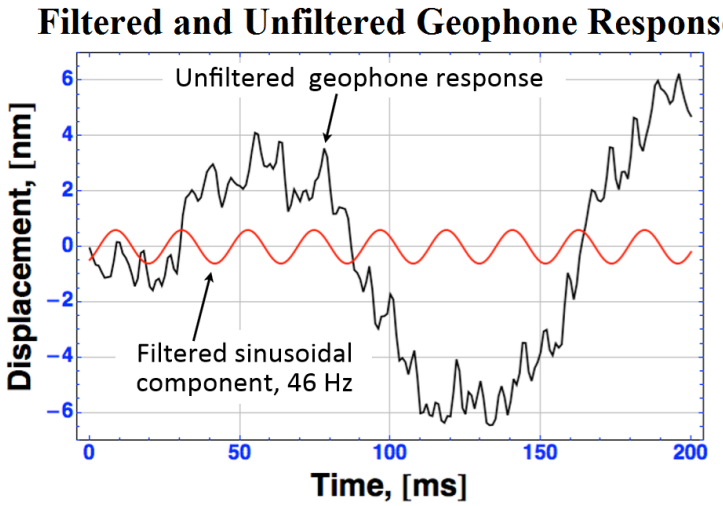

Figure 5-12: Filtered and Unfiltered Time Domain Response from the Geophone with Sinusoidal Excitation for the Initial Experimental Setup

Figure 5-14 (C) shows a maximum displacement of 0.3 µm (ambient noise and excitation signal) measured by the geophone, this is 500x stronger from that shown in Figure 5-11 (A), due to the use of the narrow bandwidth time domain filter in Figure 5-11 (A). The displacement time domain signal of the geophone for the low level excitation appears much different than the high level excitation. This is due to the high level of low frequency ambient noise in the laboratory. The "sinusoidal" appearance of the time domain displacement signal from the low level excitation does not appear in the case of the high level excitation due to the application of a band-pass filter (20 – 300 Hz) in the latter case.

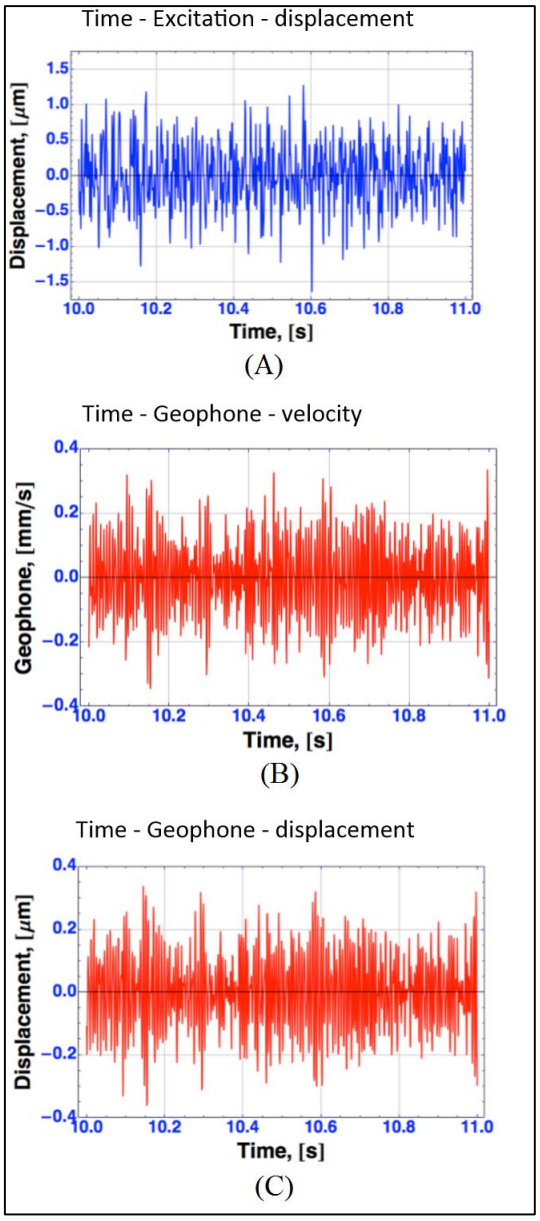

Figure 5-14: Time Domain Response from ESS, Excitation Amplitude = 1.5 µm

(A) Excitation Displacement

(B) Geophone Velocity

(C) Geophone Displacement

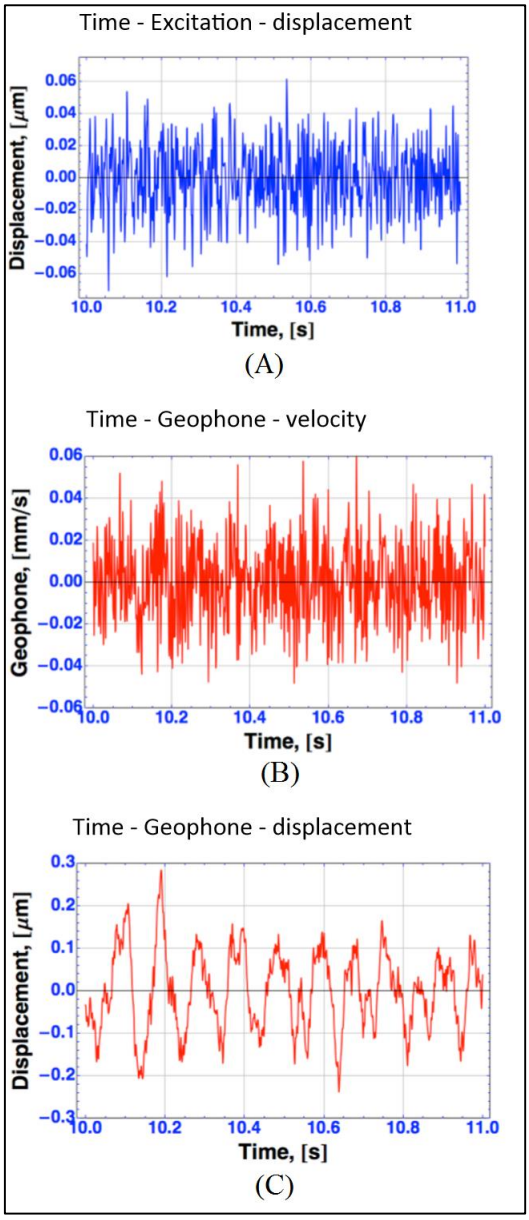

Figure 5-13: Time Domain Response from ESS, Excitation Amplitude = 0.15 µm

(A) Excitation Displacement

(B) Geophone Velocity

(C) Geophone Displacement

5.3.4 Periodogram Estimation

The periodogram method of estimating the transfer function was the first method evaluated. The periodogram estimates of the power spectral density from the time domain signals shown in Section 5.3.3 are displayed in Figures 5-15 and 5-16. The low and high excitation periodogram PSD estimates appear to be the same, as these signals are not contaminated with ambient noise, as shown in Figures 5-15 (A) and 5-16 (A).

A comparison between the low and high excitation periodogram PSD estimates for the geophone displacement reveal that the low excitation periodogram estimate is contaminated severely at low frequency by ambient noise, as shown in Figure 5-16 (C). This contamination carries through and produces an unreliable transfer function. Figure 5-17 shows the transfer functions for the high level of excitation, and low level excitation between the displacement of the geophone and the displacement of the actuator. The periodogram estimate of the high level excitation of the geophone is improved by the use of a zero phase shift bandpass filter (20-300Hz). Since the low frequency noise observed in the lab is cultural noise, it would not be present in a remote pipeline location, and for this reason it was removed. By removing the low frequency noise, the estimate is improved significantly, which can be seen in the transfer function for the high level excitation (Figure 5-18 (A)). Figures 5-18 (A) and 5-18 (B) show the same transfer function provided in Figure 5-17, however Figure 5-18 is focussed on the frequencies between 20 Hz and 100 Hz. Here the transfer functions are obtained by taking the ratio of geophone power spectral density divided by the excitation power spectral density (see Section 4.2.1.2 and Appendix B). What is immediately obvious is that the shape of the transfer functions are not the same between the low

and high excitation; indicating that the low level signal is not capable of producing a valid transfer function due to being immersed in the ambient noise.

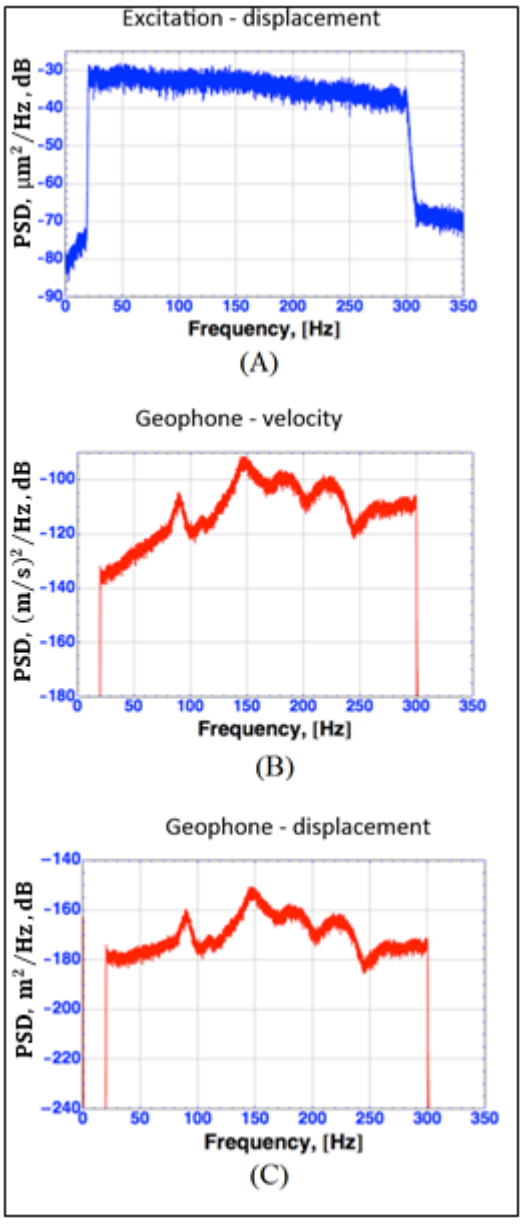

Figure 5-15: Periodogram Response from EES, Excitation Amplitude = 1.5 µm

(A) Excitation Displacement PSD

(B) Geophone Velocity PSD

(C) Geophone Displacement PSD

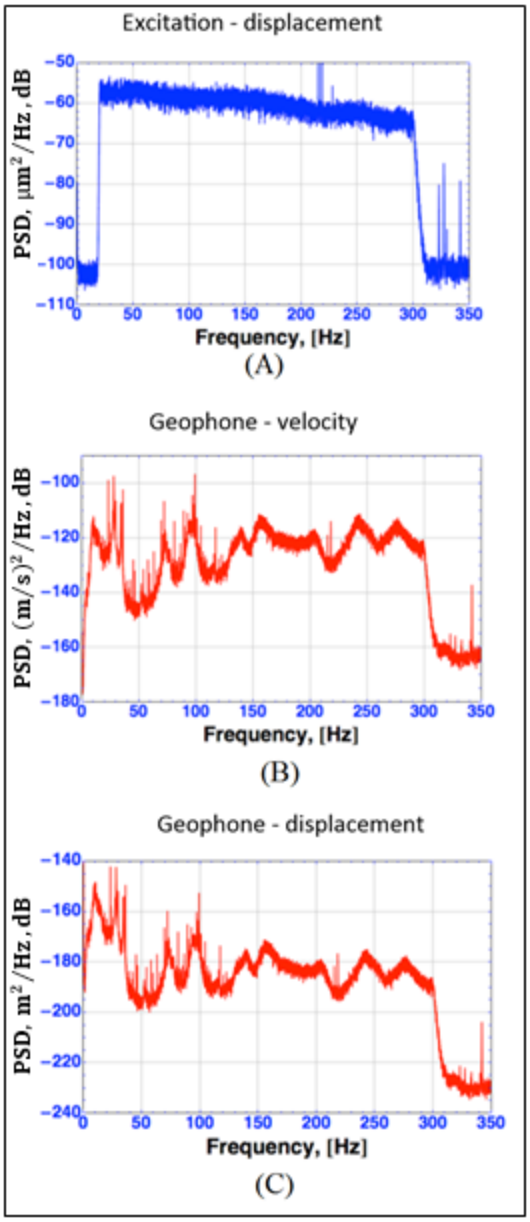

Figure 5-16: Periodogram Response from EES, Excitation Amplitude = 0.15 µm

(A) Excitation Displacement PSD

(B) Geophone Velocity PSD

(C) Geophone Displacement PSD

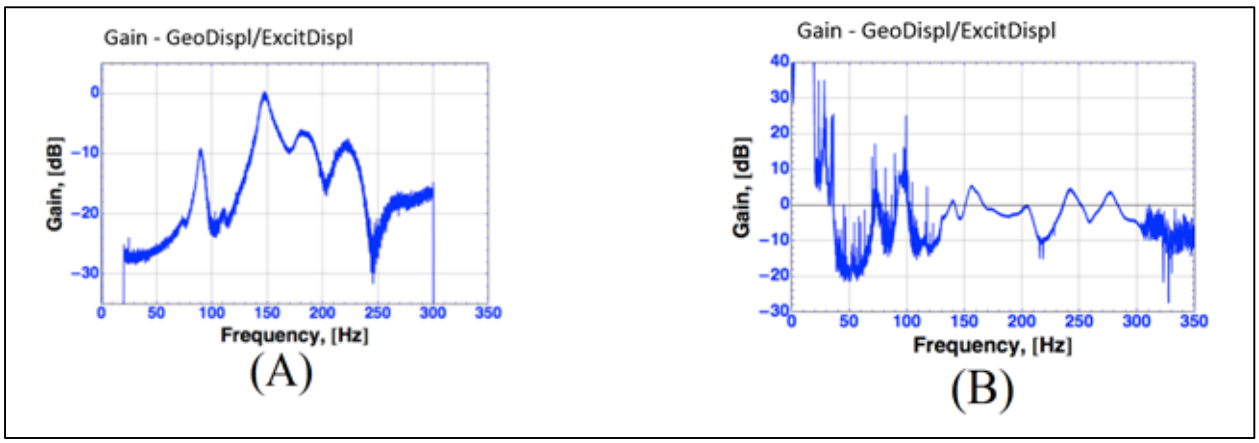

Figure 5-17: Gain of Periodogram Transfer Function from EES

(A) Gain Shown From 0 – 350 Hz, Excitation Amplitude = 1.5 µm

(B) Gain Shown From 0 – 350 Hz, Excitation Amplitude = 0.15 µm

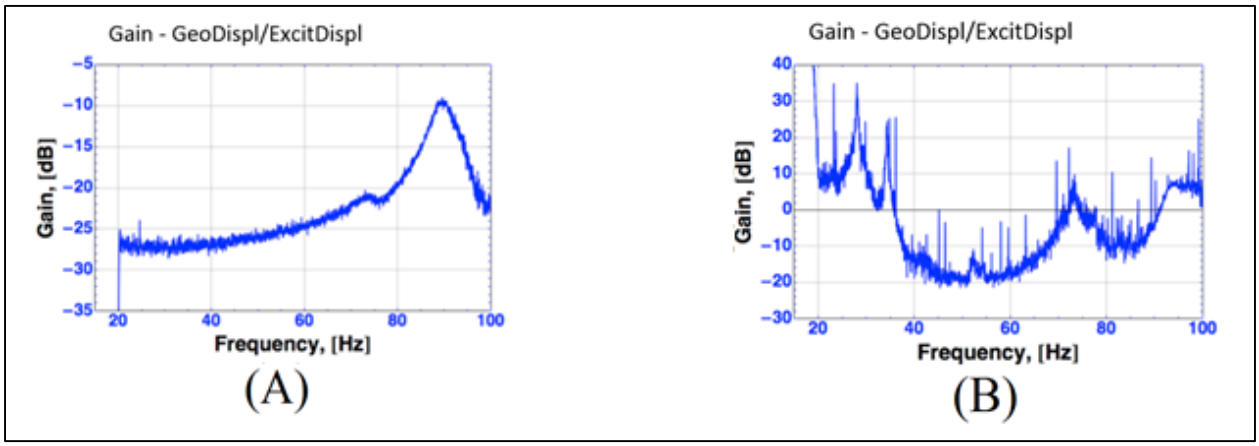

Figure 5-18: Gain of Periodogram Transfer Function from EES

(A) Gain Shown From 20 – 100 Hz, Excitation Amplitude = 1.5 µm

(B) Gain Shown From 20 – 100 Hz, Excitation Amplitude = 0.15 µm

5.3.5 Correlogram Estimation

The correlogram method of estimating the transfer function was the second method evaluated. Here the transfer function is produced by taking the ratio of the absolute values of the cross-correlation divided by the autocorrelation of the excitation (see Section 4.2.1.3 and Appendix C). Figures 5-19 and 5-20 show the autocorrelations and cross-correlations of the time domain signals shown in Section 5.3.3. The high excitation is shown in Figure 5-19 and the low is shown in Figure 5-20, where the lags are shown up to 0.25 seconds. The gain and phase of the transfer functions obtained from the correlogram method of estimating the PSD are shown in Figures 5-21 and 5-22 (high excitation of 1.5 µm). The estimate of gain is considerately improved when compared to the periodogram, due to smaller fluctuations in the PSD. However, the computational effort involved in the correlogram is significantly higher.

The low excitation (0.15 µm) gain of the transfer function obtained from the correlogram method of estimating the PSD is shown in Figure 5-23. The results are only marginally better than the periodogram method, as the low frequency noise has a similar impact on the correlogram. A very poor estimate of the phase shift is produced due to the noise in the signal and the estimate is not presented for this reason.

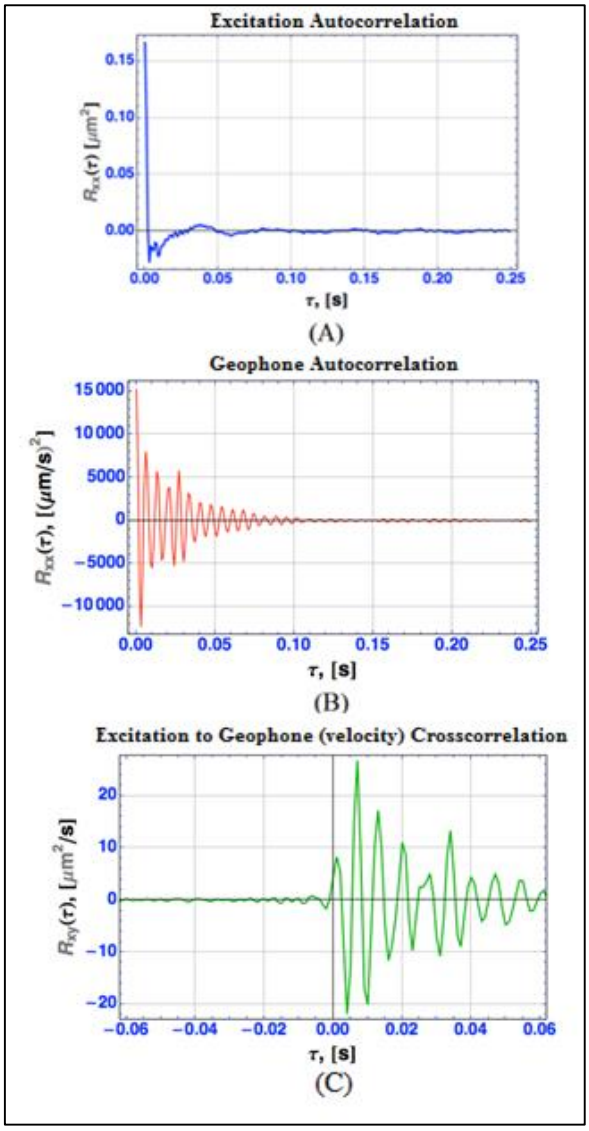

Figure 5-19: Correlation functions from EES, Excitation Amplitude = 1.5 µm

(A) Autocorrelation of Excitation

(B) Autocorrelation of Geophone

(C) Cross-correlation in Velocity

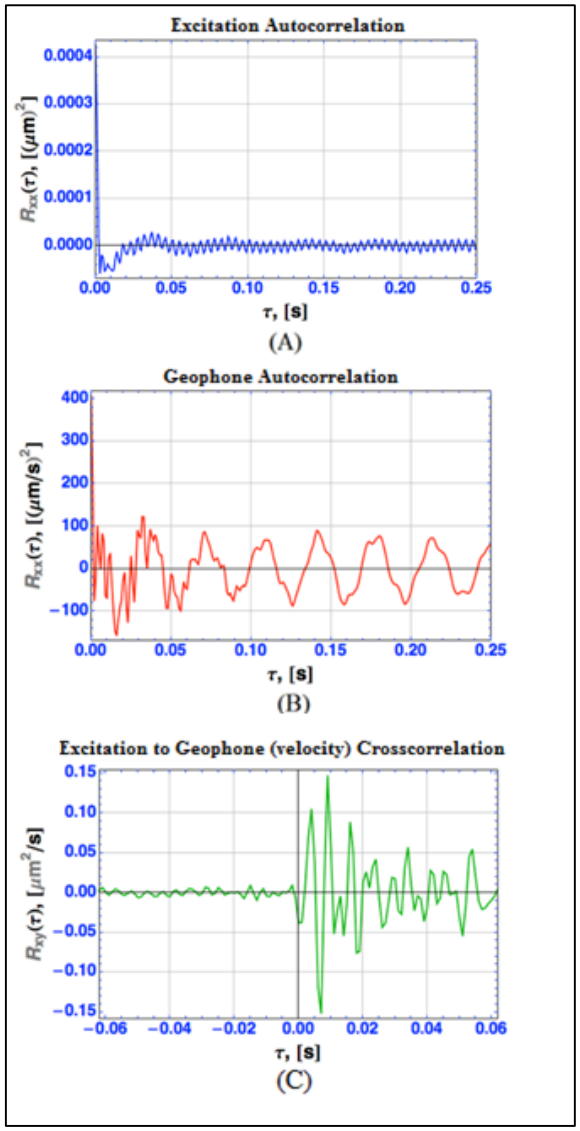

Figure 5-20: Correlation functions from EES, Excitation Amplitude = 0.15 µm

(A) Autocorrelation of Excitation

(B) Autocorrelation of Geophone

(C) Cross-correlation in Velocity

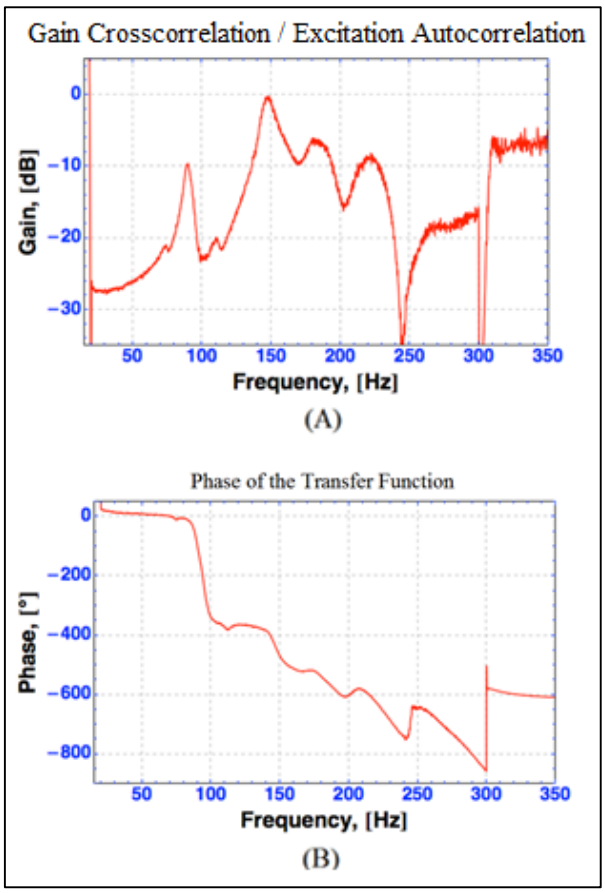

Figure 5-21: Gain and Phase of Correlogram Transfer Function from EES, Excitation Amplitude = 1.5 µm

(A) Gain Shown From 0 – 350 Hz

(B) Phase Shown From 0 – 350 Hz

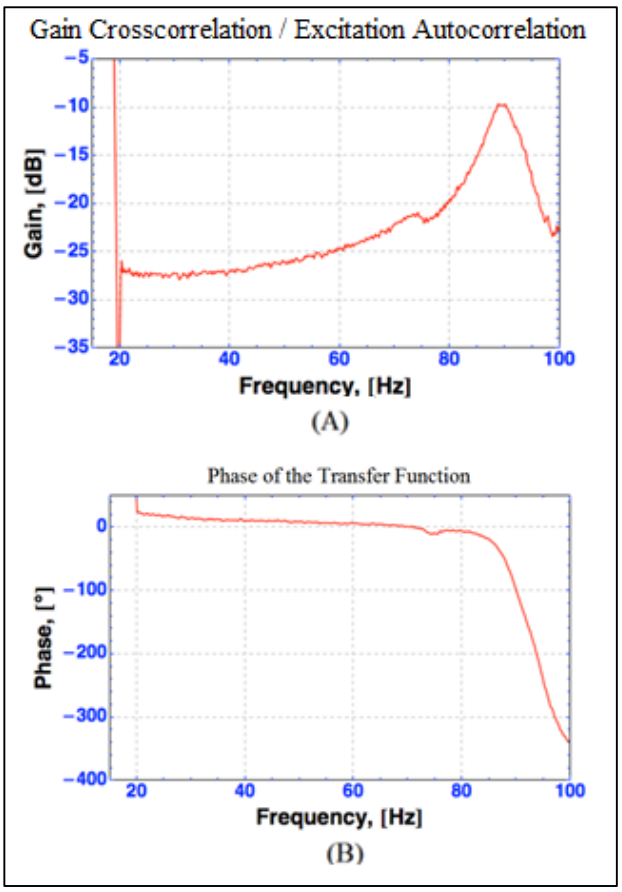

Figure 5-22: Gain and Phase of Correlogram Transfer Function from EES, Excitation Amplitude = 1.5 µm

(A) Gain Shown From 0 – 100 Hz

(B) Phase Shown From 0 – 100 Hz

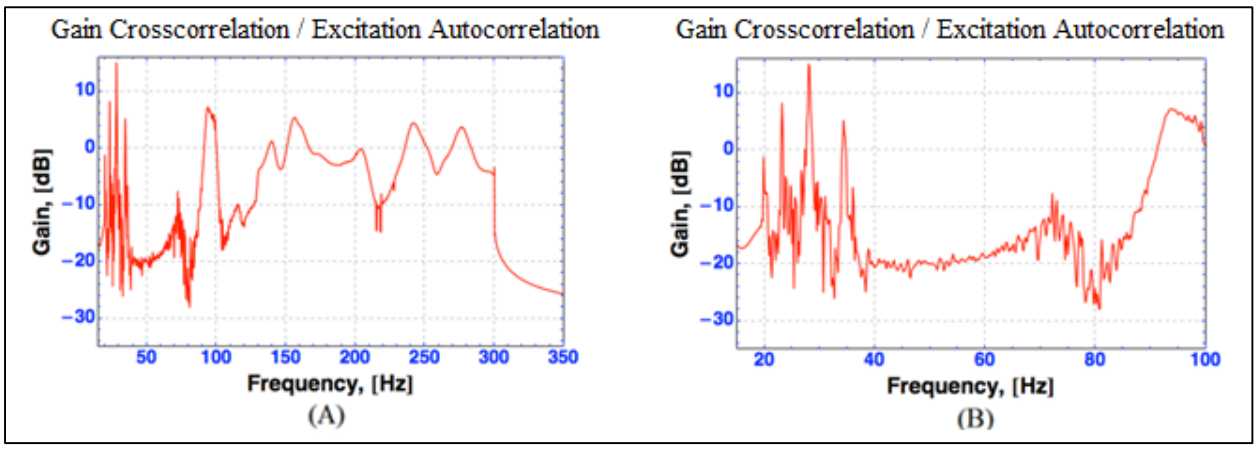

Figure 5-23: Gain of Correlogram Transfer Function from EES, Excitation Amplitude = 0.15 µm

(A) Gain Shown From 0 – 350 Hz

(B) Gain Shown From 0 – 100 Hz

5.3.6 Parametric Estimation

The parametric method of estimating the transfer function was the third method evaluated (see Section 4.2.1.4 and Appendix D). Figures 5-24 and 5-25 show the gain and phase of the parametric estimate of the transfer function from the enhanced experimental setup (amplitude set to 1.5 µm). Figure 5-25 focusses on the frequencies from 0 Hz to 100 Hz, and shows very little noise in the estimate, the quality is comparable to the correlogram method. The quality of the phase shift estimates shown in Figures 5-24 (B) and 5-25 (B) are well defined, and also agree

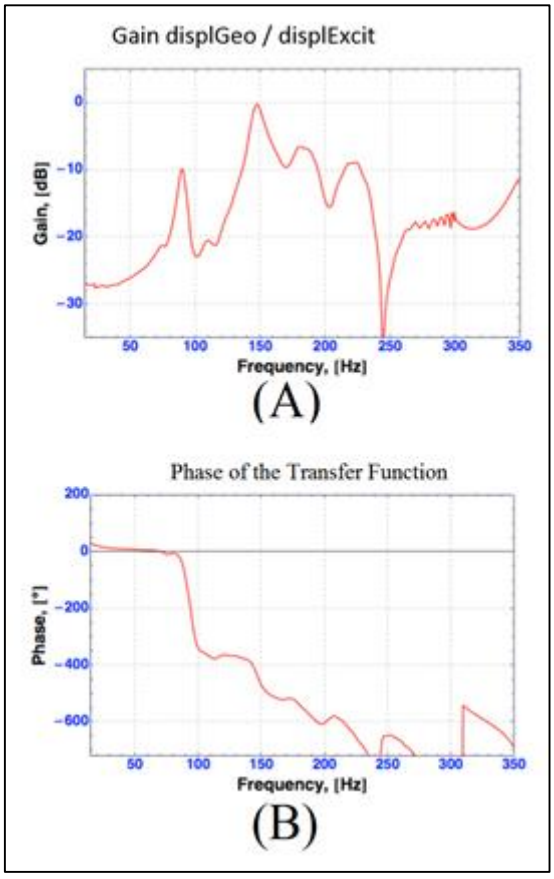

Figure 5-24: Gain and Phase of Parametric Transfer Function from EES, Excitation Amplitude = 1.5 µm

(A) Gain Shown From 0 – 350 Hz

(B) Phase Shown From 0 – 350 Hz

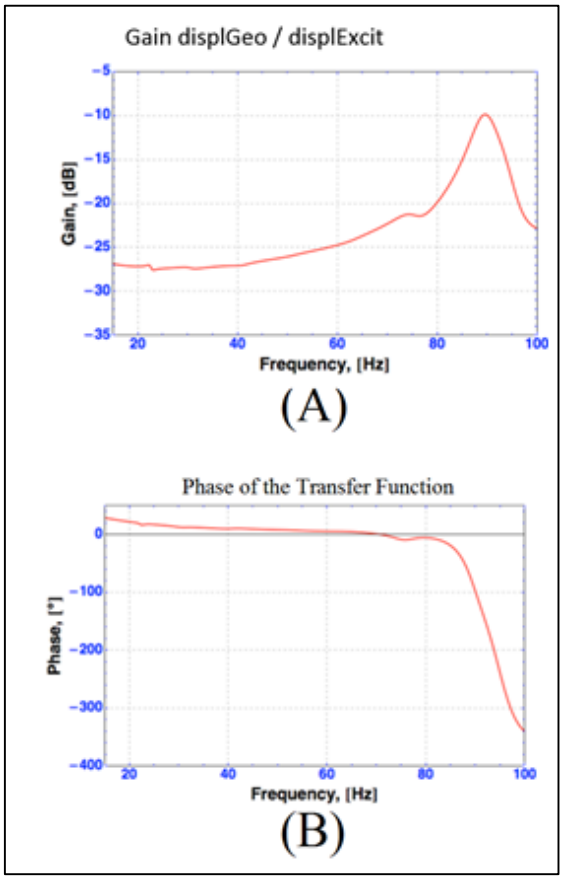

Figure 5-25: Gain and Phase of Parametric Transfer Function from EES, Excitation Amplitude = 1.5 µm

(A) Gain Shown From 0 – 100 Hz

(B) Phase Shown From 0 – 100 Hz

well with the correlogram estimates. The gain and phase from the low excitation are shown in Figures 5-26 and 5-27, and, again, are very unreliable.

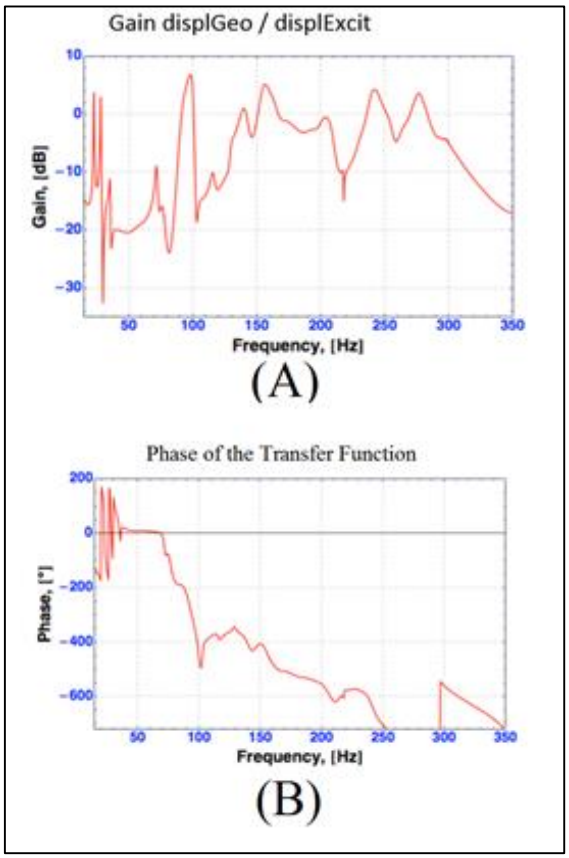

Figure 5-26: Gain and Phase of Parametric Transfer Function from EES, Excitation Amplitude = 0.15 µm

(A) Gain Shown From 0 – 350 Hz

(B) Phase Shown From 0 –350 Hz

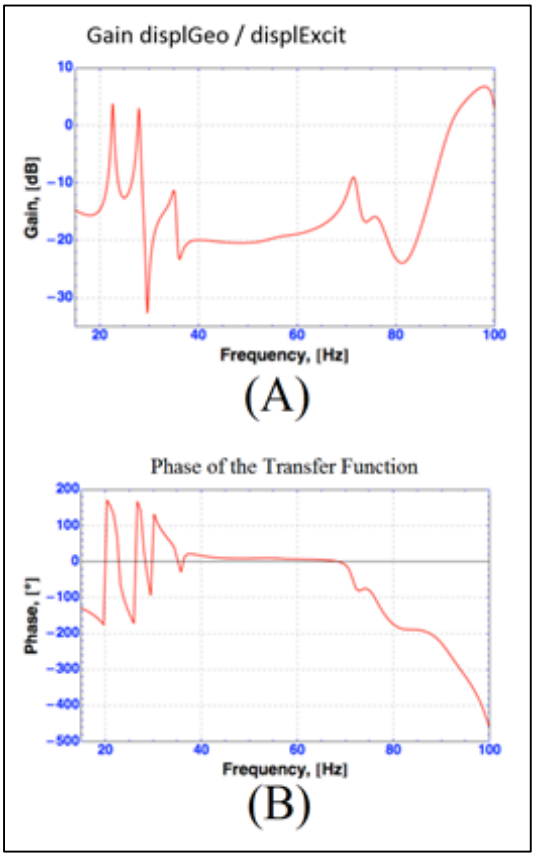

Figure 5-27: Gain and Phase of Parametric Transfer Function from EES, Excitation Amplitude = 0.15 µm

(A) Gain Shown From 0 – 100 Hz

(B) Phase Shown From 0 – 100 Hz

To confirm that ambient noise is the problem with the low excitation results another test is performed. The anti-vibration platform is enabled and the system is again excited by the actuator with 0.15µm amplitude. This scenario puts the response from the geophone above the strongly attenuated ambient noise. Figure 5-28 shows the gain of the transfer function with the anti-vibration platform enabled, and the results confirm that the ambient noise is indeed the culprit for

producing the poor results. The gain of the transfer function shown in Figure 5-28 is comparable to the gain of the high level excitation for the parametric estimation. The major difference between the two is that there are two resonance peaks in Figure 5-28, at approximately 90 Hz, instead of one.

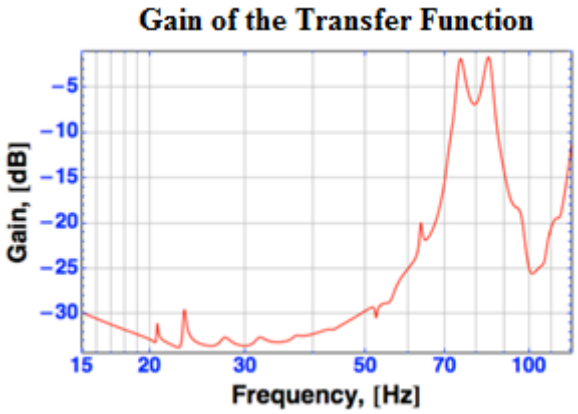

Figure 5-28: Gain of the Parametric Transfer Function from EES, Excitation Amplitude = 0.15 µm with Anti-vibration platform enabled.

5.3.7 Comparison and Selection of Recommended Method

The following Figures overlay the periodogram and correlogram transfer function estimates with the parametric estimate. Figure 5-29 (A) shows the periodogram gain comparison, and Figure 5-29 (B) shows the correlogram comparison. It is evident that the correlogram and parametric

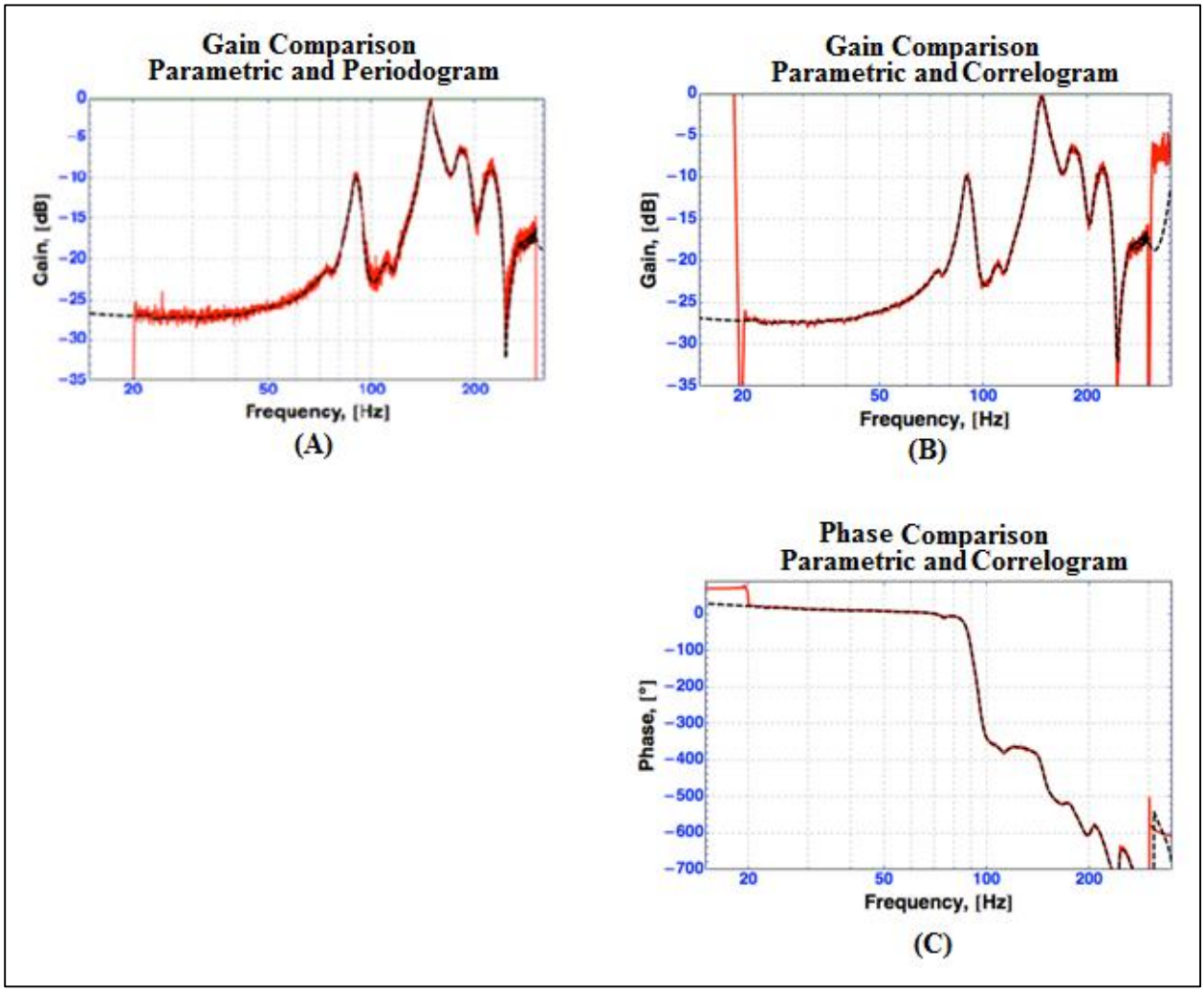

Figure 5-29: Comparison between Transfer Functions and Phase Estimates from EES, Excitation Amplitude = 1.5 µm :

(A) Gain; Black Dashed Line – Parametric Estimate, Dark Red Line – Periodogram Estimate

(B) Gain; Black Dashed Line – Parametric Estimate, Dark Red Line – Correlogram Estimate

(C) Phase; Black Dashed Line – Parametric Estimate, Dark Red Line – Correlogram Estimate

methods are better than the periodogram, due to less noise and the availability of the phase estimate. Although there is less noise in the gain Bode plot produced from the correlogram, it takes considerably longer to complete the correlation function than the parametric estimation takes to estimate the transfer function. Figure 5-30 shows the overlay of the correlogram with the parametric estimate in the frequency range of 15 Hz to 100 Hz, and shows clearly that the two estimates are very similar.

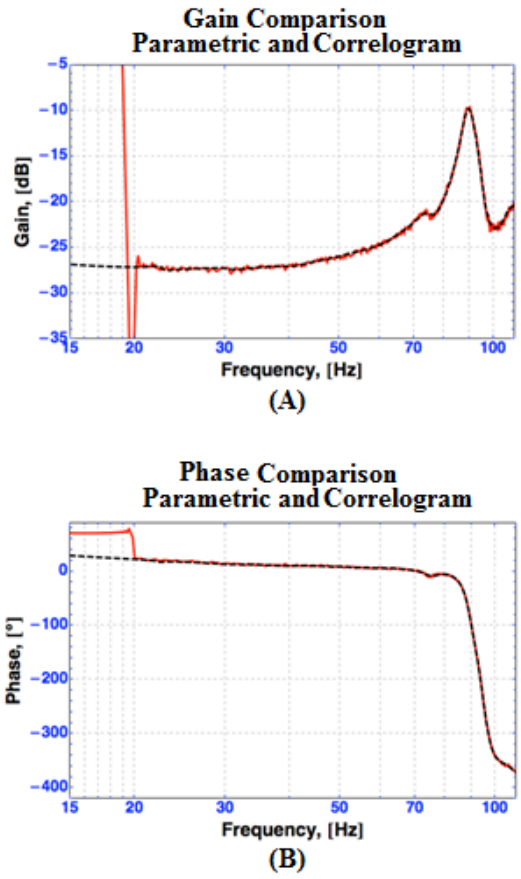

Figure 5-30: Comparison between Transfer Functions and Phase Estimates from EES, Excitation Amplitude = 1.5 µm :

(A) Gain; Black Dashed Line – Parametric Estimate, Dark Red Line – Correlogram Estimate

(B) Phase; Black Dashed Line – Parametric Estimate, Dark Red Line – Correlogram Estimate

Because the parametric method obtains the parameters of the system (coefficients), it facilitates unambiguous computation of the features. The recommended method is therefore the parametric method.

5.3.8 Numerical Results from Recommended Method

The parametric method of estimating the transfer function was selected for several reasons, one major reason being that the features of the signal channel can be quantified unambiguously from the obtained parameters of the system. A powerful tool used in this research is colloquially known as "pruning" the transfer function. Because the order of the transfer function is selected prior to computation, it is difficult to tell what order is required to achieve an adequate estimate until completion. This order is set much higher than the actual order of the system, which is not known, and then reduced through "Pruning". Once the parametric estimation is complete, the poles and zeros are displayed in the z-domain (discrete time) on the unit circle, as described in Chapter 3. Figures 5-31 and 5-32 show the poles and zeros obtained from the parametric estimate of the transfer function for the low and high excitation respectively. The figures first show the transfer function obtained for an 80^{th} order transfer function. Because the parametric method computes the transfer function quickly, it is advantageous to start with a high order transfer function and then prune it to a reasonable order which captures the required information. The figures then show all of the poles and zeros for the estimate, then show a selected amount of poles and zeros ranging from 0-110 Hz. The poles and zeros that are within 5% difference are then cancelled, and effectively prune the transfer function. The last figure shown is the overlay of the pruned transfer function and the unpruned. Table 5-5 summarizes the damping ratios and natural frequencies obtained from the two tests.

Table 5-5: Damping Ratios and Natural Frequencies Obtained from the Parametric Method of Estimating the Transfer Function, Excitations = 0.15 µm (Anti-vibration enabled) and 1.5 µm (Anti-vibration disabled)

Test Type	Natural Frequency / Frequencies	Damping Ratio(s)
EES, Excitation = 0.15 µm, Anti-vibration enabled	74.53 Hz 84.46 Hz	0.0192 0.0200
EES, Excitation = 1.5 µm, Anti-vibration Disabled	89.54 Hz	0.0329

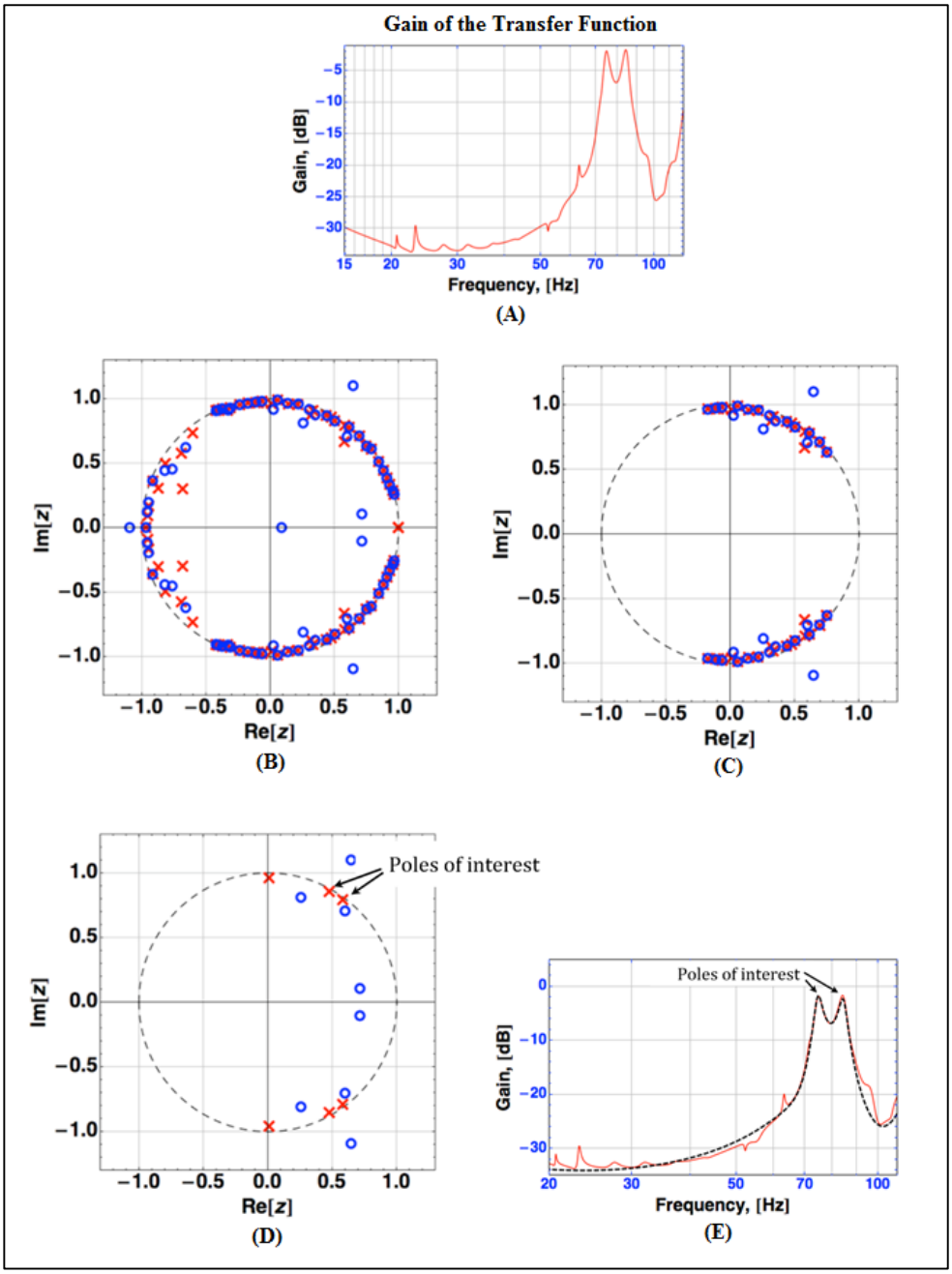

Figure 5-31: Pole-zero Plots of Parametric Estimation from EES, Excitation = 0.15 µm, Anti-vibration Platform Enabled

(A) Gain of the Parametric Transfer Function from 15 to 120 Hz

(B) Pole-zero Plot of the Transfer Function Showing 79 Zeros and 80 Poles

(C) Pole-zero Plot of the Transfer Function from 0 to 110 Hz

(D) Pole-zero Plot of the Transfer Function after Pruning

(E) Approximation (dashed line) of the Transfer Function via Pruned Pole-zero Plot

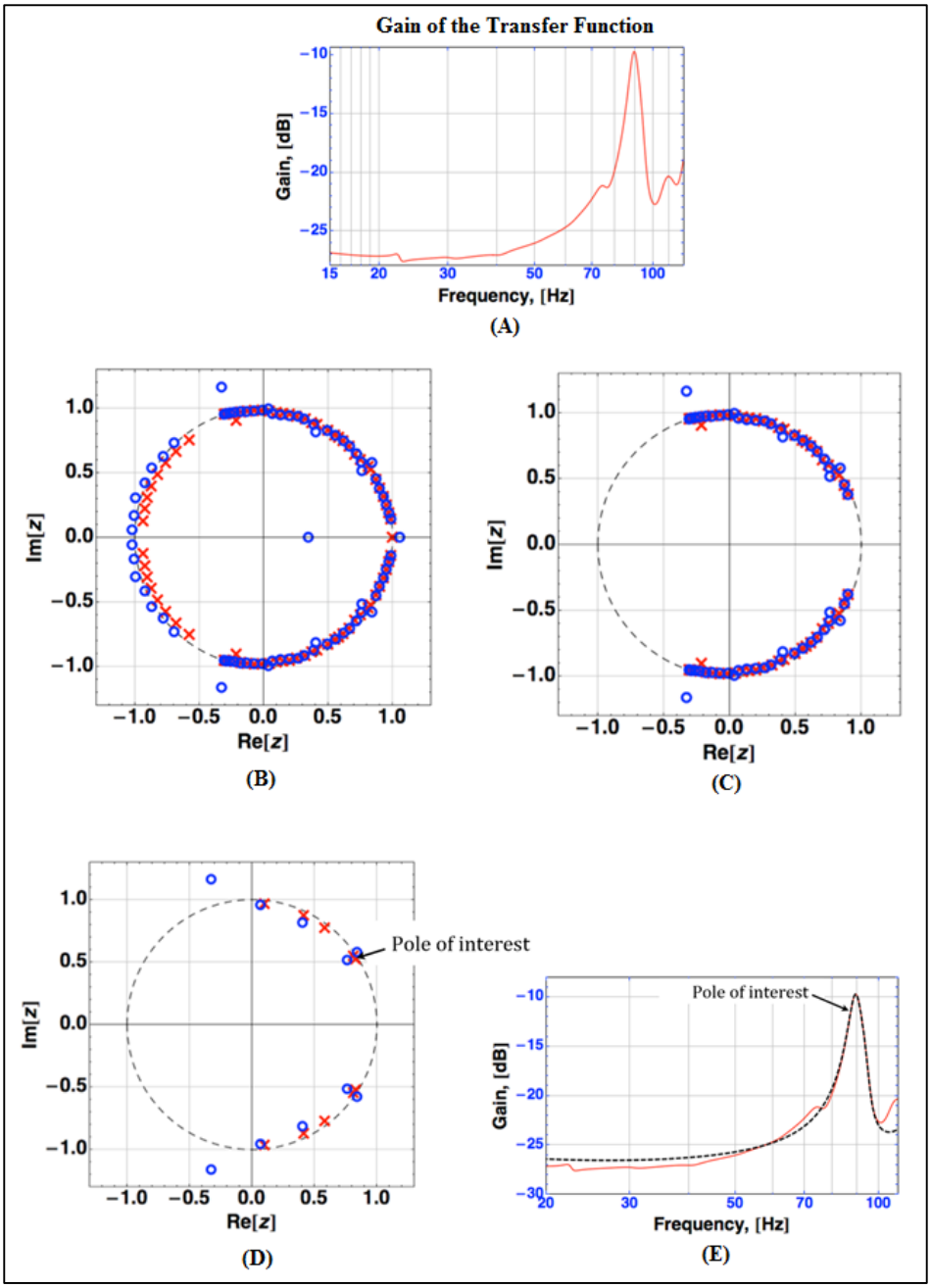

Figure 5-32: Pole-zero Plots of Parametric Estimation from EES, Excitation = 1.5 µm, Anti-vibration Platform Disabled

(A) Gain of the Parametric Transfer Function from 15 to 120 Hz

(B) Pole-zero Plot of the Transfer Function Showing 79 Zeros and 80 Poles

(C) Pole-zero Plot of the Transfer Function from 0 to 110 Hz

(D) Pole-zero Plot of the Transfer Function after Pruning

(E) Approximation (dashed line) of the Transfer Function via Pruned Pole-zero Plot

CHAPTER 6: CONCLUSION AND RECOMMENDATIONS

Pipeline leaks have a high risk, and for this reason have been given a large amount of media and corporate attention as of late. The world is realizing that pipeline leaks are detrimental to both the environment and the economy, and also realizing that the industries current best practices are only meeting the minimum requirements in terms of condition monitoring. Many leak detection schemes are available today, however, none of which are suitable for all situations. Because of this, there will always be a need for new leak detection methods.

The research presented in this thesis describes an experimental setup and numerical evaluation techniques which identify features of the signal channel for pipeline leak detection. The features obtained are expected to be capable of indicating hydrocarbon contamination. The features of interest considered in this research are the gain and phase of the transfer function, the natural frequencies and damping ratios of the signal channel.

One major driving factor for investigating the proposed method of leak detection is the recent advancements in MEMS seismometers. In the past the most widely used sensing techniques in seismometers and accelerometers were capacitive and piezoelectric, which are inferior compared to the new sensing techniques available in emerging MEMS devices. Optical diffraction gratings and Fabry Pérot resonant optical cavities are the optical sensing schemes used in emerging devices, and are therefore the recommended sensors for this type of leak detection. Optical sensing techniques are advantageous because optical performance approaches the Brownian noise limits of the mechanical device, which is often the limiting factor in the sensitivity of the device. The emerging sensors have very low frequency requirements, which allow low frequency

signals from pipelines to be studied, this is an area of pipeline research only recently observable, and is investigated for this reason. Figure 6-1 shows one of the recommended sensors.

Figure 6-1: Silicon Audio's GeoLight Prototype [28]

The method of pipeline leak detection considered in this research is based on the fundamental aspect that pipelines vibrate. Several mechanisms which can excite pipelines at both high and low frequencies exist. For high frequency excitation, blade pass and vortex shedding are the two major excitation mechanisms. The coupling, and amplification mechanism in place for high frequency excitation is the cross wall natural frequency. The high amplitude, high frequency pulsation excites the pipe wall circumferentially, and may analogously be thought of as "breathing".

Low frequency excitation mechanisms are mechanically induced, pulsation induced, or liquid flow excited. The coupling mechanisms in place for low frequency excitation are piping bends, closed pipe sections, valves, orifices, reducers and changes in pipe diameters. The high amplitude, low frequency pulsations may excite the pipe in the axial direction, similar to a beam bending. Low frequency excitations are capable of producing frequencies as low as 5Hz. This

confirms that very low frequency vibrations are apparent in pipelines, and confirms one of the major driving factors for the investigation in this thesis.

Once the pipeline is excited, ground waves propagate away from the pipeline and radiate a large amount of energy. There are four types of ground waves; two of which are classified as body waves, and two are surface waves. The way a sensor is placed in the ground dictates which ground wave it will measure. Therefore the dynamic properties of the ground obtained from the data will depend on the sensor orientation. This research considered the P-wave in the experimental and in-situ setups, this is recommended because the first sensor must be placed close to the buried pipe, and therefore cannot measure surface waves. The proposed experimental setup also utilizes the P-wave as illustrated in Figure 6-2. The proposed experimental setup is recommended because the design allows multiple positions for the geophones to be placed, and

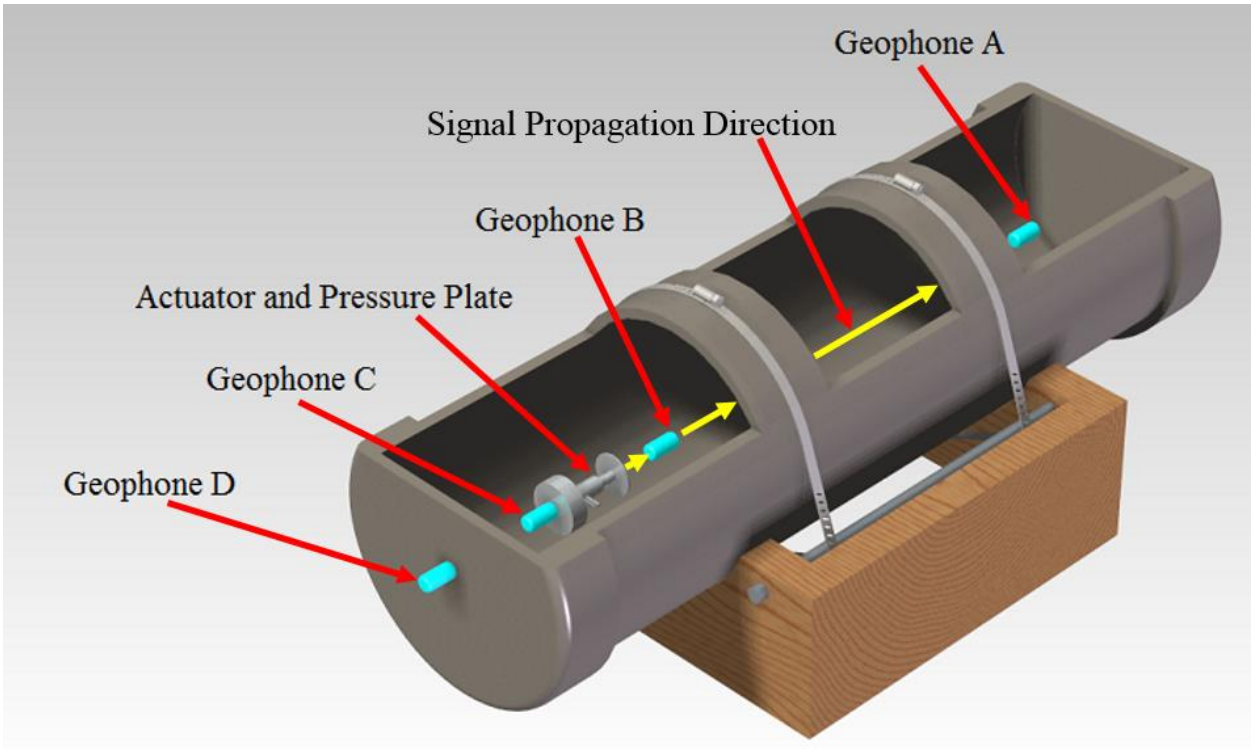

Figure 6-2: Proposed Experimental Setup

allows several extra geophones so correlation between the actuator and the frame is possible. The proposed final setup consists of a much larger container, cut from a 12 inch (304.8 mm) diameter PVC tube, measuring 1 meter (39.37 in) in length. The ends are capped with thick PVC standard caps. The base is constructed from 2" by 8" wood, coped at 45 degrees. The tube is held down securely using hose clamps of sufficient length. The design allows multiple positions for the geophones to be placed as shown in Figure 6-2. Several extra geophones are placed in the setup to allow correlation between the actuator and the frame. Geophone C and Geophone D are placed respectively to the mass attached to the actuator and to the end cap of the tube. The purpose of Geophone C and D are to measure movement with respect to the inertial frame. It is intended that the mass will not move relative to the inertial frame. It is expected that the frame will be of sufficient mass to remain stationary.

Three methods of estimating the transfer function were used in this research. The first method considered was the periodogram, the second the correlogram, and last the parametric method. The periodogram is recommended for preliminary analysis of the data, as it will quickly allow the user to identify erroneous results by observing the individual spectrums created before an average of the spectrums are taken. It is only recommended as a preliminary tool because the phase of the transfer function is not available from this method. The correlogram showed very good results that were almost equal to those obtained from the parametric method. However, the computational effort required to produce the correlation function is extremely high, some calculations took several hours to produce. It was found that the parametric method was the best of the three investigated, and is the recommended method for identifying features of the signal channel. The parametric method produced the cleanest gain Bode plot of the transfer function

(removed noise) and the cleanest Bode phase plot of the three methods. In addition, the computational efforts were not very high, only taking a few minutes to compute. The method of pruning the transfer function discussed in Section 5.4.8 is very helpful, and is recommended in conjunction with the parametric method.

Included in the appendix are several flow charts for obtaining the transfer function from any of the three methods. It is recommended that the charts be followed for the experimental setup, as there is a lot of room for mistakes. For example, in one experiment it was found that the excitation signal created by the signal generator was not exciting the piezo electric actuator for the entire recording. This discontinuity of data acquisition has a very prominent effect on the sensitivity of the FFT. Extreme care must be taken to ensure that the instrumentation settings and data are correct.

From the results Section 5.4.8 it was found that the damping ratios and natural frequencies for the low and high excitation tests were similar and are shown below in Table 6-1. The phenomenon here is that the low excitation showed two natural frequencies where the high excitation only showed one. The reason for this could be wave interference within the sand container via waves reflecting off the back wall, further investigation with a larger setup may shed light on this issue. The percent difference between the high excitation natural frequency and both the higher and lower of the two natural frequencies from the low excitation test are respectively 5.6% and 16.8%. The damping ratios from the two tests are not similar, the percent difference between the high excitation damping ratio and both the higher and lower of the two damping ratios from the low excitation test are respectively 39.2% and 41.6%. This makes sense

however because the shape of the two resonance peaks are similar except the low excitation has two resonance peaks, it is undetermined which test represents the true state of the system.

Table 6-1: Damping Ratios and Natural Frequencies Obtained from the Parametric Method of Estimating the Transfer Function, Excitations = 0.15 µm (Anti-vibration enabled) and 1.5 µm (Anti-vibration disabled)

Test Type	Natural Frequency / Frequencies	Damping Ratio(s)
EES, Excitation = 0.15 µm, Anti-vibration enabled	74.53 Hz 84.46 Hz	0.0192 0.0200
EES, Excitation = 1.5 µm, Anti-vibration Disabled	89.54 Hz	0.0329

CHAPTER 7: FUTURE WORK

The next logical step in this research is to build the proposed experimental setup, and test a variety of different hydrocarbons. Testing the hydrocarbons would encompass the use of the parametric method of estimating the transfer function to identify features of the signal channel. It would then include comparison of the signal channel features between the non-contaminated and contaminated states.

The step after the proposed experimental setup would be the in-situ setup; in collaboration with a pipeline company. The in-situ setup would be a two stage process, the first stage would mimic the experimental setup. Before placing an array of sensors down the length of the pipe, it would make sense to first place a single set, giving only consideration to the radial dimension of the pipeline. The second stage would give consideration to the longitudinal dimension of the pipeline.

The parametric method employed in this research requires the entire data block prior to computing the transfer function. In certain situations it may be advantageous to identify features of the signal channel in real time. A more advanced method of parametric estimation involving a recursive algorithm allows real time updates to the transfer function. Both of these methods of parametric estimation can be enhanced to incorporate the delay of the system which is inherent due to the time it takes for the wave to propagate through the signal channel.

Modelling the entire experimental setup and completing a finite element analysis would be beneficial because it would allow a comparison between the two. Not only would it be

interesting to compare the results, it would provide valuable information about the resonance frequencies obtained from the experimental setup.

REFERENCES

[1] Saskatchewan Association for Resource Recovery Corp., "SARRC Annual Report," Saskatchewan Association for Resource Recovery Corp., Saskatoon, 2009.

[2] Department of Energy and Climate Change, "Potential Greenhouse Gas Emissioins Associated with Shale Gas Extraction and Use," Department of Energy and Climate Change, London, 2013.

[3] T. Chis and A. Saguna, "Pipeline Leak Detection techniques," *The Journal Annals. Computer Science Series,* vol. 5, no. 1, pp. 25-34, 2007.

[4] C. Liu, Foundations of MEMS, Upper Saddle River, NJ: Pearson/Prentice Hall, 2006.

[5] J. R. Hall, F. E. Richart and R. D. Woods, Vibrations of Soils and Foundations, Englewood Cliffs: Prentice-Hall, Inc., 1970.

[6] B. H. Tongue, Principles of Vibration, New York: Oxford University Press, 2002.

[7] A. V. Oppenheim and A. S. Willsky, Signals and Systems, Englewood Cliffs NJ: Prentice Hall, 1997.

[8] C. G. Lai, *Simultaneous Inversion of Rayleigh Phase Velocity and Attenuation for Near-Surface Site Characterization,* Georgia Institute of Technology: Department of Civil and Environmental Engineering, 1998.

[9] S. Foti, G. J. Rix, C. G. Lai and R. Vilantonio, "Simultaneous Measurement and Inversion of Surface Wave Dispersion and Attenuation Curves," in *Soil Dynamics and Earthquake Engineering*, Milano, 2002.

[10] R. B. Caldwell and T. Grant, "A Ground-Motion Transfer Function Matrix between Two Nearby Rock and Soil Sites: A System Identification Problem," *Bulletin of the Seismological Society of America,* vol. 101, no. 1, pp. 222-234, February 2011.

[11] W. T. Chu and O. Hunaidi, "Acoustical characteristics of leak signals in plastic water distribution pipes," *Applied Acoustics,* vol. I, no. 58, pp. 235-254, 1999.

[12] S. Stein and M. Wysession, An Introduction to Seismology, Earthquakes and Earth Structure, St. Louise: Blackwell Publishing, 2003.

[13] J. D. Hoffman, Numerical Methods for Engineers and Scientists, Boca Raton: Taylor & Francis Group, LLC, 2001.

[14] L. S. Marple, Digital Spectral Analysis: With Applications, Englewood Cliffs, NJ: Prentice Hall, 1987.

[15] G. Mavko, "Parameters That Influence Seismic Velocity," Stanford Rock Physics Laboratory, Stanford, 1990.

[16] J. K. Pieper, "ENME 461 Mechatronics," 2004. [Online]. Available: http://homepages.ucalgary.ca/~pieper/Analysis.htm. [Accessed 05 October 2013].

[17] J. Peterson, "Observation and Modeling of Seismic Background Noise," US Department of Interior Geological Survey, Albuquerque, 1993.

[18] S. M. Price and D. R. Smith, "Sources and Remedies of High-Frequency Piping Vibration and Noise," in *Proceedings of the 28th Turbomachinery Symposium*, San Antonio, 1999.

[19] R. D. Blevins, Flow-Induced Vibrations, New York: Van Nostrand Reinhold Ltd., 1977.

[20] M. Mohitpour, K. K. Botros and T. Van Hardeveld, Pipeline Pumping and Compression Systems: A Practical Approach, New York: ASME Press, 2008.

[21] K. E. Atkins, S. J. Morton and J. C. Wachel, "Piping Vibration Analysis," in *Proceedings of the Nineteenth Turbomachinery Symposium*, San Antonio, 1990.

[22] M. Cerna and A. . F. Harvey, "The Fundamentals of FFT-Based Signal Analysis and Measurement," National Instruments, 2000.

[23] J. Bendat and A. G. Piersol, Engineering Applications of Correlation and Spectral Analysis, New York: John Wiley & Sons, Inc, 1980.

[24] R. Isermann, Digital Control Systems, New York: Springer-Verlag, 1981.

[25] J. B. Merchant, "MEMS Applications in Seismology," in *Seismic Instrumentation Technology Symposium*, 2009.

[26] T. B. Gabrielson, "Mechanical-Thermal Noise in Micromachined Acoustic and Vibration Sensors," *IEEE Transactions on Electron Devices,* vol. 40, no. 5, pp. 903-909, 1993.

[27] D. W. Carrb, P. J. Clewsa, M. S. Bakera, G. R. Bogart, R. H. lsson, U. Krishnamoorthya and T. P. Swilera, "In-Plane MEMS-Based Nano-g Accelerometer with Sub-Wavelength Optical Resonant Sensor," *Sensors and Actuators A: Physical,* pp. 283-290, 2008.

[28] B. Avenson, C. T. Garcia, N. A. Hall, G. Onaran and B. A. Yocom, "Micro-Seismometers Via Advanced Meso-Scale Fabrication," *Monitoring Research Review: Ground-Based Nuclear Explosion Monitoring technologies,* pp. 280-288, 2010.

[29] L. F. Degerteken, N. A. Hall, W. Lee and Z. Zhiping, "Fabrication and Characterization of a Micromachined Acoustic Sensor With Integrated Optical Readout," *IEEE Journal of Selected Topics in Quantum Electronics,* vol. 10, no. 3, pp. 643-651, 2004.

[30] R. Paschotta, "RP Photonics Encylopedia," RP Photonics, 26 06 2013. [Online]. Available: http://www.rp-photonics.com/phase_noise.html. [Accessed 13 08 2013].

[31] D. W. Carr and Symphony Acoustics, "Accelerometer Comprising an Optically Resonant Cavity". United States of America Patent 7,583,390 B2, 1 September 2009.

[32] E. S. Hor, "Knowledge and Entertainment," 16 January 2012. [Online]. Available: seanghor.files.wordpress.com/2012/01/expt04fabryperot.pdf. [Accessed 04 08 2013].

[33] M. Horbatsch, "Marko Horbatsch: webpage," 01 December 2005. [Online]. Available: http://www.yorku.ca/marko/PHYS2212/lab7.pdf. [Accessed 14 08 2013].

[34] G. Hernandez, Fabry-Perot Inferometers, Cambridge: Press Syndicate of the University of Cambridge, 1986.

[35] Physikinstrumente, "PI," Physikinstrumente, 1996. [Online]. Available: http://www.physikinstrumente.com/piezo-actuator/PL022,%20PL033,%20PL055-piezo-actuator.html. [Accessed 10 03 2014].

[36] Seismic Equipment Solutions, "Seismic Equipment Solutions," 2003. [Online]. Available: http://www.globalses.com/oem_brochures/GS-32CT%20Geophone.pdf. [Accessed 10 02 2014].

[37] Alberta Energy Regulator, "Report 2013 B: Pipeline Performance in Alberta, 1990 - 2012," Alberta Energy Regulator, Calgary, 2013.

[38] University of Cincinnati, "University of Cincinnati Structural Dynamics Research Lab," 2008. [Online]. Available: http://www.sdrl.uc.edu/academic-course-info/docs/ucme662/v2_2.pdf. [Accessed 15 January 2014].

[39] Massachusetts Institute of Technology Department of Mechanical Engineering, "Understanding Poles and Zeros," 21 October 2013. [Online]. Available: http://web.mit.edu/2.14/www/Handouts/PoleZero.pdf. [Accessed 21 October 2013].

[40] Unknown, "Wikipedia," Wikipedia Foundation, 22 07 2013. [Online]. Available: http://en.wikipedia.org/wiki/Seismic_waves. [Accessed 03 December 2012].

Appendix A: Process Flowchart for Experimental Leak Detection

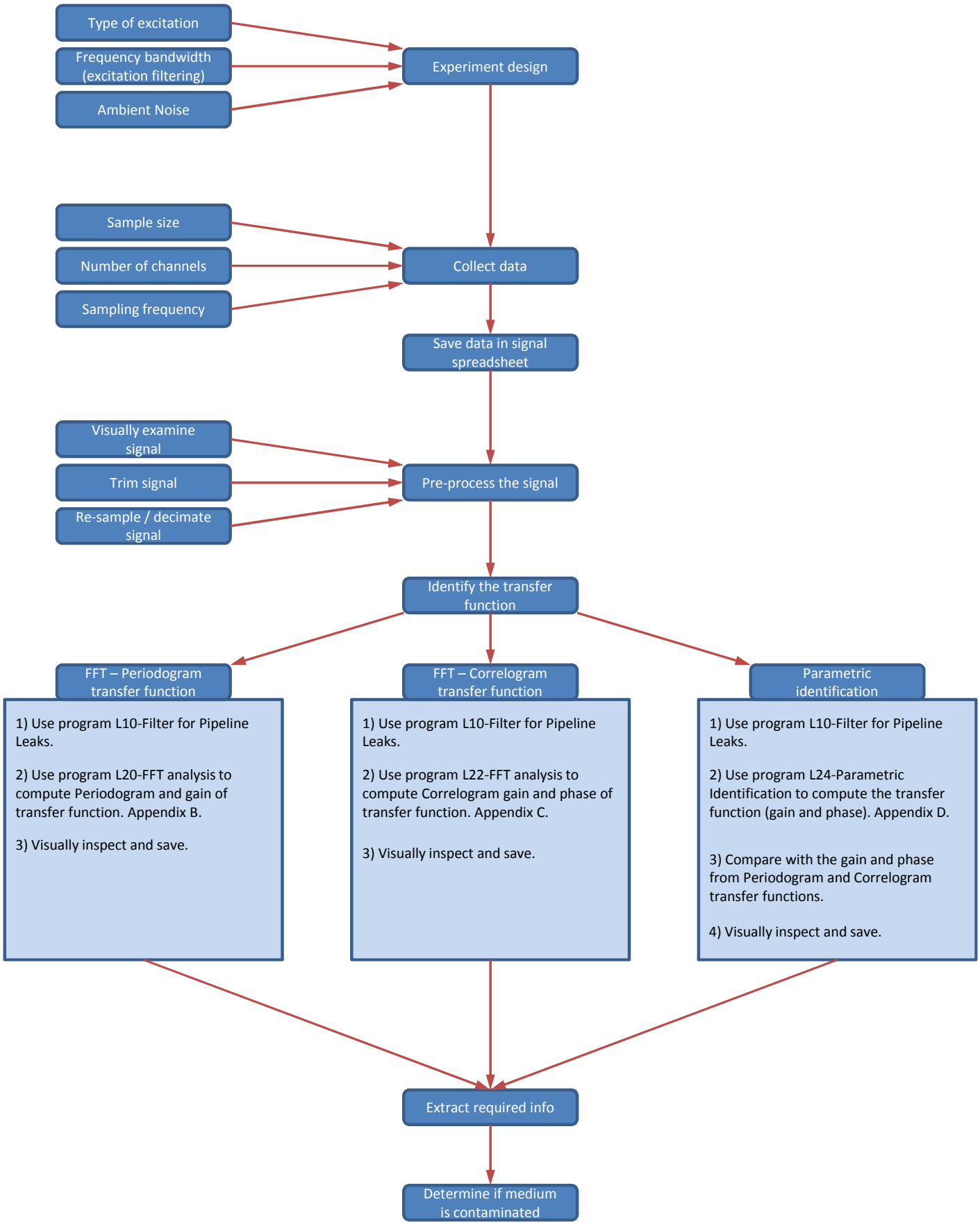

Appendix B: Process Flowchart for Periodogram Method of PSD Estimation

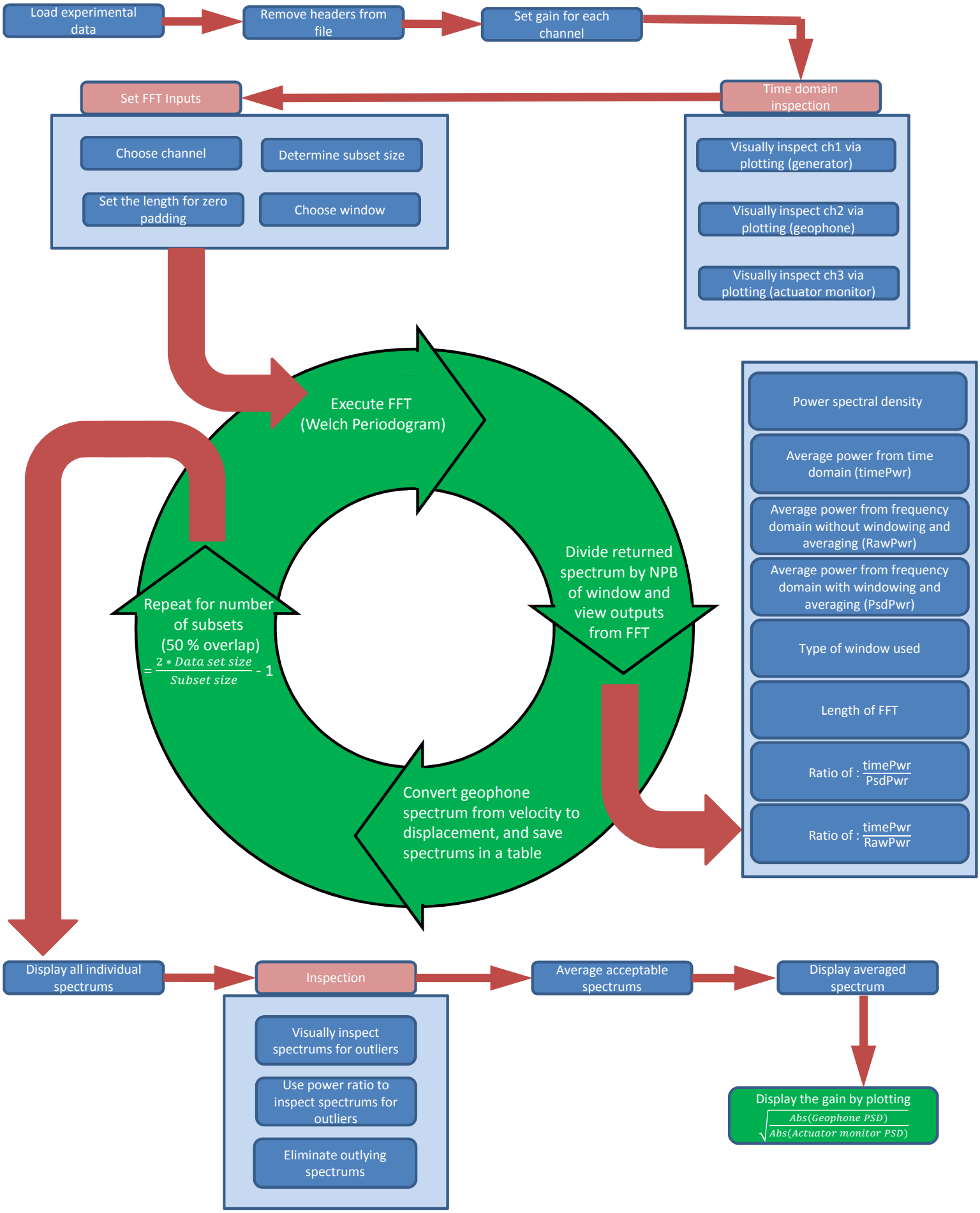

Appendix C: Process Flowchart for Correlogram Method of PSD Estimation

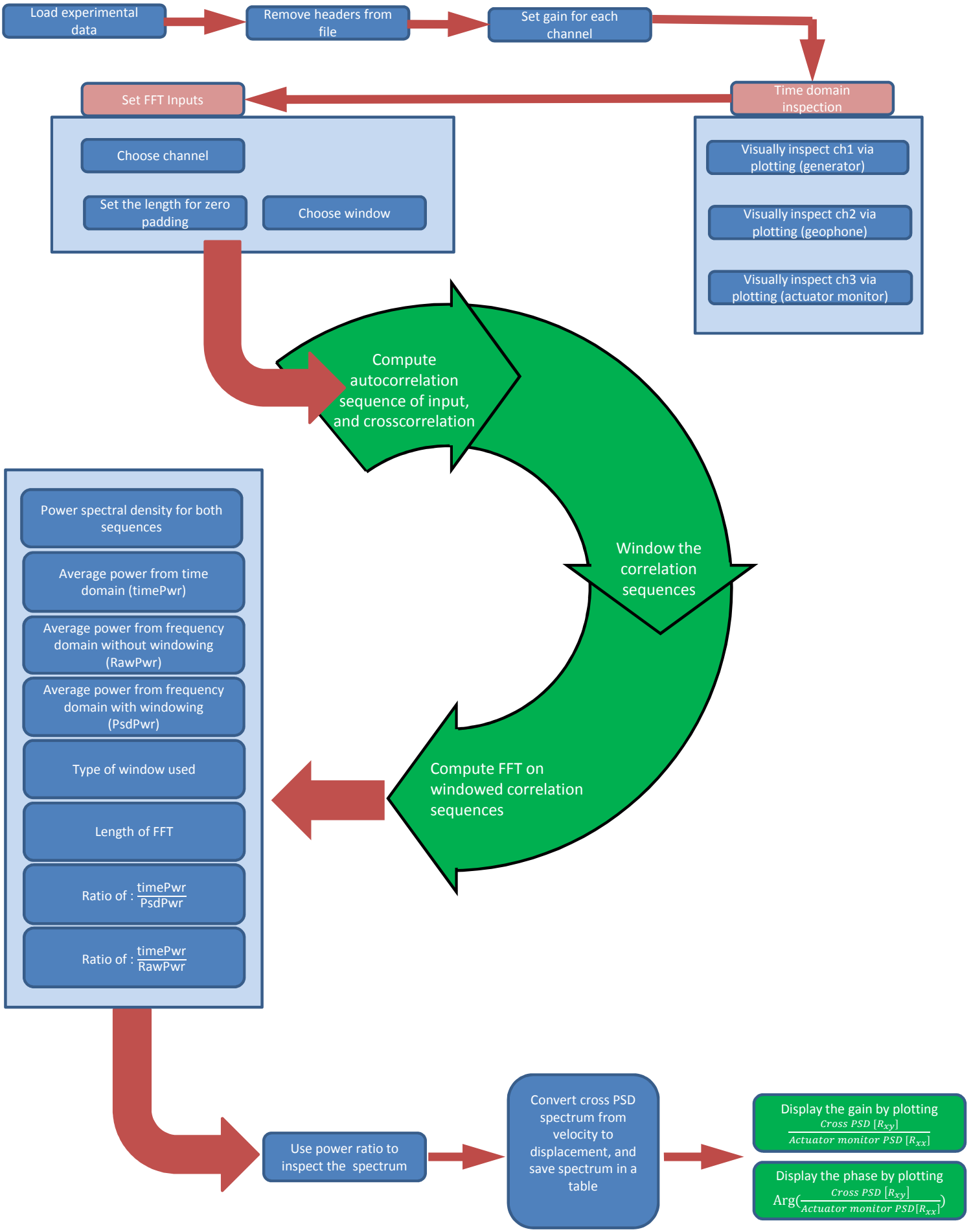

Appendix D: Process Flowchart for the Parametric Estimate of the Transfer Function